Proton Coupled Electron Transfer Reactions at the Surface of Metal Oxide Nanomaterials

Miles N. Braten

A dissertation

submitted in partial fulfillment of the

requirements for the degree of

Doctor of Philosophy

University of Washington

2015

Reading Committee:

James M. Mayer, Chair

Daniel R. Gamelin

Robert E. Synovec

Program Authorized to Offer Degree:
Department of Chemistry

University of Washington

Abstract

Redox Reactions at the Surface of Metal Oxide Nanomaterials: Proton Coupled Electron Transfer Dynamics of Reduced Zinc Oxide Nanocrystals and Screening Metal Oxides for an Alkane Oxidation Catalyst

Miles N. Braten

Chair of the Supervisory Committee:
Professor James M. Mayer

Nanostructured metal oxide materials are found in many products and processes in our society today, but they play a particularly important role in the conversion and storage of energy. The materials are used as catalysts and redox active supports in devices such as dye sensitized solar cells, solid oxide fuel cells, and flow batteries, where they transfer and store electrons and charge balancing cations. Oftentimes electron transfer is modulated by the cations and when the cation is a proton, these redox reactions are known as proton coupled electron transfer (PCET) reactions. The work described in this dissertation focuses on understanding the PCET reactivity of nanocrystalline metal oxide materials. Chapter 1 introduces the concept of PCET and provides background information on the zinc oxide (ZnO) nanocrystals (NCs) which the majority of the research is focused on. Chapter 2 examines the chemistry that occurs during the photoreduction of ZnO NCs. Chapter 3 describes experiments probing how ZnO NC capping ligand concentration and NC size modulate PCET reaction rates. Chapter 4 describes experiments that compare the PCET reactivity of ZnO NCs with different numbers of electrons and protons stored

on them. Chapter 5 describes attempts to observe the electrochemical reduction of ZnO NCs attached to gold electrodes. Finally, Chapter 6 contains attempts to identify a nanostructured metal oxide alkane oxidation catalyst for use in fuel cell.

TABLE OF CONTENTS

LIST OF FIGURES

LIST OF TABLES

ACKNOWLEDGEMENTS

When I asked my undergraduate inorganic chemistry teacher who would be a good graduate school advisor if I wanted to study electron transfer he wrote me a list. At the top of the list was, "Jim Mayer UW". He circled the top line, set down his pen, pointed to Jim's name and said "Jim Mayer, excellent scientist and a good human being." Those words could not be truer. In the five years that I have worked in Jim's lab he has pushed me to become a better scientist and a stronger person. He demonstrated patience and flexibility, especially over the past year allowing me to work remotely after the lab moved to Yale. Jim kept me motivated throughout my career as a graduate student, known when to play "disappointed dad" when I was slacking and when to be a "cheerleader" when research was making me want to pull my hair out. He helped guide my research in a direction in line with my career plans and sent me to San Francisco, Kelowna B.C., and Sweden to discuss my research with an international audience of chemists.

During graduate school your labmates become an extended family. Carolyn Valdez, my lab sister, is one of the smartest, hardest working, and enthusiastic people I have ever come across. I feel very lucky to have entered the lab at the same time as her and work on very similar projects. She was always there when I had a chemistry question or needed to vent about some aspect of graduate school, science, or lab drama. Rebecca Hayoun got Carolyn and I started on research in the Mayer lab and as a big sister, provided us with sage advice before she graduated. Tristian Tronic was a patient older brother, with acute sense of safe laboratory practice. He could point out my mistakes with making me feel stupid and had the respect of everyone in the lab. David Lao was a cool older brother. He taught me how to keep the GC instrument that was older than me running and was always there to provide moral support as I prepared for exams and presentations. His love of 1980s metal was a surprise to me but it was great to have a lab brother who enjoyed cranking up Iron Maiden and Black Sabbath. Shoshanna Barnett was the lab sister with warm motherly wisdom. She got me hooked on electrochemistry and Igor.

Some of the younger siblings I got to know a little better. Jessica Wittman was my lab sister with closest sense of humor. She could sense when I needed to talk about graduate school stress and was always there to answer questions about PCET. Her chemistry skills in the kitchen led to many dinner parties shared with other lab members and she was always down to attend whatever metal concert I might be heading to on a Friday night. Tom Porter was the class clown of our lab. He always had something to joke about and loved playing music in the lab that got underneath everyone's skin. Tom often tested my patience; especially when he would sneak tickle me while I was working in the glovebox. Tom loved drinking and dive bars and introduced the whole department (including some visiting professors from China) to the Moon Temple, RIP. Jennifer Peper was a great little sister to have in the lab. Her attention to detail makes her an awesome scientist. I enjoyed getting to be her housemate for my last stint in New Haven and always found out discussions about feminism a refreshing break from nanoparticles and redox reactions. And last but not least is Mike Pegis. For a little brother, at this point his knowledge of electrochemistry exceeds mine. His propensity to loose government identification has provided

the lab with many fun stories. My interaction with the new Yale students was brief, but I definitely connected with Scott Kolmar over sludge metal and chopped and screwed rap. Janelle, Julia and Gannon all seem like great additions to the lab and I wish them the best of luck.

Post docs must be uncles and aunts. Joel Schrauben was the coolest uncle. He led the effort in distilling the labs research on nanoparticles into a Science paper. Joel encouraged me to stay in grad school when I was having doubts about it during my second year. He also introduced me to "noise" music and some new friends in Seattle with whom we "played" noise. Alex Fox would be the weird lab uncle. His sense of humor was dark and he could slow down any paper meeting with discussion about punctuation and word choice. Colin Carver drank more coffee than any human being I have ever met. He was also great with mechanical thing and taught how to fix leaky Schlenk lines when mine would not hold vacuum. Johanna Blacquiere was my first Canadian relative and introduced the lab to garlic fingers and donair. She had a keen sense of how to make measurements and helped me develop experimental methods. Nothing can stop Caroline Saouma. She was an intensely dedicated chemist with good hands and a sharp mind. She was an aunt who could help you with anything, but who would also scare the hell out of you when experiments were not going her way. While she could be volatile, we all appreciated the order she brought to the lab, constantly fighting entropy. My Canadian uncle, Derek Wasylenko brought the Mayer groups electrochemistry game to another level. It was fun to show him around San Francisco and the whole lab enjoyed it when he and my Spanish uncle Carlos Rodriguez del Rio made fun of each other's linguistic quirks. Carlos helped the whole lab learn the tricks of stopped-flow kinetics and introduced the brave lab members to Kalimoxto. Although he was quiet upon arrival, he constantly had the whole lab laughing especially with the research papers he would show us over coffee. Bradley McKeown was the uncle who taught me what southern hospitality truly means. I will always remember his keen eye and thoughtful comments during paper editing. Miriam Bowring was the aunt who both inspired and encouraged me. She could tackle any problem her project through at her and always provided a sounding board for research ideas and frustrations with grad school and life. My interaction with Delina Damatov was far too brief, but I enjoyed talking about chemistry with her and learning about Israeli culture. Ryoji Mitsuhashi was an absolute blast in and outside the lab. Of the four Japanese visitors we had over my time in the lab he was the most memorable.

Members from the groups past resurfaced during my time in the group. Elizabeth definitely felt like a lab mother and was instrumental in organizing for the lab move to Yale. She was also helpful when it came to thinking about experimental design. There is far too much I have in common with Todd Markle. From attending the University of San Francisco and performing undergraduate research with William Karney and Claire Castro to loving the music of the Bay Area and Seattle, there were countless conversation topics that kept us up late on several occasions. He also helped me deepen my understanding of PCET and Marcus theory. I was also lucky enough to have Ian Rhile spend a summer sabbatical in our lab. He is an amazing chemist and warm, understanding person.

There are many outside the Mayer group who helped me on my way through graduate school. Professor Gamelin was a great collaborator providing insight that always strengthened our research and publications. He also invited me to his group meetings and into his lab to work after the rest of the Mayer group moved to Yale. Professor Synovec provided guidance for me on a few occasions when I was unsure if continuing in graduate school was the right thing for me. Thanks for finding the words to help me stick it out. I cannot forget to mention Paul Miller and

Adrienne Roehrich who kept the NMRs and ICP up and running for us. Martin Sadilek and Loren Kruse were always helpful when I was working in the mass spec lab.

Off of campus having a great network of friends and an awesome partner kept me sane and helped me enjoy my grad school experience to the fullest. I could not have done this without Chelsea Dalton and her constant support and love. My first housemates and friends in Seattle, at Beast Lake, kept me sane and introduced me to the local music scene and venues. Numerous nights spent at the Black Lodge or Highline having my eardrums pummeled in the company of friends kept me from losing my grip on reality.

DEDICATION

To the teachers inspired me to pursue a path in science.

to my mother and father encouraging me to understand what they did not,

to Ms. Swift for opening my eyes to how chemistry runs through everything

to Mr. Sours for showing me that math can be fun

to Mrs. Ball for showing me that "Chem is Cool"

to Warren Haskell for inspiring to work at something to better the world

to Dr. Toia for introducing me to scientific research

to Dr. Spector for keeping an eye out for during my undergraduate years

to Dr. Castro and Dr. Karney for getting me hooked on research

to Dr. Melaugh for expanding my view of chemistry and scientist

to Dr. Curtis for introducing me to inorganic chemistry and recommending an advisor

Chapter 1. INTRODUCTION

1.1 METAL OXIDES

Metal Oxides (MO_x) are a large family of materials composed of metal cations and oxygen anions. They range in lattice structure, color, reactivity, conductivity, and, usefulness to society. For example, iron oxide is red material commonly known as rust, which forms when iron reacts with water or O_2 from the atmosphere and there are whole fields of research devoted to slowing the formation of this oxide. On the other hand, alpha phase Fe_2O_3 and specially prepared amorphous iron oxide are water oxidation catalysts currently being studied for solar fuel production.[1,2] At high temperatures (~800 °C) cerium oxide is used as the anode in methane consuming solid oxide fuel cells due to its high electrical conductivity and propensity for oxygen diffusion.[3] Zinc oxide (ZnO), a white colored, wide bandgap semiconductor is used in ubiquitous consumer items such as pigment in paints and as a UV absorber in sunscreen. As an n-type semiconductor (having excess electrons) it has been used in transparent electrodes for dye-sensitized solar cells[4] and is currently being studied for use in UV light emitting diodes[5].

This dissertation is a collection of studies on the reactivity of nano-scaled metal oxides, with colloidal ZnO nanocrystals (NCs) being the main MO_x of interest. More specifically, the studies are focused on the use of these materials as reducing agents that also can deliver protons, as well as the oxidation of organic substrates at the surface of metal oxides. There is much interest in using nanoscale metal-oxides as catalysts for the oxidation and reduction of small molecules such as water or carbon dioxide (CO_2) because these MO_x nanomaterials can accept or donate multiple electrons and protons. The ability to store and transfer multiple reducing equivalents and charge balancing protons could help catalyze energy intensive reactions. For example in neutral water (pH = 7, 1 atmosphere pressure), the single electron reduction of CO_2 requires a potential of -1.90 V vs NHE, but the 2 electron and 2 proton reduction to formic acid (HCO_2H) requires a potential of only -0.61 V vs NHE.[6]

While few examples of catalysis are presented within this dissertation, it does contain experiments that identify important factors that affect the rate of these reactions and probe how these processes occur. The second chapter elucidates what is oxidized during the photoreduction of ZnO NCs. Chapter three describes experiments in which reduced ZnO NCs transfer electrons

and protons to organic substrates in the limit of less than one electron per NC. The fourth chapter examines similar reactivity but with ZnO NCs containing more than one electron. Chapter five, the final chapter containing experiments with ZnO, describes attempts to observe reductions of ZnO NCs anchored to electrodes. The last chapter in this dissertation contains attempts to identify a nanostructured metal-oxide alkane oxidation catalyst.

1.2 Proton Coupled Electron Transfer

When protons modulate the reduction and oxidation potentials of a molecule or material, the redox reactions are referred to as proton coupled electron transfer (PCET) reactions.[7] This thermodynamic coupling of protons and electrons is often summarized in what has become known as a Square Scheme, Figure 1.1. In the top left corner of the scheme, reactants X-H and Y can be observed. In this reaction a proton and an electron from X will be transferred to Y. Proton transfer (PT) and electron transfer (ET) are both elementary steps of this reaction, so if the reaction starts with a proton transfer, moving to the right across the top, the charged intermediates X^- and $H\text{-}Y^+$ are obtained. The negatively charged intermediate X^- may then transfer an electron to the positively charged intermediate $H\text{-}Y^+$, following the downward pointing arrow on the right, yielding the neutral products X and H-Y. This way of moving from reactants to products, with initial proton transfer, is referred to as the stepwise PT-ET mechanism. It is also possible for X-H to transfer an electron to Y initially and go through a stepwise ET-PT pathway. Alternatively, the proton and electron can be transferred from X-H to Y in one kinetic step, a net hydrogen atom transfer (HAT),[8] which avoids the often high energy charged intermediates. This pathway has been defined as concerted proton electron transfer (CPET).[9]

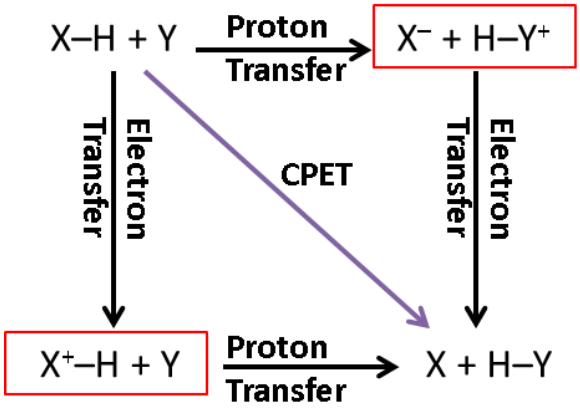

Figure 1.1. A square scheme demonstrating stepwise, PT-ET and ET-PT, as well as the concerted proton electron transfer (CPET) pathway for a proton coupled electron transfer reaction.

When a molecule or material participates in PCET reactions, the reduction potentials of the unprotonated and protonated species and pK_a values of the reduced and oxidized species are measured to determine the thermodynamic coupling of the protons and electrons. For many metal-oxides under aqueous conditions this coupling is about 59 mV per pH unit, a Nernstian relationship. Attempts to determine this coupling for ZnO NCs in aprotic, organic solvents are described in chapter five.

1.3 Chemistry at the Nanoscale

The field of nanoscience focuses on the synthesis, characterization, physical properties, and reactivity of particles or materials comprised of particles with dimensions from one to hundreds of nanometers (nm). While nanoparticles of many shapes and sizes can be synthesized; spheres, rods, cubes, plates, *etc.*, the ZnO NCs described in this thesis are roughly spherical[10] and range in size from about 3 to 6 nm in diameter. One interesting aspect of nano-sized materials is that the surface area to volume ratio of the nanoparticles is much greater than those of their bulk counterparts. For example a ZnO NC with a 4.0 nm diameter would have a volume of 33 nm^3 and a surface area of 50 nm^2. An NC of this size would contain about 1400 Zn ions and about 400 of these ions, or about 30 percent, would be located at the surface.[11] This is one of the major differences between nano and bulk materials where surface ions would be a very small fraction

of the total. When considering reactions that are catalyzed at surfaces, nanomaterials have the advantage of this high surface to volume ratio but our understanding of how particular reactions occur is still nascent.

Quantum confinement is an important phenomena encountered in nano-sized semiconductor materials, which effects the bandgap energy and therefore the optical and electronic properties of a given material. A simple way to explain the effect is that it is observed when a nanoparticle has a smaller radius than the Bohr radius of a conduction band electron in a specific material. For spherical nanocrystal the deviation in bandgap energy from that of the bulk is described by the Brus Equation, Equation 1.1.[12,13] In this equation E^* is the energy of the band gap of a given size nanocrystal; E_g is the energy of the bandgap in the bulk, ħ is Plank's constant divided by 2π, R is the radius of the NC, m_e and m_h are the effective masses of the electron and the hole, e is the electron charge, and ε is dielectric constant for the bulk material. From the Brus equation it is evident that E^* roughly increases with the inverse square of the NC radius until the radius reaches the Bohr radius of an electron in a given material and the bandgap of the NC is equal to that of the bulk.

$$E^* \cong E_g + \frac{\hbar^2\pi^2}{2R^2}\left[\frac{1}{m_e}+\frac{1}{m_h}\right] - \frac{1.8e^2}{\varepsilon R} \quad (1.1)$$

The deviation in bulk bandgap energy is net positive and shifts both the conduction and valence bands, meaning that conduction band electrons are more reducing and valence band holes are more oxidizing than in the bulk. This increase also affects the optical bandgap of NCs within the regime of quantum confinement so the band-edge absorption onset is blue-shifted compared to that of the bulk materials. For semiconductors such as CdSe, with an optical bandgap in the visible range, the color of the absorption and emission can be tuned with NC size and is probably what led to such NCs being referred to as "quantum dots."

1.4 Background on Zinc Oxide Nanocrystals

ZnO nanocrystals have been studied since the early 1980s in a variety of contexts. Early theoretical work by Brus on the electronic properties of semiconductor "clusters" included calculations on ZnO due to its wide bandgap of about 3.4 eV.[14] As other researchers developed methods for synthesizing clusters of ZnO they began to study the photophysical properties of the

particles and provide experimental data to test the predictions of theory.[15,16] Experiments in the optical properties of ZnO nanocrystals eventually led to the realization that "extra" electrons could be stored in the particles upon exposure to photons with energy greater than the optical bandgap.[17] Using thin films of ZnO nanocrystals, investigators have probed the optical[18] and size dependent electrochemical properties of these materials.[19] In aqueous conditions, Lemon and Hupp found evidence of proton uptake during the electrochemical reduction of ZnO thin films.[20] As research on ZnO nanocrystals progressed, the use of aliphatic capping ligands such as dodecylamine and trioctylphosphine oxide (TOPO),[21] allowed for the suspension of the crystals in aprotic organic solvents. Under these conditions Shim and Guyot-Sionnest demonstrated nanocrystal reduction from both molecular redox reagents and photolysis.[22]

The majority of redox reactivity with ZnO in this dissertation comes revolves around photoreduction or uses nanocrystal that that were photoreduced, so a brief explanation of this process follows. The photoreduction of ZnO nanocrystals occurs after the absorption of a photon with energy greater than the optical bandgap creates an exciton. An exciton is the electron that has been excited to the conduction band of a crystal and the hole remaining the valence band that are coulombically bound. The hole in the exciton migrates to the surface of the particle where oxidizes some species (often referred to as a hole trap) and keeping the electron that was excited into the conduction band from relaxing back down, Figure 1.2 In the anaerobic conditions these conduction band electrons are stable for days.

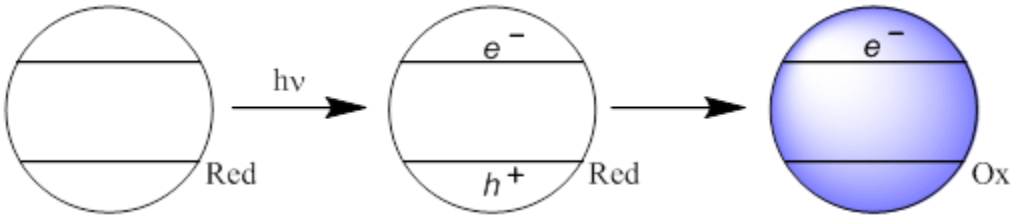

Figure 1.2. Photoreduction of a ZnO nanocrystal. From left to right: Unreduced nanocrystal with conduction and valence bands represented by horizontal lines, top and bottom, respectively and hole trap, "Red." Absorption of above bandgap radiation, hν, creates exciton, electron (e^-) in the conduction band and hole (h^+) in the valence band. Oxidation of hole trap leaves behind oxidized species, Ox, and leaves "extra" electron in nanocrystal conduction band.

Solutions of unreduced ZnO nanocrystals are colorless. Upon reduction, the solutions become light to dark blue depending on the electron concentration. The UV-visible spectra of

reduced ZnO NCs display a blue-shift of the band-edge absorption and a broad increase in the visible wavelengths that peaks in the IR, Figure 1.3. Titrations of the extra electrons in ZnO nanocrystals have shown the broad visible absorbance is linear with electron concentration.

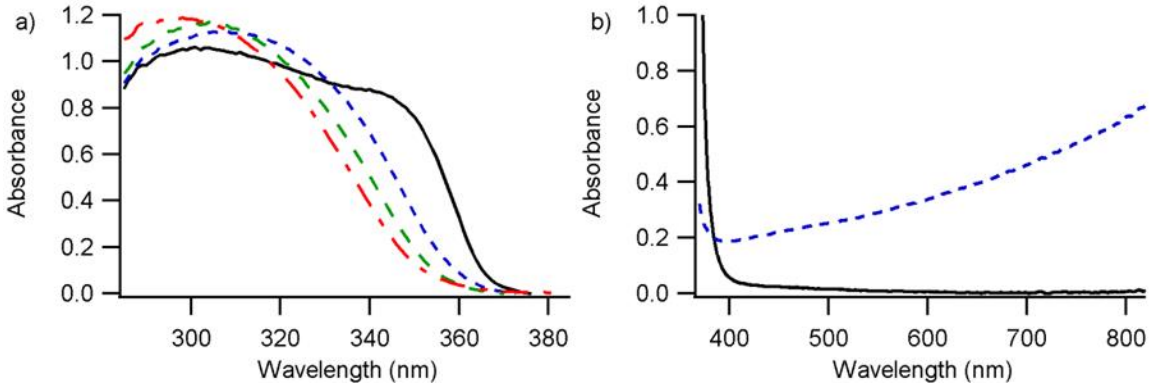

Figure 1.3. Spectral changes associated with photoreduction of ZnO NC solutions. a) Spectra of a dilute solution (~1 μM) of ZnO nanocrystals before photolysis (black, solid); after 30 seconds of photolysis (blue, dashed); after 60 seconds of photolysis (green, dashed) and after 120 seconds of photolysis (red, dot-dashed.) b) Spectra of a concentrated solution (~0.1 mM) of ZnO NCs before (black, solid) and after 45 minutes of photolysis (blue, dashed.

Research on the reactivity of ZnO nanocrystals in the Mayer lab began in a collaboration with the Gamelin lab which had developed syntheses of high quality nanocrystals[10] and an understanding of their chemistry. Much of this early research was performed by Liu, who was the first to demonstrate that the conduction band electrons were stable for days and could be titrated. This led to the observation that multiple electrons could occupy the conduction band of ZnO NCs.[23,24] Following up the work of Liu, Whitaker established that the electron paramagnetic resonance signals of CB electrons in ZnO NCs was size dependent.[25] This allowed for the demonstration of electron transfer from small photoreduced nanocrystals to large unreduced nanocrystals with the driving force being provided the difference of conduction band energy due to quantum confinement.[26] Stoichiometric reactions between photoreduced ZnO nanocrystals and organic hydrogen atom acceptors in aprotic organic demonstrated that these nanomaterials were PCET reagents. This reactivity was also recognized with TiO_2 nanoparticles and initial kinetic studies pointed to a CPET process.[27] Studies with of the ZnO NCs with chemical reductants, oxidants, acids and bases revealed that the presence of protons greatly affected the reduction potential of the ZnO NCs.[28]

As four of the chapters in this dissertation focus on reactions of colloidal ZnO NCs, it is important to document the NC synthesis and characterization procedures. The following section contains the pertinent details of the preparation and characterization of all the ZnO NC batches used in the experiments described in this dissertation.

1.5 Synthesis and Characterization

1.5.1 *General Considerations*

Zinc acetate dihydrate ($Zn(OAc)_2 \cdot 2H_2O$), tetramethylammonium hydroxide pentahydrate ($Me_4NOH \cdot 5H_2O$) and dodecylamine were purchased from Sigma Aldrich. Unless noted, solvents were purchased from Fisher. Ethanol was obtained from Decon and hydrochloric acid was purchased from Macron. The zinc standard solutions (1000 µg/mL) for were purchased from High-Purity Standards. Toluene was dried using a Seca Solvent System installed by Glass Contour.

Centrifugation was performed with a Hamilton Bell Vanguard 6500 centrifuge. Absorption spectra were collected with a Hewlett-Packard 8453 diode-array UV-visible spectrophotometer. Inductively Coupled Plasma, Atomic Emission Spectroscopy (ICP-AES) was performed on either a Jarrell Ash 955 Atom Corp or a Perkin Elmer Optima 8300 ICP optical emission spectrophotometer.

1.5.2 *Zinc Oxide Nanocrystal Synthesis*

Batches of nanocrystals were prepared in different quantities based on methods developed Schwartz[29] and modified by Norberg.[10] For a medium sized batch (other batch conditions listed in Table 1.1), $Zn(OAc)_2 \cdot 2H_2O$ (3g, 13.7 mmol) was dissolved in 100 mL of dimethyl sulfoxide and 40 mL of ethanol in a 500 mL Erlenmeyer flask and placed in an ice bath with stirring. A solution of $Me_4NOH \cdot 5H_2O$ (4 g, 23.1 mmol) was prepared with 40 mL of ethanol and transferred to a separatory funnel and dripped into the cold zinc acetate solution over the period of about 12 minutes. After addition of the base solution was complete, nanocrystal growth was arrested by precipitation with about 300 mL of ethyl acetate. The nanocrystals were collected by repetitive centrifugation at 3400 rpm. Once the nanocrystals had been separated from the reaction solution, they were dissolved in about 2 mL of ethanol, precipitated with about 10 mL of

n-heptane and pelleted by centrifugation. The dissolution, precipitation step was repeated in order to remove excess zinc and other starting materials. The nanocrystals were then capped by dissolving the pellet with 2 mL of dodecylamine heated to 160 °C. For smaller crystals, around 3.4 nm in diameter, about 10 mL of ethanol was added to precipitate the NCs. Larger NCs, 5 to 6 nm in diameter, were obtained by continued heating for 10 to 15 minutes with the size being monitored by optical absorption spectroscopy. The capped, precipitated ZnO nanocrystals were suspended in toluene, bubble degassed under reduced pressure three times, transferred to an N_2 filled glovebox and stored at -35 °C until use.

Table 1.1. ZnO NC Batch Sizes

Size	$Zn(OAc)_2 \cdot 2H_2O$ (g, mmol)	DMSO/EtOH (mL)	$Me4OH \cdot 5H_2O$ (g, mmol)	EtOH (mL)
Small	1.0, 4.56	35/15	1.35, 7.45	12
Medium	3.0, 13.7	100/40	4.0, 22.1	40
Large	10.0, 45.6	330/135	13.4, 73.9	135

1.5.3 *Zinc Oxide Nanocrystal Characterization and Measurement of Concentration*

The average nanocrystal diameter was determined with the method developed by Meulenkamp using the minima of the derivative of the band edge absorption from a UV-visible absorption spectrum of a dilute solution of ZnO NCs.[30] This in turn was used to calculate the nanocrystal concentration after the Zn^{2+} concentration was measured by ICP-AES as is described below. A 400 µL aliquot of a ZnO solution was removed from the glovebox in a 1 dram vial and the solvent was removed under reduced pressure. The remaining dodecylamine-capped ZnO was then calcined in a tube furnace at 500 °C for at least 2 hours. The sample was then digested in ultrapure concentrated hydrochloric acid and diluted to 5 mL in a volumetric flask with deionized water. Five samples were prepared for ICP-AES analysis by the method of standard additions. A 100 µL aliquot of the digested ZnO NC stock was added to 10 mL volumetric flasks that were spiked with 0, 50, 150, 300 and 500 µL of a 1000 µg/mL Zn standard solution in 2% HCl. The flasks were filled to volume with deionized water. The intensity of the atomic emission for Zn was plotted against the added concentration of Zn ion and the x intercept of this line was

used as the [Zn] concentration. The average volume of a ZnO nanocrystal was calculated for a sphere with the diameter obtained from the absorption spectra. The wurzite ZnO unit cell has a volume of 47.66 $Å^3$ and contains two formula units per cell so the number of Zn ions per nanocrystal. was calculated using Equation 1.2. The nanocrystal concentration is obtained by the total Zn concentration from ICP-AES divided by the number of Zn ions per nanocrystal.

$$2 \times {}^{4}/_{3}\ \pi r^3 \ \div 47.66\ Å^3 \qquad (1.2)$$

1.6 NOTES

(1) van de Krol, R.; Liang, Y.; Schoonman, J. *J. Mater. Chem.* **2008**, *18* (20), 2311.

(2) Smith, R. D. L.; Prévot, M. S.; Fagan, R. D.; Zhang, Z.; Sedach, P. A.; Siu, M. K. J.; Trudel, S.; Berlinguette, C. P. *Science* **2013**, *340* (6128), 60–63.

(3) Steele, B. C. H.; Middleton, P. H.; Rudkin, R. A. *Solid State Ion.* **1990**, *40–41, Part 1*, 388–393.

(4) Hagfeldt, A.; Boschloo, G.; Sun, L.; Kloo, L.; Pettersson, H. *Chem. Rev.* **2010**, *110* (11), 6595–6663.

(5) Hassan, J. J.; Mahdi, M. A.; Yusof, Y.; Abu-Hassan, H.; Hassan, Z.; Al-Attar, H. A.; Monkman, A. P. *Opt. Mater.* **2013**, *35* (5), 1035–1041.

(6) Kumar, B.; Llorente, M.; Froehlich, J.; Dang, T.; Sathrum, A.; Kubiak, C. P. *Annu. Rev. Phys. Chem.* **2012**, *63* (1), 541–569.

(7) Warren, J. J.; Tronic, T. A.; Mayer, J. M. *Chem. Rev.* **2010**, *110* (12), 6961–7001.

(8) Mayer, J. M. *Acc. Chem. Res.* **2011**, *44* (1), 36–46.

(9) Costentin, C.; Evans, D. H.; Robert, M.; Savéant, J.-M.; Singh, P. S. *J. Am. Chem. Soc.* **2005**, *127* (36), 12490–12491.

(10) Norberg, N. S.; Gamelin, D. R. *J. Phys. Chem. B* **2005**, *109* (44), 20810–20816.

(11) Valdez, C. N.; Schimpf, A. M.; Gamelin, D. R.; Mayer, J. M. *ACS Nano* **2014**, *8* (9), 9463–9470.

(12) Brus, L. E. *J. Chem. Phys.* **1984**, *80* (9), 4403–4409.

(13) Brus, L. *J. Phys. Chem.* **1986**, *90* (12), 2555–2560.

(14) Brus, L. E. *J. Chem. Phys.* **1983**, *79* (11), 5566–5571.

(15) Koch, U.; Fojtik, A.; Weller, H.; Henglein, A. *Chem. Phys. Lett.* **1985**, *122* (5), 507–510.

(16) Bahnemann, D. W.; Kormann, C.; Hoffmann, M. R. *J. Phys. Chem.* **1987**, *91* (14), 3789–3798.

(17) Haase, M.; Weller, H.; Henglein, A. *J. Phys. Chem.* **1988**, *92* (2), 482–487.

(18) Redmond, G.; O'Keeffe, A.; Burgess, C.; MacHale, C.; Fitzmaurice, D. *J. Phys. Chem.* **1993**, *97* (42), 11081–11086.

(19) Hoyer, P.; Weller, H. *Chem. Phys. Lett.* **1994**, *221* (5–6), 379–384.

(20) Lemon, B. I.; Hupp, J. T. *J. Phys. Chem. B* **1997**, *101* (14), 2426–2429.

(21) Other researchers have shown that TOPO does not actually act as a ligand, but impurities found within the technical grade are actually acting as capping ligands. These impurities tend to be negative charged "X-type" ligands such as di-n-octylphosphinic acid, *n*-octylphosphonate, and P′-P′-(di-*n*-octyl) pyrophosphonate (a)Wang, F.; Tang, R.; Kao, J. L.-F.; Dingman, S. D.; Buhro, W. E. *J. Am. Chem. Soc.* **2009**, *131* (13), 4983–4994. (b) Morris-Cohen, A. J.; Donakowski, M. D.; Knowles, K. E.; Weiss, E. A. *J. Phys. Chem. C* **2010**, *114* (2), 897–906.

(22) Shim, M.; Guyot-Sionnest, P. *J. Am. Chem. Soc.* **2001**, *123* (47), 11651–11654.

(23) Liu, W. K.; Whitaker, K. M.; Kittilstved, K. R.; Gamelin, D. R. *J. Am. Chem. Soc.* **2006**, *128* (12), 3910–3911.

(24) Liu, W. K.; Whitaker, K. M.; Smith, A. L.; Kittilstved, K. R.; Robinson, B. H.; Gamelin, D. R. *Phys. Rev. Lett.* **2007**, *98* (18).

(25) Whitaker, K. M.; Ochsenbein, S. T.; Polinger, V. Z.; Gamelin, D. R. *J. Phys. Chem. C* **2008**, *112* (37), 14331–14335.

(26) Hayoun, R.; Whitaker, K. M.; Gamelin, D. R.; Mayer, J. M. *J. Am. Chem. Soc.* **2011**, *133* (12), 4228–4231.

(27) Schrauben, J. N.; Hayoun, R.; Valdez, C. N.; Braten, M.; Fridley, L.; Mayer, J. M. *Science* **2012**, *336* (6086), 1298–1301.

(28) Valdez, C. N.; Braten, M.; Soria, A.; Gamelin, D. R.; Mayer, J. M. *J. Am. Chem. Soc.* **2013**, *135* (23), 8492–8495.

(29) Schwartz, D. A.; Norberg, N. S.; Nguyen, Q. P.; Parker, J. M.; Gamelin, D. R. *J. Am. Chem. Soc.* **2003**, *125* (43), 13205–13218.

(30) Meulenkamp, E. A. *J. Phys. Chem. B* **1998**, *102* (29), 5566–5572.

Chapter 2. IDENTIFICATION OF THE PHOTOLYSIS PRODUCT FROM THE PHOTOREDUCTION OF AMINE CAPPED ZINC OXIDE NANOCRYSTALS

2.1 INTRODUCTION

Many of the first reported studies on the photoreduction of ZnO NCs were performed on solutions of uncapped NCs suspended in alcohols, water, or a combination of the two.[1–3] In these studies the alcohols (methanol, ethanol, or 2-propanol) were the logical hole quencher that led to the storage of electrons in the NC conduction band. Haase *et. al.* noted that the band edge bleaching was greater in solutions that included alcohol than solutions made from only water.[2] As research on NCs and QDs progressed, new syntheses of ZnO NCs capped with organic ligands (amines, and trialkylphosphine oxides) were developed.[4–6] These new capping ligands allowed for the dissolution of the ZnO NCs into non-polar organic media.

Using amine and trioctylphosphine oxide (TOPO) capped ZnO NCs, *prepared in the absence of alcohols*, Shim and Guyot-Sionnest demonstrated the one electron photoreduction of the NCs upon exposure to above bandgap radiation.[4] In contrast, our collaborators in the Gamelin group often added ethanol (2% v/v) to samples of ZnO NCs for photoreduction studies and achieved multiple electrons per NC.[7] With no reported hole quencher in Shim and Guyot-Sionnest's photoreduction studies, coupled with in depth reports of impurities in the 90% technical grade TOPO,[8] we began to question ethanol was always oxidized during NC photoreduction.

From a thermodynamic perspective, one may expect that the exitonic holes would preferentially oxidize the amines. The bond disassociation energies (BDEs) for the α C–H bonds of ethanol and *n*-butylamine are 96±1 and 90±2 kcal/mol respectively.[9] Assuming that the dodecylamine capping ligands have a BDE equal to that of *n*-butylamine, there is at least a 3 kcal/mol difference in favor of oxidizing the amine. After the first C–H bond breaking event in dodecylamine, subsequent loss of three more electrons and protons would lead to dodecanenitrile (Equation 2.1). During initial studies on the PCET reactivity of photoreduced ZnO NCs, the

presence of the proposed dodecanenitrile photolysis product was observed in NMR and GC-MS experiments.[10] The following experiments describe the identification of the hole quencher from the photoreduction of dodecylamine capped ZnO NCs.

$$CH_3(CH_2)_{10}CH_2NH_2 - 4e^- - 4H^+ \rightarrow CH_3(CH_2)_{10}C{\equiv}N \quad (2.1)$$

2.2 RESULTS

2.2.1 *Screening of the Dodecylamine Capping Ligand Starting Material*

The dodecylamine starting material was tested for the presence of dodecanenitrile as received from the manufacturer and after heating to simulate the conditions during NC capping. Gas chromatography coupled with flame ionization detection (GC/FID) of the starting material gave a retention time of 5.11 minutes for the dodecylamine, Figure 2.1a. By spiking the starting material with an authentic sample of dodecanenitrile, and observing an increased intensity for a peak with the retention time of 5.46, it was confirmed that dodecanenitrile was present in the starting material. The concentration of dodecanenitrile, measured by the method of standard additions, was determined to be about 0.1% (mol/mol) in both the as-received and heated dodecylamine starting material.

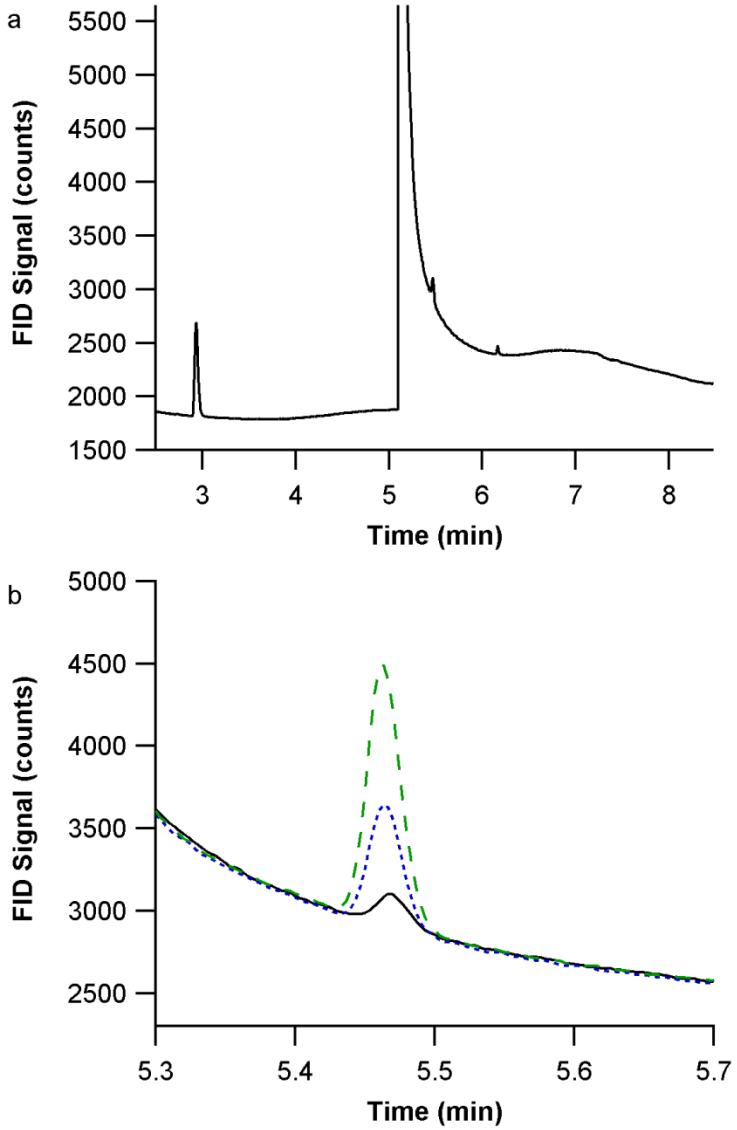

Figure 2.1. Chromatograms of dodecylamine starting material. (a) Chromatogram of 30 mM dodecylamine (5.11 min) and 0.3 mM naphthalene (2.93 min) internal standard. (b) Chromatograms of 30 mM dodecylamine with 0 (black, solid), 0.12 (blue, dotted) and 0.8 (green, dashed) mM spikes of dodecanenitrile (5.46 min).

2.2.2 *Analysis of Unphotolyzed and Photolyzed ZnO Solutions*

A solution of ZnO NCs was split in two. Half of the solution was photolyzed for thirty minutes turning deep blue and the other half was not photolyzed. The ZnO NCs (unphotolyzed and photolyzed) were precipitated with acetonitrile[11] and the supernatant was prepared for GC/FID

analysis with the intention of measuring an increase in dodecanenitrile concentration. The chromatogram of the supernatant from the unphotolyzed sample (Figure 2.2a, black, solid line) was similar to the dodecylamine starting material, with dodecanenitrile having a retention time of 5.46 minutes. The chromatogram of the supernatant of the photolyzed solution (Figure 2.2a, blue, dotted line) did not display an increase in the dodecanenitrile, but a new peak with a retention time of 5.90 minutes was observed.

Given the unexpected new peak, an experiment was undertaken in which a solution of ZnO NCs, from the same synthetic batch of the previous experiment, was split in two with one half of the solution being brought through five photolysis cycles and the other being left unphotolyzed. The chromatogram from the supernatant of the ZnO NC sample brought through five photolysis cycles displayed a dramatic increase in the new peak with a 5.90 minute retention time (Figure 2.2a, green, dashed line). Smaller peaks with retention time of 5.59 and 5.73 were also observed, suggesting that multiple products were made through the photoreduction and oxidation of the ZnO NCs.

To demonstrate that this product was not unique to this synthetic batch of NCs and to understand how the product increased with multiple photolysis cycles the following set of experiments were performed. A sample from a different synthetic batch of NCs was split into four portions, which were brought through zero, one, two and four photolysis cycles respectively. The chromatograms of the samples were similar to those from the previous synthetic batch displaying a peak with a retention time of 5.94 minutes that increased with photolysis cycle (Figure 2.2b). The product peak did not increase in whole number multiples (Figure 2.2b inset), which may be explained by the presence of other peaks and shoulders with retention times of 5.69, 5.85, and 6.0 minutes respectively.

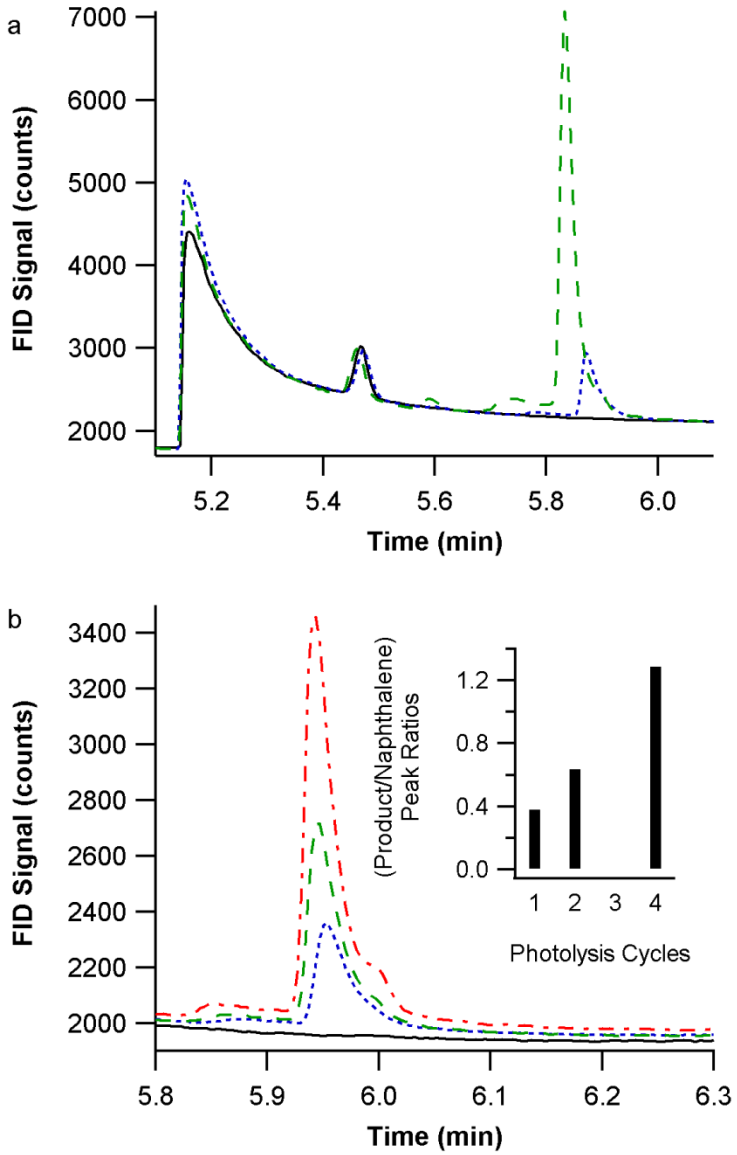

Figure 2.2. Chromatograms of capping ligand solutions separated from ZnO NCs. (a) Chromatograms from solutions of ZnO NCs that were photolyzed for 0 min (black, solid), singly photolyzed (blue, dotted), and 5X photolyzed (green, dashed). The peak with retention times of 5.46 and about 5.9 minutes correspond to dodecanenitrile the photolysis product respectively. (b) Chromatograms from solutions of ZnO NCs that were photolyzed for 0 min (black, solid), one 30 min cycle (blue, dotted), two 30 minute cycles (green, dashed), four 30 minute cycles (red, dot-dashed). Inset displays increase in intensity of the product peak with a retention time of 5.94 minutes (data were not obtained after three cycles).

2.2.3 *Identification of the Photolysis Product(s)*

In an attempt to identify the photolysis product with a retention time of 5.95 minutes in the GC/FID chromatograms, the samples prepared for GC/FID analysis were diluted appropriately for analysis on a GC/MS instrument (see section 2.5.5). Switching to a another instrument with a different column and parameters led to changes in retention times. The chromatograms of the samples photolyzed zero and one times had peaks with retention times of 6.0 and 7.8 minutes with mass spectra that matched naphthalene and dodecylamine respectively (not pictured). The chromatogram of the sample brought through four photolysis cycles had a new peak with a retention time of 8.4 minutes which should correspond to the peak at about 5.9 minutes in the GC/FID chromatograms based on its retention time being later than the DDA, (Figure 2.3). The product peak was most likely not observed in the sample brought through one photolysis cycle due to a lower concentration of the product.

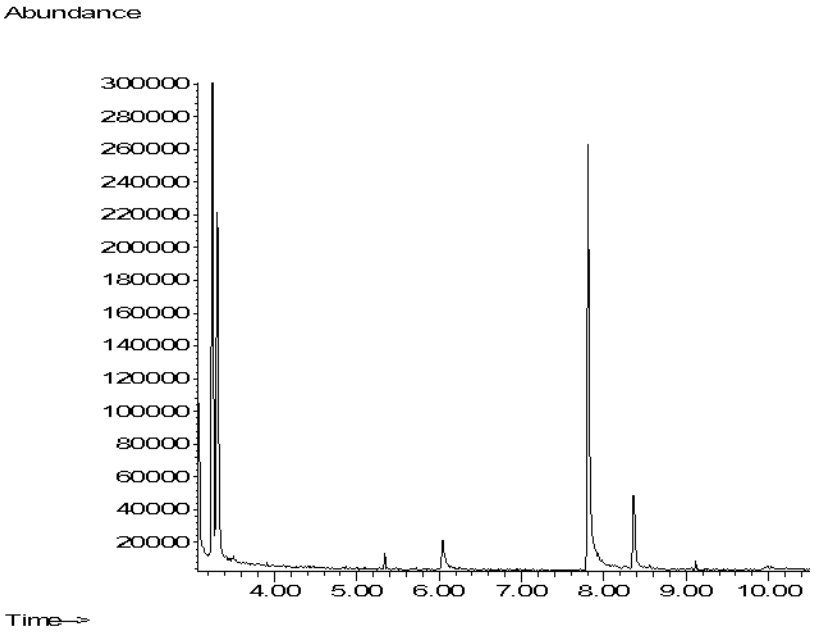

Figure 2.3. GC/MS Chromatogram of the supernatant from a solution of ZnO NCs photolyzed four times.The electron impact mass spectrum of the peak for dodecylamine, with a retention time of 7.8 minutes, displayed a weak signal for the parent ion at 185 m/z. Subsequent loss of 15 atomic mass units (amu) ($-CH_3$) yielded an ion at 170 m/z, followed by a fragmentation pattern showing 14 amu loss ($-CH_2$) down to 86 m/z (Fig 2.4a). This mass spectrum matched that of an authentic sample of DDA (not pictured). The mass spectrum of the

photolysis product peak, with a retention time of 8.4 minutes, displayed a strong signal at 196 amu, followed by a fragmentation pattern, showing a 14 amu loss down to 56 m/z (Fig 2.4b). The similar fragmentation to DDA suggests the new product is derived from the amine, but the signal at 196 m/z is likely a fragment of the parent species since it is only 11 amu heavier than DDA.

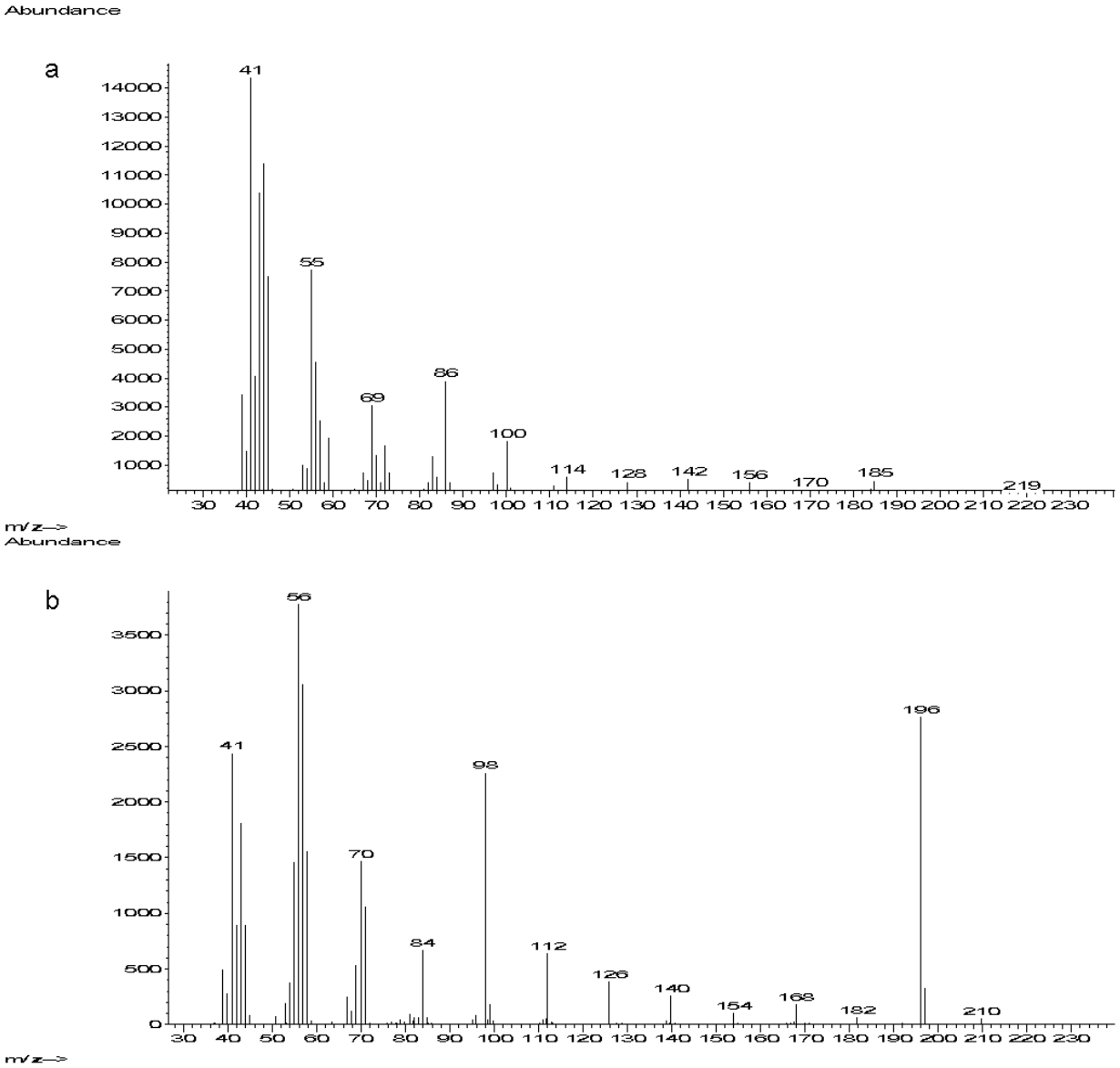

Figure 2.4. (a) Electron impact mass spectrum of dodecylamine, from the peak with a retention time of 7.8 minutes. (b) Mass spectrum of the photolysis product, from the peak with a retention time of 8.4 minutes.

Having been unable to identify the photolysis product with electron impact MS, a softer ionization method, electrospray ionization mass spectrometry (ESI/MS) was employed. The supernatant of a ZnO NC solution brought through 5 photolysis cycles was diluted in acidic acetonitrile and ESI/MS were obtained. The mass spectrum contained six signals, one at 186.2 m/z attributed to DDA plus a proton and five others at 212.2 m/z; 238.3 m/z; 274.4 m/z; 326.6 m/z; and 378.5 m/z which are the products formed during multiple photolysis cycles (Figure 2.5). These ions, with mass charge ratios greater than 186 m/z, were not observed in a control sample of DDA (not pictured).

The 26 amu difference between the dodecylammonium ion and first product ion, 212 m/z, could be accounted for by two carbon and two hydrogen atoms. A possible photolysis product with a molecular mass of 211 amu is 1-dodecanamine-*N*-ethylidene ($CH_3(CH_2)_{11}N{=}CHCH_3$ or DDI); which is the imine formed upon the condensation of acetaldehyde with dodecylamine. The acetaldehyde would be derived from the $2e^-/2H^+$ oxidation of ethanol at the surface of a photo-excited ZnO NP (Scheme 2.1 a, b). This photolysis product, with the signal of 212.2 m/z, is most likely the same product observed at 5.88 min by GC/FID and 8.4 min by GC/MS.

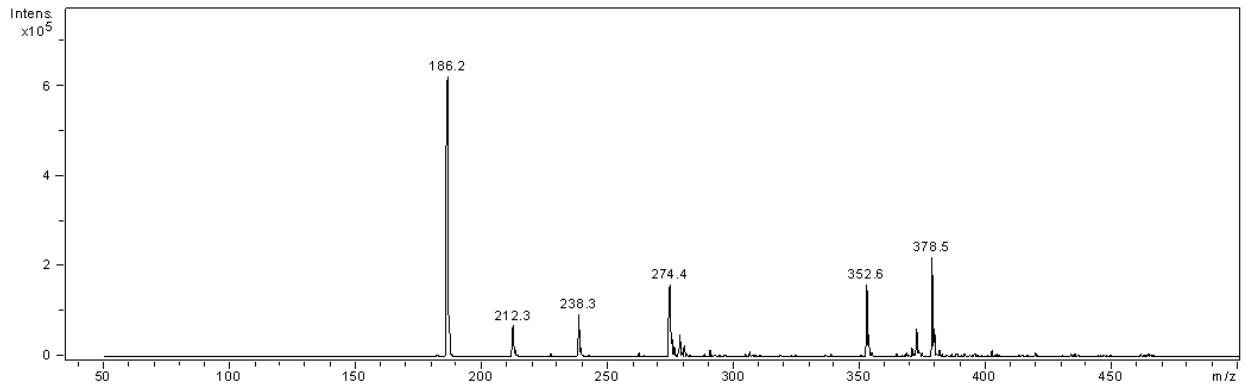

Figure 2.5. ESI/MS of the supernatant of a ZnO NC solution brought the five photolysis cycles displaying peaks for six different ions.

The ion with a mass to charge ratio of 238.3 amu is most likely the product from the condensation of two acetaldehyde molecules and a dodecylamine capping ligand. This could occur through the condensation of DDI with acetaldehyde (Scheme 2.1 C) Alternatively, acetaldehyde produced during photolysis could self-condense, yielding crotonaldehyde, which could then react with a DDA capping ligand (Scheme 2.1 d, e). The mass difference between the

274.4 and 238.3 ions is 36 amu, which can be accounted for by two oxygen and four hydrogen atoms. It is possible that the product from the condensation of crotonaldehyde and dodecylamine had both double bonds hydrated. The ions with mass charge ratios of 326.6 and 378.5 m/z could not be easily attributed to molecules known to be present in the photolyzed solutions and may be artifacts from the oxidation of photoreduced ZnO NCs or the ionization process.

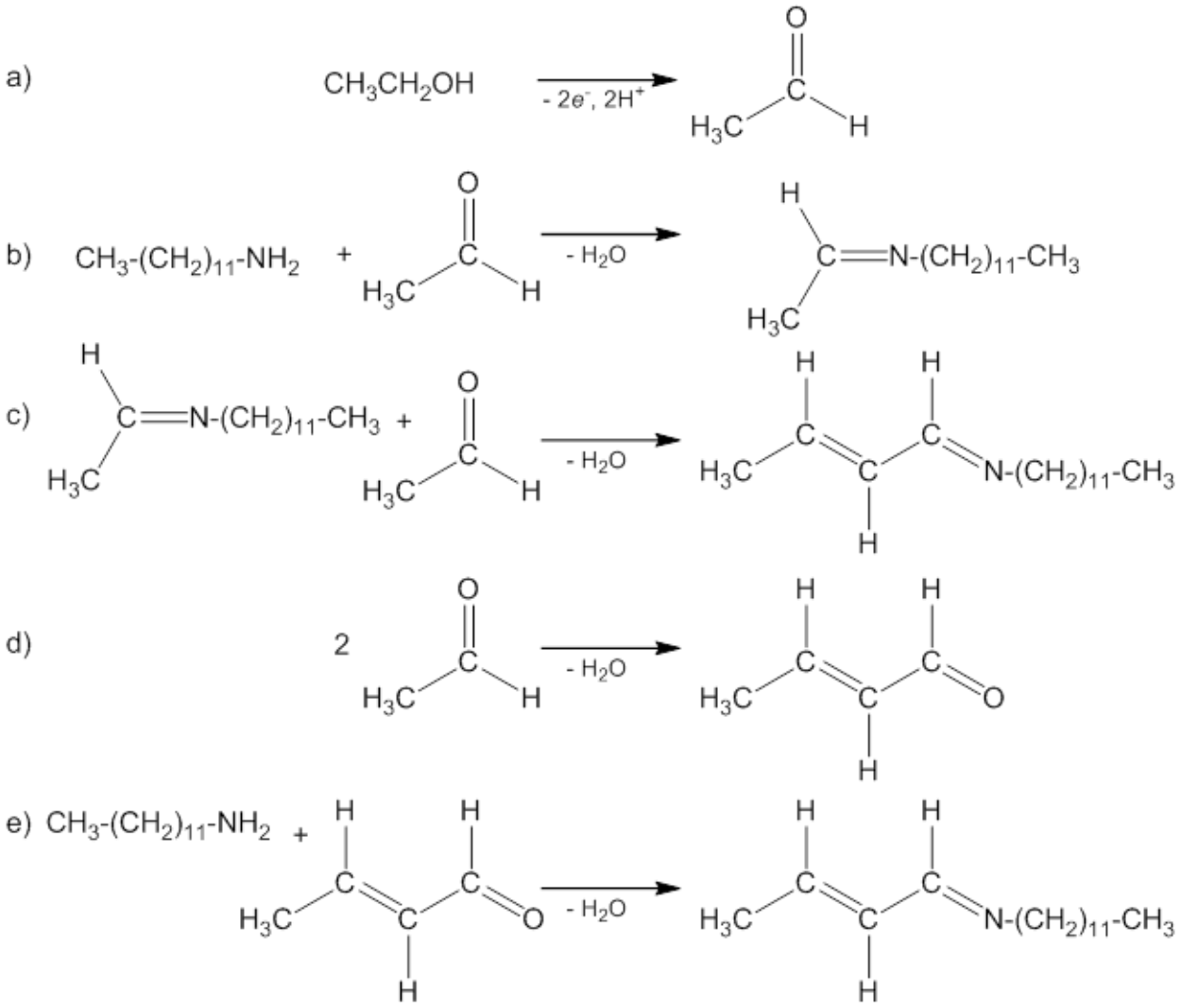

Scheme 2.1. (a) Oxidation of ethanol to acetaldehyde.

(b) Condensation of dodecylamine and acetaldehyde to yield 1-dodecanamine-*N*-ethylidene.

(c) Condensation of 1-dodecanamine-*N*-ethylidene and acetaldehyde.

(d) Self-condensation of acetaldehyde to yield crotonaldehyde.

(e) Condensation of dodecylamine and crotonaldehyde.

2.2.4 *Synthesis of Photolysis Products*

To confirm the photolysis product was 1-dodecanamine, *N*-ethylidene, an authentic sample was independently synthesized from equimolar quantities of the dodecylamine capping ligand and acetaldehyde. A GC/MS chromatogram of the crude product contained peaks at 7.8 and 8.4 minutes, correlating to dodecylamine and the photolysis product (Figure 2.6). The mass spectra of the peaks at 7.8 and 8.4 minutes (not pictured) matched those of dodecylamine and the photolysis product, providing strong evidence for that 1-dodecanamine, *N*-ethylidene is produced during photoreduction of ZnO NCs.

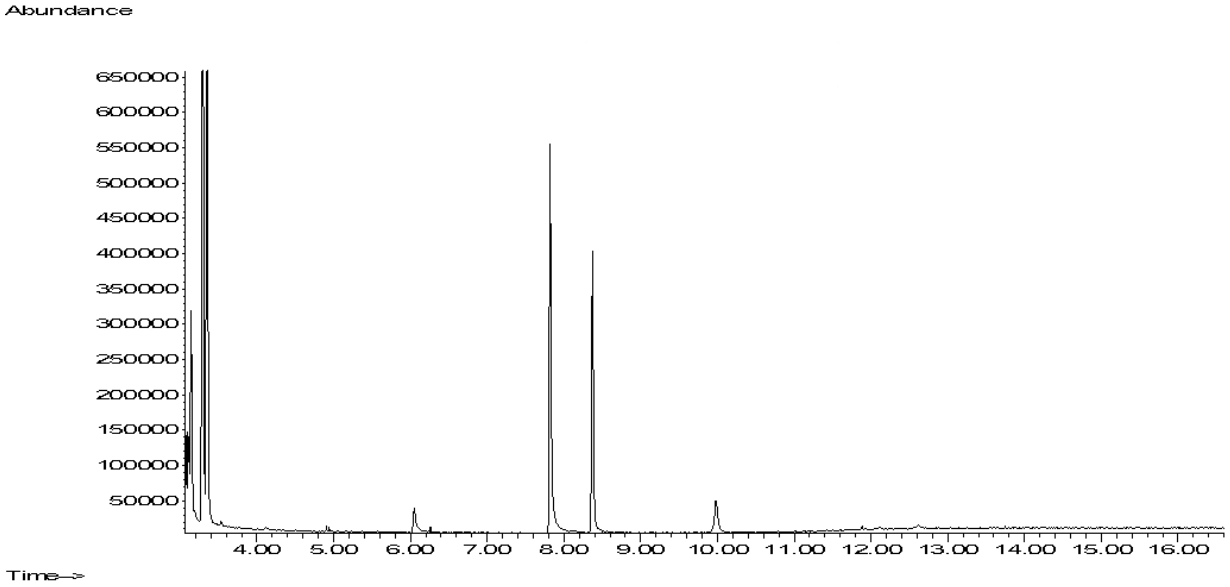

Figure 2.6. GC/MS chromatogram of oil obtained from condensation of dodecylamine (7.8 minutes) and acetaldehyde to form 1-dodecanamine, *N*-ethylidene (8.4 minutes).

The ^{1}H NMR spectra of dodecylamine and the oil of 1-dodecanamine, *N*-ethylidene synthesized with 1.5 times excess acetaldehyde were obtained. The NMR spectrum of the crude product did contain signals for dodecylamine but also new signals (q 7.65 ppm; t 3.29 ppm; and d 1.88 ppm) that are consistent with an imine product (Fig 2.7).[12] NMR spectra obtained from photo-reduced ZnO solutions show small differences from un-photolyzed solutions; signals from 1-dodecanamine, *N*-ethylidene have not been observed.

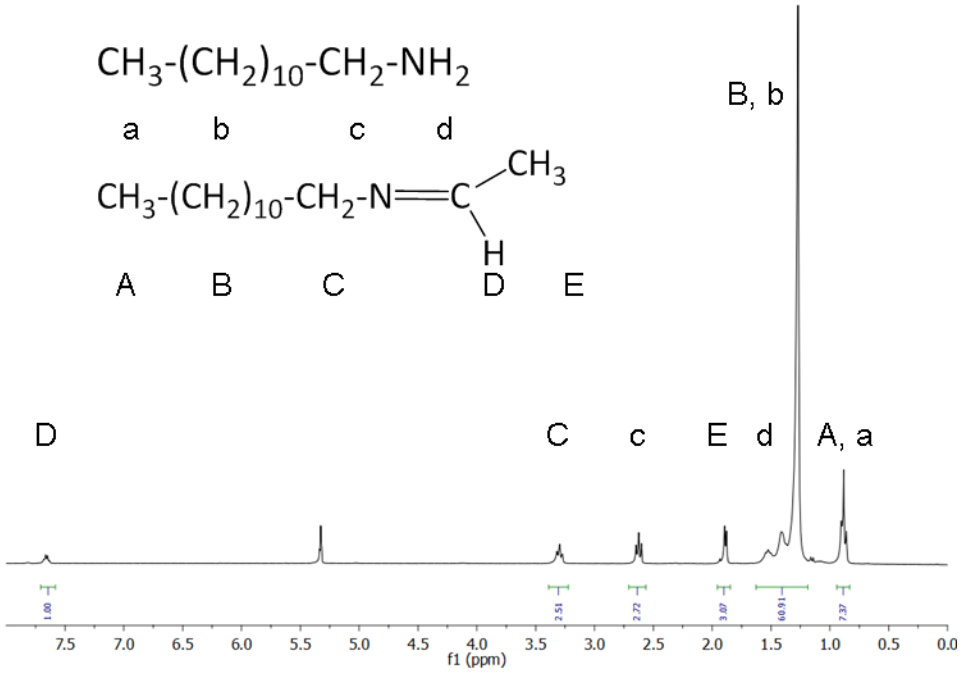

Figure 2.7. NMR spectrum of 1-dodecanamine, *N*-ethylidene reaction mixture in dichloromethane-d_2. Signals associated with dodecylamine starting material and 1-dodecanamine, *N*-ethylidene product are labeled with lower and upper case letters respectively.

2.2.5 *Exploring the role of ethanol in the photoreduction of ZnO NCs*

To further investigate the role of ethanol in photoreduction of ZnO NCs, the preparation of the NCs was modified to minimize exposure to ethanol. In a typical hydrolytic synthesis, ethanolic tetramethylammonium hydroxide is dripped into zinc acetate dissolved in a dimethyl sulfoxide/ethanol solution. The NC are then precipitated with ethyl acetate and washed twice with ethanol and *n*-heptane to remove residual zinc acetate. After the NCs are capped with dodecylamine they are precipitated with ethanol prior to resuspension in toluene. To minimize NC ethanol exposure and hopefully displace ethanol from the NC surface, acetonitrile and benzene were substituted for ethanol and *n*-heptane, respectively. The UV-vis absorption spectrum of the uncharged ZnO NPs prepared using the "low ethanol" method was similar to those obtained from the typical preparation.

A solution of the "minimal ethanol" NCs was split into three equal volumes (2.4 mL) in Kontes cuvettes and each was spiked with an equal volume (100 µL) of toluene, ethanol, or ethanol-d_6. The absorbance spectrum of each sample was obtained before and after 30 minutes of

photolysis to monitor band-edge bleaching upon photoreduction; all of the samples displayed a band edge bleach, indicating all of them were reduced. The samples were prepared for GC/FID analysis as described in the experimental section. The chromatogram for the sample spiked with toluene displayed no peak for 1-dodecanamine, *N*-ethylidene, while the samples spiked with proteo and duetero ethanol displayed overlapping peaks with retention times of 6.9 minutes (Figure 2.8). The retention time for 1-dodecanamine-*N*-ethylidene is later than in previous GC/FID chromatograms because the GC temperature program was altered to match that used with the GC/MS instrument.

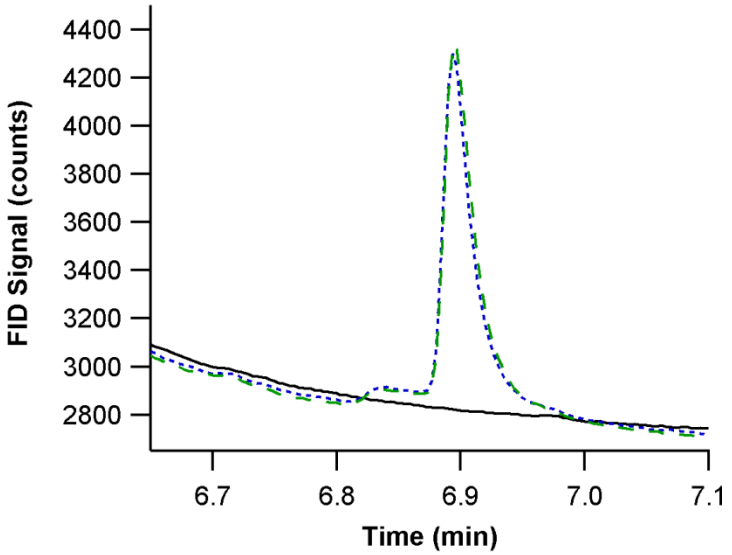

Figure 2.8. GC/FID chromatograms of the supernatant of photolyzed "low ethanol" ZnO NC solutions. The solutions were spiked with toluene (black, solid), ethanol (blue, dotted), and ethanol-d_6 (green, dashed) prior to photolysis.

The samples analyzed by GC/FID were diluted and analyzed by GC/MS. Again the peak attributed to 1-dodecanamine, *N*-ethylidene was not observed in the sample spiked with toluene. The chromatograms of the samples spiked with proteo and duetero ethanol both contained peaks with retention times of 8.4 minutes. For the proteo sample, the mass spectrum of the peak at 8.4 minutes was almost identical to that observed in previous samples. The mass spectrum for the 8.4 minute peak in the chromatogram of duetero sample was similar to the proteo, but most of the ion peaks had been shifted by one amu, indicating that a single deuterium was incorporated into the product (Fig 2.9). This is consistent with the proposal that ethanol is

oxidized during the photoreduction of ZnO NCs and that the oxidation product, acetaldehyde, condenses with the dodecylamine capping group yielding 1-dodecanamine, *N*-ethylidene. The oxidation of ethanol-d_6 could lead to acetaldehyde-d_4, so one may expect to see a 4 amu peak shift from the condensation of the acetaldehyde-d_4 with the dodecylamine. The 1 amu peak shift suggests that the methyl group from the acetaldehyde derived side of 1-dodecanamine, *N*-ethylidene is lost upon ionization.

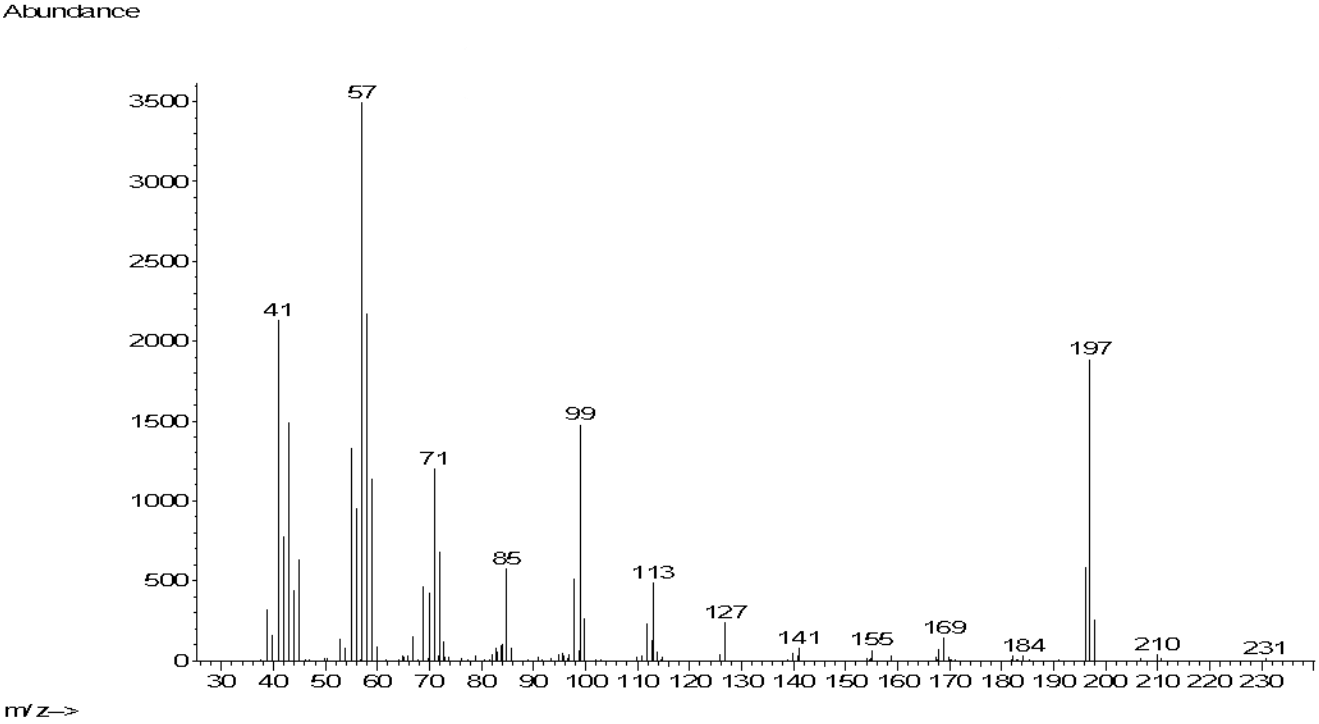

Figure 2.9. Mass Spectrum of the peak with a retention time of 8.4 minutes from the supernatant of the "low ethanol" ZnO NC solution spiked with ethanol-d_6. Most of the ion signals have been shifted by 1 amu (i.e. 196 to 197; 168 to 169).

2.2.6 *Quantifying 1-dodecanamine, N-ethylidene and Conduction Band Electrons.*

During the photoreduction of ZnO NCs, each ethanol molecule that is oxidized should provide two electrons and two protons to an NC. To test this hypothesis, two methods were used to correlate the number of conduction band electrons and the amount of DDI present in solution. In both methods the titration of electrons was performed the same way. In the first method the quantification of DDI was performed using a calibration curve, while in the second method, the method of standard additions was used.

In the first method, a sample of ZnO was split into 6 aliquots. The first aliquot was photolyzed, the second was left unphotolyzed, and the remaining four were reserved to make the calibration curve The photoreduced solution of ZnO NCs was titrated with the hydrogen atom abstractor 2,4,6-tri-*tert*-butyl-phenoxyl ($^{t}Bu_3ArO^{\bullet}$)[13,14] to quantify the number of conduction band electron (Figure 2.10). The titration was monitored by the loss of the absorption at 850 nm (inset, squares) that is attributed to the presence of electrons in the conduction band of ZnO NC and the by subsequent appearance of the peak at 402 nm (inset, triangles) from the presence of excess $^{t}Bu_3ArO^{\bullet}$. From this titration it was determined that 2.1 µmoles of electrons were produced during photolysis.

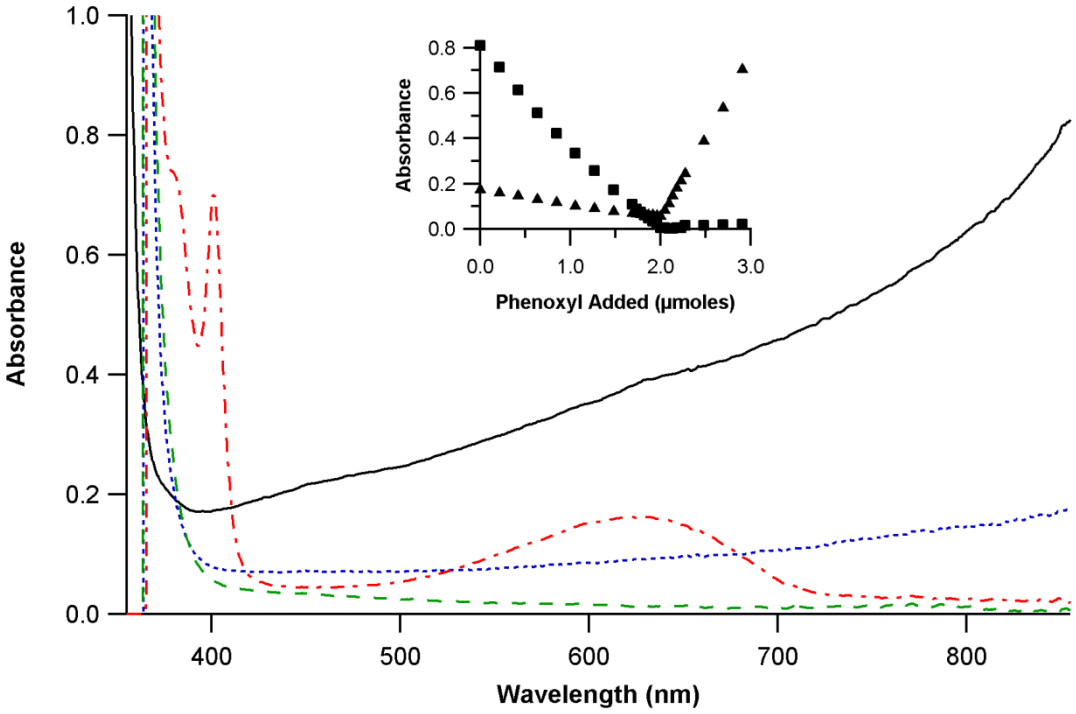

Figure 2.10. Titration of reduced ZnO NCs with $^{t}Bu_3ArO^{\bullet}$ to quantify electrons. Spectra of the reduced ZnO NC solution before titration (black, solid), about 80% complete (blue, dotted), 100% complete (green, dashed) and with excess $^{t}Bu_3ArO^{\bullet}$ (red, dotted & dashed). The inset is the absorbance at 850 nm (squares) and 402 nm (triangles) over the course of the titration plotted versus moles of $^{t}Bu_3ArO^{\bullet}$ added.

Following the titrations, the four aliquots reserved to make the DDI calibration curve were spiked with known amounts of acetaldehyde. The supernatant was obtained and prepared for GC/FID analysis in the same manner as the photoreduced sample. Using the obtained calibration curve the concentration of DDI in the supernatant of the photoreduced sample was determined to be 147 µM, and from back calculation, there were 1.8 µmoles in the photolyzed solution before titration. The ratio of titrated electrons, 2.1 µmoles, with the measured amount of DDI from this experiment was 1.2. This method was abandoned because there was no way to verify if all the acetaldehyde added to samples for the calibration curve had been converted into DDI.

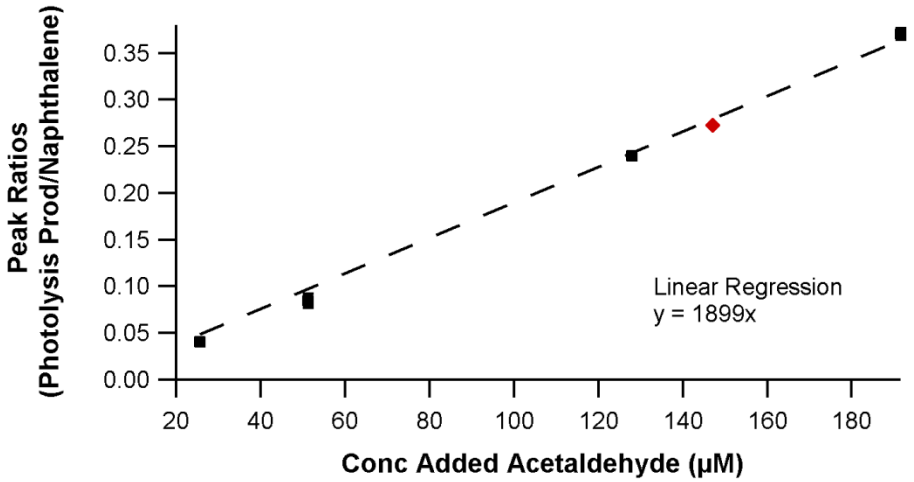

Figure 2.11. Calibration curve for quantification of 1-dodecanamine, *N*-ethylidene. Ratio of the DDI to naphthalene internal standard plotted against the concentration of added Acetaldehyde. The red diamond indicates that the concentration of DDI present in the supernatant of the photoreduced ZnO sample to be 147 µM assuming that all the added acetaldehyde converts to DDI.

The results from the calibration curve experiment and four experiments on three different batches of NCs using the method of standard addition to quantify the DDI are summarized in Table 2.1. For the first batch on ZnO NCs the electron to DDI ratio was greater than two. Two other batches provided electron to DDI ratios of 1.2 and 2.4 respectively. While no strong conclusion can be drawn from this data it is reassuring that the measured quantities of electrons and DDI were close to the two-to-one ratio one would expect.

Table 2.2. Correlation of Measured CB electrons and 1-dodecanamine, *N*-ethylidene

NC Batch	Method	Electrons (µmoles)	DDI (µmoles)	Ratio
MB1198	Regression	2.1	1.8	1.2
MB2006	Standard Add.	1.8	0.73	2.4
MB2006	Standard Add.	2.0	0.95	2.1
MB2022	Standard Add.	1.9	1.6	1.2
MB2036	Standard Add.	2.1	0.89	2.4

2.3 DISCUSSION

Although the hypothesis based on thermodynamics, that the weaker α C–H bonds of dodecylamine should be preferentially oxidized over those of ethanol during the photoreduction of ZnO NCs, the data presented above demonstrates that ethanol is the hole quencher under normal experimental conditions. Recent work on the processes governing multiple reductions during ZnO NCs photolysis, from our collaborators in the Gamelin lab, showed that the ethanol must be preassociating with ZnO and behaving as a "static quencher."[15] One may imagine this preassociation occurring by several different modes of interaction: van der Waals interactions with the ZnO surface and capping ligands; hydrogen bonding between the hydroxyl group of ethanol and surface oxygen; or an acid-base dissociation of ethanol onto the ZnO surface. The latter case, in which ethanol dissociatively adsorbs as a proton and an alkoxide onto oxygen and zinc surfaces sites respectively, has been observed in ultra-high vacuum experiments on single crystals of ZnO.[16]

If the ethanol in our colloidal ZnO system is preassociating with the NC surface in a similar dissociative fashion, the thermodynamics of the system would have to be reconsidered. Computational studies on the oxy anionic substituent effect have demonstrated that BDE of the C–H bond of methanol decreases by 10 to 12 kcal/mol when switching from a proton to the alkali metals sodium and potassium. The BDE of the alkoxide, with no counter ion, has a C–H bond that is 17 kcal/mol weaker than that of methanol.[17] Assuming this trend holds for ethanol, dissociative adsorption onto ZnO could attenuate the α C–H bond strength of ethanol below that of the dodecylamine.[18] Having redefined what potential hole quenchers are available to the photolyzed ZnO NCs, our initial hypothesis seems to hold. The molecule (or molecular fragment) with weaker α C–H bond will be oxidized during photoreduction.

The mechanism by which the acetaldehyde and the dodecylamine condense is unclear. Assuming the ethanol adsorbed in a dissociative manner, acting as an X type ligand, the acetaldehyde obtained from its oxidation would act as an L type ligand, which would be more liable giving it the ability to react with the dodecylamine. Given the nonpolar solvent toluene, the water molecule from this reaction would most likely adsorb to the surface of the NC in place of the acetaldehyde. The product from the condensation of two acetaldehyde molecules and the dodecylamine capping ligand most likely occurs with the first condensation occurring between the amine and one of the aldehydes.

While the experiments attempting to correlate the CB electrons in photoreduced ZnO with the DDI did not lead to a strong conclusion, the fact that they were within range is reassuring that the developed methods were sound. Taken with the results from the "low ethanol" experiments, in which ZnO was able to be photoreduced in the absence of ethanol, it is not surprising that a consistent ratio of electrons to DDI was obtained. While a hole trap was not identified in above mentioned case, it could presumably have been water, other trace alcohols, or DDA, although no evidence was found to support the later.

As researchers move from fundamental studies of nanomaterials, such as the ones described here, to more applied studies for developing these materials as catalysts, an intimate understanding of the redox chemistry is needed. If researchers wish to use nanomaterial catalysts to produce fuel from the reduction of protons to H_2 or CO_2 to methanol, they must know where there reducing and oxidizing equivalents are ending up. An example of this has been described in which the capping ligands stabilizing a nanorod catalyst ended up as acting as a sacrificial reductant.[19]

2.4 CONCLUSIONS

The product from photoreduction of ZnO NCs was determined to be acetaldehyde, from the oxidation of ethanol remaining from synthesis. The acetaldehyde was not observed experimentally as it condenses with the capping ligand, dodecylamine to yield 1-dodecanamine, *N*-ethylidene. This product was detected by GC/FID, GC/MS and ESI-MS and confirmed through comparison of an authentic sample.

2.5 EXPERIMENTAL

2.5.1 *General Considerations*

The synthesis and characterization of ZnO NCs is described in Chapter 1. Solutions of ZnO NCs were stored in a freezer at -35 °C in a N_2 filled glovebox and sealed in gas-tight Kontes cuvettes prior to photolysis. Unless otherwise noted, all reagents were purchased from Aldrich and all solvents were purchased from Fisher Scientific. Absolute ethanol was purchased from Decon. Toluene-d_8, benzene-d_6, and ethanol-d_6 were purchased from Cambridge Isotopes Laboratories. The ethanol-d_6 was used as received. The toluene-d_8 and benzene-d_6 were dried over NaK and stored of molecular sieves. Anhydrous toluene was obtained from a Seca SolventSystem using a Grubbs-type catalyst.

2.5.2 *Instrumentation and Measurements*

GC/FID measurements were made on an HP 5890 Gas Chromatography system equipped with an Agilent J&W DB-5 column packed with (5%-phenyl)-methylpolysiloxane. A method was developed to detect the dodecanenitrile in solutions of dodecylamine in less than ten minutes to allow for the screening of many samples. The carrier gas was helium and the FID was run with hydrogen gas at 6 psi. The injector and detector temperatures were held at 280 and 320 °C respectively. The initial column temperature of 140 °C was held for 3.5 minutes before being increased to 175 °C at a rate of 45 °C/min. This temperature of 175 °C was maintained for one minute before being increased to 260 °C at a rate of 50 °C/min, at which it was held for 1.5 minutes, Figure 2.12.

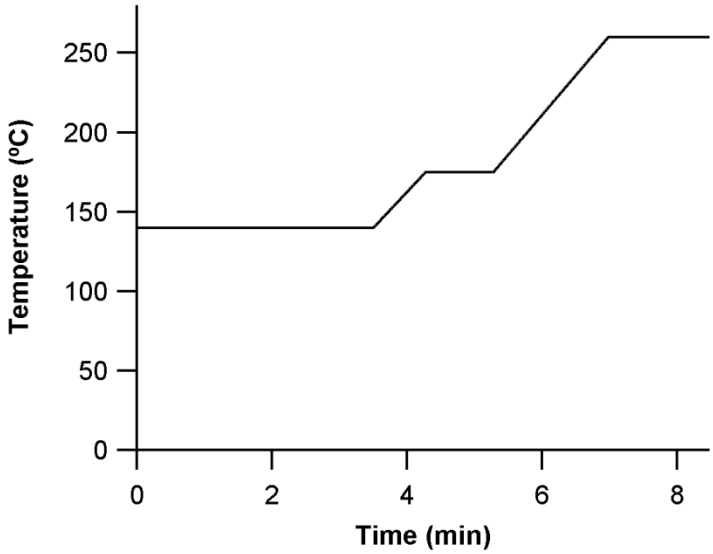

Figure 2.12. GC temperature program for analysis of capping ligand solutions

GC/MS analysis was performed on an HP-5971A mass spectrometer with an HP 5890 gas chromatograph equipped with an Agilent J&W DB-5 column (5%-phenyl)-methylpolysiloxane and an HP 7673A auto sampler. Samples (1 μL) were introduced to the column in split injection mode. The injection inlet was held at 250 °C and the MS interface at 280 °C. The initial oven temperature was 70 °C and was programmed to 300 °C at a rate of 20 °C min^{-1} and held at 300 °C for five minutes. Mass spectra were obtained starting at three minutes and scanning a range of 35-550 m/z.

ESI/MS analysis was performed on a Bruker Esquire Ion Trap Mass Spectrometer with an HP 1100 liquid chromatograph. Samples were injected in-line using a carrier solvent of 99% acetonitrile and 1% acetic acid. The analyses were run in positive ion mode, scanning from 50 to 1000 m/z, with a capillary exit of 90.0 V.

Electronic absorption spectra were obtained using a Hewlett-Packard 8453 diode-array UV-visible spectrophotometer. Photoreduction of the experimental solutions was achieved using an Oriel 200 W Hg/Xe arc lamp (Model 66056) and power supply (Model 68742, operating at 6 amps). Optical titrations were performed in an N_2 filled glovebox using an Ocean Optics USB4000 spectrometer configured with an XR1 grating for extended range, and a DT-Mini-2-GS light source.

2.5.3 *Analysis of Dodecylamine Capping Ligand by GC/FID*

In a 20 mL scintillation vile, several grams of dodecylamine were heated at 165 C for 15 minutes to simulate the conditions experienced during NC capping. As received dodecylamine (63 mg, 68 mM), heated dodecylamine (57 mg, 62 mM), dodecanenitrile (54 mg, 60 mM), and naphthalene (39 mg, 61 mM) were dissolved with toluene in 5 mL volumetric flasks to prepare stock solutions for GC-FID analysis. From these stock solutions four samples all containing 880 µL of the as received dodecylamine and 9.8 µL naphthalene stocks with 0, 4, 10 and 27 µL additions of the dodecanenitrile stock were prepared to determine dodecanenitrile concentration in the as received dodecylamine. A similar set of samples was prepared for the heated amine, only changing the volume of the heated dodecylamine stock to 960 µL. These solutions had 30 mM dodecylamine, 0.3 mM naphthalene, and 0, 0.12, 0.3, and 0.8 mM dodecanenitrile respectively. These samples were analyzed by three separate 1 µL injections using the GC/FID method described in section 2.5.2. The naphthalene and dodecanenitrile peaks were integrated from 2.89 to 3.01 minutes and 5.43 to 5.51 minutes respectively. The concentration of dodecanenitrile in the starting material samples was calculated by the method of standard additions, as the x-intercept for the linear fit to the plot of the ratio of the naphthalene peak to the dodecanenitrile peak versus added concentration of dodecanenitrile. The ratio of the naphthalene to dodecanenitrile peaks was used to account for variations introduced through manual injection of the 1 µL sample volume.

2.5.4 *GC/FID Analysis of Unphotolyzed and Photolyzed ZnO Solutions.*

A 3 mL aliquot of ZnO NCs (3.5 nm diameter, 0.4 mM) was diluted to 6 mL. Half of this volume was set aside and the other 3mL were sealed in an airtight Kontes cuvette with a Teflon coated magnetic stirrer and photolyzed for 30 minutes. After photolysis both samples were open to air and 3 mL of acetonitrile was added to each, precipitating the NCs. The solutions were transferred to test tubes and the NCs were pelleted by centrifugation for 20 minutes at 3,400 rpm. The supernatant was removed and filtered with Celite® 545 and glass wool. Four samples of the unphotolyzed solution were prepared in 1 mL volumetric flasks using 500 µL of the appropriate supernatant, 4.9 µL of a 61 mM naphthalene stock solution and 0.0, 2.0, 5.0, and 8.3 µL of a dodecanenitrile stock solution. Four samples of the photolyzed solutions were prepared in the

same manner. All of the samples were analyzed by three separate 1 µL injections using the GC/FID method described in section 2.5.2.

A 2 mL aliquot of ZnO NCs (3.5 nm diameter, 0.40 mM) was diluted to 4 mL with toluene. This sample was split in half as described previously. The half of the sample placed in the Kontes cuvette (fitted with a 14/20 ground glass joint) was brought through five photolysis cycles. The cycling was achieved by opening the sample to air after one 30 minute cycle to allow for NC oxidation followed by three bubble-degassing cycles on a Schlenk line. Once the photolysis cycles were complete the ZnO NCs in the unphotolyzed and photolyzed samples were pelleted as described above. The supernatant of the photolyzed and unphotolyzed samples were spiked with naphthalene and dodecanenitrile for GC/FID analysis as described above. All of the samples were analyzed by three separate 1 µL injections using the GC/FID method described in section 2.5.2.

A 4.5 mL aliquot of ZnO NCs (4.1 nm diameter, 0.46 mM) was diluted to with toluene to a total volume of 9.0 mL. Three 2.5 mL volumes of the NC solution were placed in Kontes cuvettes and 1.5 mL was placed in a scintillation vial. One of the cuvettes was brought through a 30 minute photolysis. The second and third cuvettes were brought through two and four photolysis cycles respectively, as described above. The ZnO NCs were pelleted for the four solutions as described previously. Samples for GC/FID analysis were prepared from 500 µL of the solution and 4.9 µL of a 61 mM naphthalene stock solution in 1 mL volumetric flasks; no dodecanenitrile was added to these samples. All of the samples were analyzed by three separate 1 µL injections using the GC/FID method described in section 2.5.2.

2.5.5 *Identification of the Photolysis Products with GC and ESI MS*

Portions (200 µL) of samples prepared for GC/FID analysis, made from the supernatant of ZnO NCs that were brought through zero and four photolysis cycles, were diluted with toluene in 1 mL volumetric flasks. GC/MS chromatograms of the two samples were obtained as described in section 2.5.2.

A (2 µL) portion of a sample prepared for GC/FID analysis, made from the supernatant of ZnO NCs that were brought through five photolysis cycles, was diluted with 1000 µL with a 99% acetonitrile and 1% acetic acid solution. MS data from the sample was collected as described in section 2.5.2.

2.5.6 *Synthesis and characterization of 1-dodecanamine, N-ethylidene*

A sample of 1-dodecanamine, *N*-ethylidene was independently synthesized by the addition of a molar equivalent of acetaldehyde (600 μL, 0.01 mol) to a solution of DDA (2.0g, 0.01 mol) in CH_2Cl_2 (100mL) on 3Å molecular sieves on ice over the period of an hour. The reaction mixture was transferred to a round bottom flask and the solvent was removed by rotary evaporation and the crude product, a yellowish paste, was placed under high vacuum for an hour and stored at -20 °C overnight.

A pinhead sized quantity of the crude reaction product was dissolved in toluene in a 5 mL volumetric flask with a 24.6 μL spike of 0.061M naphthalene solution. A sample for GC/MS analysis was prepared by diluting 200 μL of that solution to 1000 μL and analyzed by the method described in section 2.5.2. ^{1}H NMR spectra of the crude product were obtained in CH_2Cl_2-d_2 and the amount of 1-dodecanamine, *N*-ethylidene was quantified to be 53% w/w by using hexamethylbenzene as an internal standard.

2.5.7 *Synthesis and experiments with "low ethanol" ZnO NCs.*

Zinc acetate dihydrate (1.00 g, 5.5 mmol) was dissolved in a dimethyl sulfoxide and ethanol mixture (35 and 10 mL) and cooled in an ice bath for 30 minutes. Tetramethylammonium hydroxide pentahydrate (1.34 g, 7.4 mmol) dissolved in ethanol (15 mL) was dripped into the cooled zinc solution over a period of 12 minutes. Ethyl acetate was used to precipitate the ZnO NCs, which were pelleted in test tubes through centrifugation at 3400 rpm. The ZnO NC pellets were suspended in acetonitrile followed by precipitation with benzene and centrifugation to reform the pellets. The acetonitrile/benzene wash step was repeated. The twice washed ZnO NC pellets were then dissolved in hot (160 °C) dodecylamine to cap the NCs with the amine. The capped NCs were then precipitated in acetonitrile, centrifuged into pellets and suspended in toluene. The ZnO NC solution was then bubble degassed on a high vacuum line three times and transferred to an N_2 filled glovebox. The NCs had an average diameter of 3.7 nm determined by UV-Visible spectroscopy and had a concentration of 5.1×10^{-6} as measured by ICP-AES.

An aliquot (4.0 mL) of the "low ethanol" ZnO NCs was diluted with toluene (4.0 mL). This aliquot was divided among three Kontes cuvettes (2.4 mL each) and the three cuvettes were spiked with toluene, ethanol or ethanol-d_6 (100 μL). Each sample was then photolyzed for 30

minutes. The samples were oxidized with air, the NCs were precipitated with acetonitrile, and the supernatant was filtered as described previously. Samples for GC/FID analysis were prepared from the supernatants of the toluene, ethanol, and ethanol-d_6 spiked ZnO NC solutions using 600 µL of the respective supernatant in 1 mL volumetric flasks. The temperature program for GC/FID analysis was altered changed to that used for GC/MS analysis. Portions (400 µL) of the samples prepared for the GC/FID experiments were diluted to 1 mL and analyzed by GC/MS as described in section 2.5.2.

2.5.8 *Quantification of conduction band electrons & 1-dodecanamine, N-ethylidene*

Two ways of correlating the number of conduction band electrons and the 1-dodecanamine, *N*-ethylidene are described. Both methods quantify the electrons by means of titration, but they differ in how the 1-dodecanamine, *N*-ethylidene is quantified. The first method involves making a calibration curve by adding known quantities of acetaldehyde to ZnO NC solutions and assuming complete reaction between the aldehyde and dodecylamine capping ligands. The second method involves quantifying synthesized 1-dodecanamine, *N*-ethylidene by NMR and using the method of standard addition.

Method 1: A 4 mL aliquot of ZnO NCs (3.53×10^{-4} M) was diluted to 10 mL with toluene. This diluted ZnO solution was split into two 2.4 mL portions and one 5 mL portion. One of the 2.4 mL portions was photolyzed for 45 minutes. A stock solution of 2,4,6-tri-*tert*-butyl-phenoxyl (^{t}Bu$_3$ArO$^\bullet$)[20] was prepared from 5.7 mg with toluene in a 1 mL volumetric flask (22 mM). A 100 µL portion of the stock was diluted to 500 µL (4.4 mM). The photolyzed and unphotolyzed solutions were titrated with the ^{t}Bu$_3$ArO$^\bullet$ solutions giving 2.1×10^{-6} and 0 moles of electrons respectively.

A stock solution of acetaldehyde was prepared adding 5 µL to a 5 mL volumetric flask with toluene chilled in an ice bath (0.018 M). The remaining 5 mL portion of ZnO NC was further split into four 1 mL portions to prepare a calibration curve for the quantification of the 1-dodecanamine, *N*-ethylidene in the photolyzed sample. Each of the 1 mL ZnO samples was spiked with the acetaldehyde stock (10, 20, 50 and 75 µL) and toluene was added to bring the total sample volumes to 1.4 mL. The ZnO NCs in the titrated (2.2 mL) and calibration curve samples (1.2 mL) were precipitated with equal volumes of acetonitrile and the supernatants were

filtered collected and filtered as described previously. Samples for GC analysis were prepared in 1 mL volumetric flasks using 400 µL of the respective supernatant and a 4.9 µL spike of a naphthalene standard (0.060 M). The samples were analyzed by GC/FID as described above.

Method 2: A fresh batch of 1-dodecanamine, *N*-ethylidene was prepared by the addition of 3 molar equivalents of acetaldehyde (400 µL, 7.2 mol) to a solution of DDA (400 mg, 2.2 mol) in benzene (50 mL), cooled in an ice bath over $MgSO_4$. The reaction mixture was transferred to a round-bottom flask, leaving behind the $MgSO_4$, and the solvent was removed affording an oil with a yellow tinge. A small amount of the fresh DDI was dissolved in benzene-$_{d6}$ (500 µL) containing a hexamethylbenzene (HMB) standard (2.8 mM) internal standard for quantification. A ^{1}H NMR spectrum was obtained on a Bruker AV-500 instrument and the concentration of 1-dodecanamine, *N*-ethylidene was calculated from the 1 H quartet of DDI centered at 7.34 ppm and the 18 H peak of HMB centered at 2.13 ppm. The concentration of DDI in solution was 74 mM, which means the freshly prepared oil was 65% DDI by weight.

A solution of ZnO NPs was prepared by diluting 3 mL (4.18×10^{-4}) to 8 mL with toluene. Three 2.4 mL aliquots were placed in a Kontes cuvettes and one was photolyzed for 30 minutes. A stock solution of ^{t}Bu$_3$ArO$^\bullet$ was prepared from 4.2 mg with toluene in a 1 mL volumetric flask (16 mM). A 100 µL portion of the stock was diluted to 500 µL (3.2 mM). The unphotolyzed and photolyzed samples were titrated with the ^{t}Bu$_3$ArO$^\bullet$ solutions giving 1.8×10^{-6} and 0 moles of electrons respectively. The ZnO NCs of the photolyzed and unphotolyzed samples were precipitated with equal volumes of acetonitrile and the supernatant was removed and filtered as previously described. Stock solutions of naphthalene (43 mg) and DDI (92 mg) were prepared in 5 mL volumetric flasks with toluene. Samples to quantify the DDI by the method of standard addition were prepared from 600 µL of the supernatant, 5 µL of the naphthalene stock and 0, 2, 5, or 10 µL spikes of the DDI stock. The samples were analyzed by the GC/FID method described previously and the concentration of DDI in the photolyzed solution was determined to be 3.7×10^{-4} M.

2.6 NOTES

(1) Bahnemann, D. W.; Kormann, C.; Hoffmann, M. R. *J. Phys. Chem.* **1987**, *91* (14), 3789–3798.

(2) Haase, M.; Weller, H.; Henglein, A. *J. Phys. Chem.* **1988**, *92* (2), 482–487.

(3) Kamat, P. V.; Patrick, B. *J. Phys. Chem.* **1992**, *96* (16), 6829–6834.

(4) Shim, M.; Guyot-Sionnest, P. *J. Am. Chem. Soc.* **2001**, *123* (47), 11651–11654.

(5) Schwartz, D. A.; Norberg, N. S.; Nguyen, Q. P.; Parker, J. M.; Gamelin, D. R. *J. Am. Chem. Soc.* **2003**, *125* (43), 13205–13218.

(6) Norberg, N. S.; Gamelin, D. R. *J. Phys. Chem. B* **2005**, *109* (44), 20810–20816.

(7) Liu, W. K.; Whitaker, K. M.; Kittilstved, K. R.; Gamelin, D. R. *J. Am. Chem. Soc.* **2006**, *128* (12), 3910–3911.

(8) Wang, F.; Tang, R.; Kao, J. L.-F.; Dingman, S. D.; Buhro, W. E. *J. Am. Chem. Soc.* **2009**, *131* (13), 4983–4994.

(9) Luo, Y.-R. *Comprehensive handbook of chemical bond energies*; CRC press, 2007.

(10) Hayoun, R. Studies of Metal Oxides in Organic Redox Reactions: Zinc Oxide Nanoparticles as Chemical Reductants In Electron Transfer and Hydrogen Atom Transfer Reactions and the Use of Osmium Tetroxide to Oxidize Higher Alkanes. Dissertation, University of Washington: Seattle Washington, 2011.

(11) Recovery of the DDA ligands was attempted by addition of strongly acidic water to the toluene NC solutions in hopes of dissolving the NCs. This led to a biphasic mixture, with an emulsion (presumably of the DDA ligands) which was difficult to recover. Alternatively, DDA recovery by NC precipitation was attempted by addition of EtOH to the toluene NC solutions. While the solutions became cloudy upon addition of EtOH, NC precipitation was not achieved.

(12) Guillemin, J.-C.; Denis, J.-M. *Tetrahedron* **1988**, *44* (14), 4431–4446.

(13) Schrauben, J. N.; Hayoun, R.; Valdez, C. N.; Braten, M.; Fridley, L.; Mayer, J. M. *Science* **2012**, *336* (6086), 1298–1301.

(14) Valdez, C. N.; Braten, M.; Soria, A.; Gamelin, D. R.; Mayer, J. M. *J. Am. Chem. Soc.* **2013**, *135* (23), 8492–8495.

(15) Cohn, A. W.; Janßen, N.; Mayer, J. M.; Gamelin, D. R. *J. Phys. Chem. C* **2012**, *116* (38), 20633–20642.

(16) Vohs, J. M.; Barteau, M. A. *Surf. Sci.* **1989**, *221* (3), 590–608.

(17) Steigerwald, M. L.; Goddard, W. A.; Evans, D. A. *J. Am. Chem. Soc.* **1979**, *101* (8), 1994–1997.

(18) It is also worth noting that that the BDE of the amine will increase on coordination, as the N lone pair is occupied with the Zn and not available to stabilize the carbon radical upon hole quenching.

(19) Acharya, K. P.; Khnayzer, R. S.; O'Connor, T.; Diederich, G.; Kirsanova, M.; Klinkova, A.; Roth, D.; Kinder, E.; Imboden, M.; Zamkov, M. *Nano Lett.* **2011**, *11* (7), 2919–2926.

(20) Manner, V. W.; Markle, T. F.; Freudenthal, J. H.; Roth, J. P.; Mayer, J. M. *Chem Commun* **2008**, No. 2, 256–258.

Chapter 3. EXPLORING THE FACTORS AFFECTING THE RATE OF PCET FROM REDUCED ZINC OXIDE NANOCRYSTALS TO HYDROGEN ATOM ACCEPTORS

3.1 INTRODUCTION

Understanding the factors that affect the rate of electron transfer between metal-oxide materials and redox active molecules is a rich scientific field. Much of the work has been focused on ET from photo-excited, surface-attached dyes to semiconductor metal-oxide electrodes in the context of dye sensitized solar cells (DSSCs), with nanocrystalline ZnO, TiO_2, and SnO_2 being the materials of choice.[1,2,3] The forward ET reactions (excited dye reducing MO_x electrode) are ultrafast occurring on the femto to pico second timescale, while the back ET (reduced NC to oxidized dye) occurs on the nano to microsecond scale.[4] There are few reported charge transfer studies with colloidal nanocrystals as opposed to films composed of them. One group of researchers studied the effect of NC size on ET from surface attached zinc porphyrins to size-selected colloidal ZnO NCs. They observed that electron injection occurred faster for larger NCs and attributed this to a higher density of conduction band states for larger NCs.[5] In early work on ZnO NCs (before the advent of DSSCs), Haase, Weller, and Henglein studied the reaction of photoreduced ZnO NCs with oxygen by following the recovery the band-edge bleach. They found that the rate constant for the oxidation of the photoreduced 1.7 nm NCs was 3.2×10^6 $M^{-1}s^{-1}$ and that it was about 50 times slower for 4.0 nm NCs.[6]

Due to the fast timescale of these ET reactions they are often initiated with lasers and studied by time resolved spectroscopies, following spectral changes associated with changes in oxidation state of the products and reactants. These techniques are often called Laser Flash Photolysis (LFP) or Transient Absorption Spectroscopy (TA). In the nanosecond and slower time scales, researchers use commercially available and custom built systems which generally contain a laser (often referred to as the pump), a light source (referred to as the probe), a monochromator, a detector/amplifier, and oscilloscope and a computer to digitize the signal and control the time

of the pump and probe. In a basic experiment, the probe light is shined on the sample for a short period (5 to 10% of the collection time) to obtain an initial absorbance or voltage before the laser pumps the sample at an angle perpendicular to the probe light. The laser pulse excites the dye molecules or causes the photoreduction of NCs which is observed by an increase or decrease in absorbance. This absorbance change is monitored over time as the photo-excited dye molecules or reduced NCs go on to react. The time resolved data are displayed as the difference in absorbance (ΔA) versus time and the ΔA is usually determined by software using equation 3.1, where V_0 is the voltage before the laser flash and V_t is the voltage after the flash.

$$\Delta A = \log \frac{V_0}{V_t} \qquad (3.1)$$

Early work with ZnO NCs in our lab demonstrated that upon photoreduction, the NCs could act as net hydrogen atom donors, providing electrons and protons to the stable organic radicals 2,4,6-tri-tertbutyl-phenoxyl (^{t}Bu$_3$ArO$^\bullet$) (see Figure 3.1) and 2,2,6,6-tetramethyl-piperidin-1-yl-oxyl (TEMPO). TA measurements following the band-edge bleach of the ZnO NCs yielded bimolecular rate constants of 3.0 ± 0.7 × 10^7 and 1.8 ± 0.4 × 10^3 $M^{-1}s^{-1}$ for the reactions of the photoreduced NCs with ^{t}Bu$_3$ArO$^\bullet$ and TEMPO respectively. A crude experiment where excess dodecylamine capping ligand was added to the NCs and ^{t}Bu$_3$ArO$^\bullet$ reaction mixture demonstrated a retardation in rate. The following chapter describes experiments designed to gain a better understanding how two factors, the average NC size and the capping ligand concentration influence the rate of PCET between photoreduced ZnO NCs and ^{t}Bu$_3$ArO$^\bullet$.

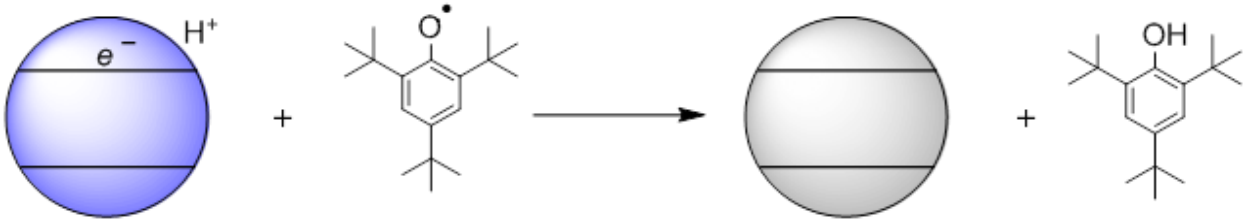

Figure 3.1. Reaction studied in this Chapter; PCET from reduced ZnO NC to ^{t}Bu$_3$ArO$^\bullet$.

3.2 RESULTS

3.2.1 *Measuring PCET Rates with Transient Absorption Spectroscopy*

A method was developed to measure the rate of PCET from photoreduced ZnO NCs to the $^{t}Bu_3ArO^{\bullet}$ radical. Briefly, reaction solutions of ZnO NCs (concentrations in the 1 to 0.1 µM range) and $^{t}Bu_3ArO^{\bullet}$ (concentrations in the 100 to 800 µM range) were prepared in gas-tight fluorescence cuvettes with absorbance values between 0.30 and 0.75 and 355 nm, the wavelength of the laser excitation pulse. Absorbance spectra of the solutions were obtained before and after TA data was collected to monitor the consumption of the $^{t}Bu_3ArO^{\bullet}$ radical, Figure 3.2a. TA data was obtained for each concentration of $^{t}Bu_3ArO^{\bullet}$ prepared, at a single wavelength of 350 nm, monitoring the recovery of band-edge bleach absorbance associated with ZnO NC reduction. As expected, reaction solutions with greater concentrations of the $^{t}Bu_3ArO^{\bullet}$ radical displayed a faster recovery of the band-edge bleach than solutions with lesser concentrations of the hydrogen atom acceptor, Figure 3.2b.

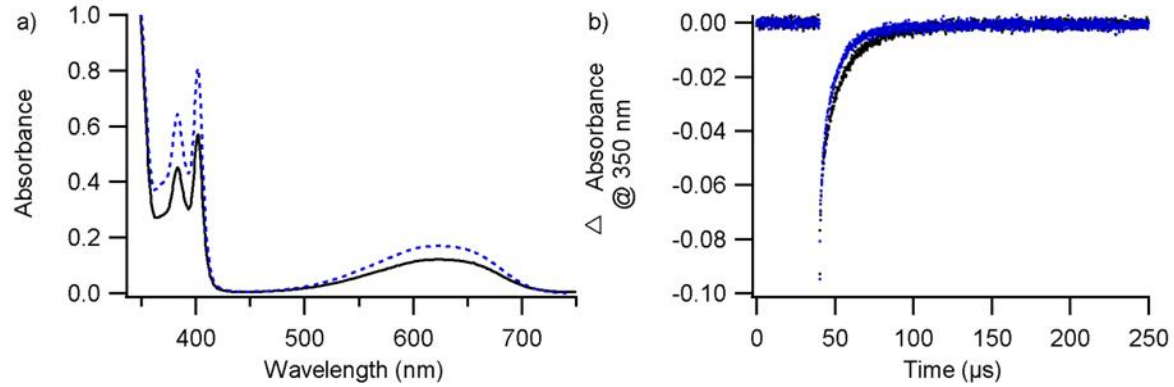

Figure 3.2. a) Spectra of ZnO NCs (1.56 µM) with $^{t}Bu_3ArO^{\bullet}$ at 327 µM (black, solid) and 465 µM (blue, dotted) obtained before TA data collection. b) Kinetic traces of collected at 350 nm correlating with the spectra from samples in (a). The recovery of the band edge bleach from reaction of photoreduced ZnO and $^{t}Bu_3ArO^{\bullet}$ is displayed.

The TA data was imported into SpecFit software and observed rate constants were obtained by fitting the recovery of the bleach to a single exponential function, Figure 3.3a. Second order rate constants were obtained by plotting the observed rates measured under pseudo first order conditions against the concentration of $^{t}Bu_3ArO^{\bullet}$. Error bars (± 2σ) were obtained by

collecting data with four experimental replicates, Figure 3.3b, allowing for comparison of rate constants across several batches of ZnO NCs and under different concentrations of the dodecylamine capping ligand.

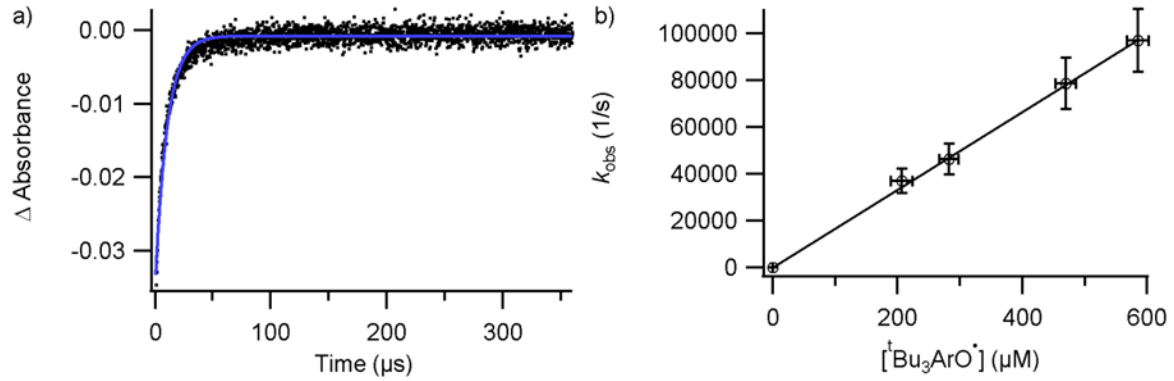

Figure 3.3 a) Band-edge bleach recovery data (black dots) and fit of data (blue line) for reaction of reduced 4.7 nm ZnO NCs (0.43 μM) with ^{t}Bu$_3$ArO$^\bullet$ (588 μM). b) Pseudo first order rate constants obtained from fitting data plotted against concentration of ^{t}Bu$_3$ArO$^\bullet$ to obtain a bimolecular rate constant of $1.68 \pm 0.04 \times 10^8$ $M^{-1}s^{-1}$.

3.2.2 *Effect of the capping ligand concentration on PCET Rate*

Having established a method to measure the rate of PCET with a known error, experiments were performed to determine how the concentration of the dodecylamine capping ligands affects the reaction rate. In one set of experiments, measurements were obtained on solutions with four concentrations of ^{t}Bu$_3$ArO$^\bullet$ and four concentrations of dodecylamine. The observed rate of PCET decreases as the concentration of amine capping ligand increased, Figure 3.4a. At high capping ligand concentration (greater than 17 mM) the reaction did not complete within a time window that was short enough to ensure stability of the probe light (less than 1 ms). Comparing the half-lives of samples with same concentration of ^{t}Bu$_3$ArO$^\bullet$ but different concentrations of dodecylamine demonstrates that the observed half-lives increase in a linear fashion with increasing capping ligand concentration, Figure 3.4b.

Working at capping ligand concentrations below 8 mM, the PCET rate constants for reaction with ^{t}Bu$_3$ArO$^\bullet$ were measured for several batches of ZnO NCs. In each case increasing the concentration of dodecylamine decreases the second order rate constant well beyond the experimental uncertainty, Figure 3.5. Increasing the capping ligand concentration 10 to 50 fold

led to a decrease in rate by factors of ~1.2 to 3.7, Table 3.1. The PCET rate constants always decreased when reaction mixtures were spiked with dodecylamine. The measured decrease in rates was within a factor of 2.5 between the batches that were tested. Replicate experiments on ZnO NCs from the same batch, spiked with the same concentration of dodecylamine, led a decrease in rate that was reproducible within error, as can be seen from the second and third entries in Table 3.1.

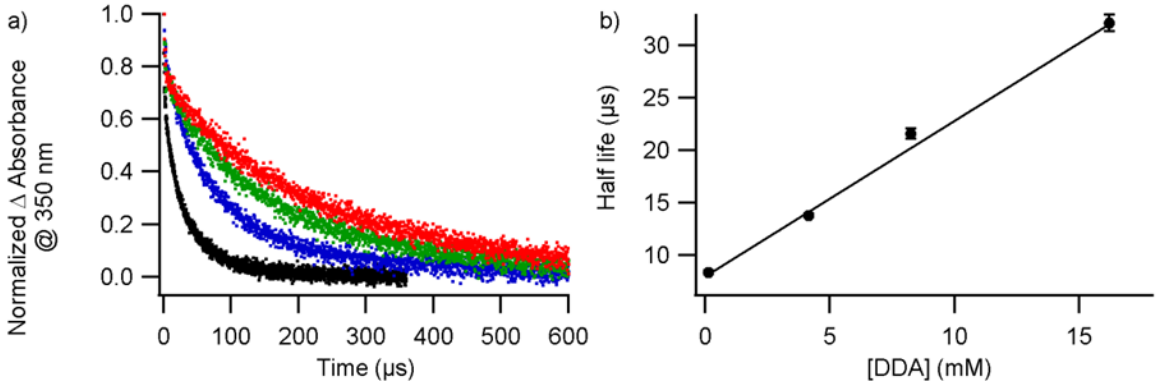

Figure 3.4. a) Normalized kinetic data for the reaction of photoreduced ZnO NCs (4.7 nm, 0.3 μM) with $^{t}Bu_3ArO^{\bullet}$ (306 μM) with different capping ligand concentrations: 0.14 mM, black; 4.14 mM blue; 8.24 green; and 16.2 red. The line has been added to demonstrate linear increase in half-life b) Half-lives from the kinetic traces displayed in panel (error bars ± σ). (a) demonstrating a decrease in observed rate with increasing dodecylamine concentration.

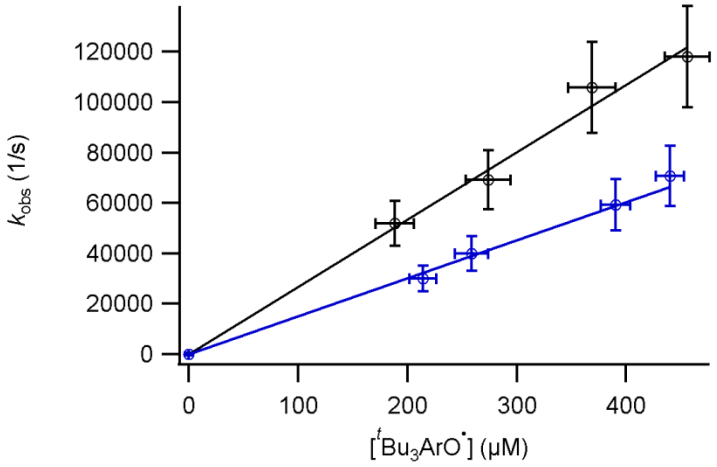

Figure 3.5. Plot of the observed PCET rate constants for reaction of photoreduced ZnO NCs (3.7 nm, 1.56 μM) with ^{t}Bu$_3$ArO$^\bullet$ for NCs with the native, 0.45 mM capping ligand concentration (data points above, black) and with added dodecylamine, 4.49 mM (data points below, blue). The second order rate constants are $2.67 \pm 0.23 \times 10^8$ and $1.51 \pm 0.13 \times 10^8$ $M^{-1}s^{-1}$ respectively.

Table 3.3. Comparing PCET Rates of as Synthesized vs. Added DDA ZnO Nanocrystals

Batch	k_{PCET} ($M^{-1}s^{-1}$)	Capping Ligand Concentration (mM)	Increase in [DDA]	Decrease in k_{PCET}
MB2164	$1.26 \pm 0.11 \times 10^8$	0.14	53	3.17 ± 0.56
	$4.04 \pm 0.37 \times 10^7$	**7.44**		
MB3005	$9.96 \pm 0.87 \times 10^7$	0.16	27	1.75 ± 0.31
	$5.79 \pm 0.52 \times 10^7$	**4.26**		
MB3005	$9.67 \pm 0.97 \times 10^7$	0.16	27	1.44 ± 0.29
	$6.87 \pm 0.70 \times 10^7$	**4.26**		
MB3026	$2.67 \pm 0.23 \times 10^8$	0.45	10	1.79 ± 0.31
	$1.51 \pm 0.13 \times 10^8$	**4.49**		

3.2.3 *Effect of Average NC Diameter on Rate of PCET*

To test what effect the average ZnO NC size has on the rate of PCET, batches of NCs with average diameters ranging from 3.8 to 6.0 nm were prepared as described in section 1.5.2.[7] The NC diameter was changed by varying the length of time the synthesized NCs were held in the molten dodecylamine capping ligands before precipitation with ethanol. The 3.8 nm NCs were

precipitated immediately, while the large NCs were allowed to grow for about 10 minutes. The average NC diameter was estimated from the band edge inflection point as described in section 1.5.3.[8] Rate constants were compiled from the data described in section 3.2.2 for the samples with no added dodecylamine capping ligand or measured in a similar manner. The change in bandgap energy, ΔE_g, was calculated from the average NC size with the Brus Equation, Equation 1.1. This energy was then used to estimate the ΔE_{CB} from Equation 3.1, where m_e and m_h are the effective masses of the electron (0.275) and hole (0.59) in ZnO.

$$\Delta E_{CB} \cong \frac{m_e^{-1}\Delta E_g}{m_e^{-1}+m_h^{-1}} \tag{3.2}$$

Data from the different sized batches of ZnO NCs has been collected in Table 3.2. The bimolecular rate constants for the reaction of photoreduced ZnO with $^{t}Bu_3ArO^{\bullet}$ have been plotted against the ΔE_{CB} and the average NC diameter for each batch of NCs, Figure 3.6. As can be observed the energy of the conduction band, determined from average nanocrystal size, appears to have little effect on the rate of PCET. The 3.8 nm ZnO NCs, with a 0.180 eV greater driving force than the 6.0 nm ZnO NCs, only react about 1.5 times faster than the larger NCs.

Table 3.4. Comparing PCET Rates of ZnO Nanocrystals with Different Average Diameters

Band edge inflection point (nm)	NC diameter (nm)	ΔE_{CB} (eV)	k_{PCET} ($M^{-1}s^{-1}$) × 10^8
352	3.8	0.252	2.67 ± 0.23
356	4.2	0.195	1.30 ± 0.11
360	4.7	0.144	1.45 ± 0.14
364	6.0	0.066	1.66 ± 0.14

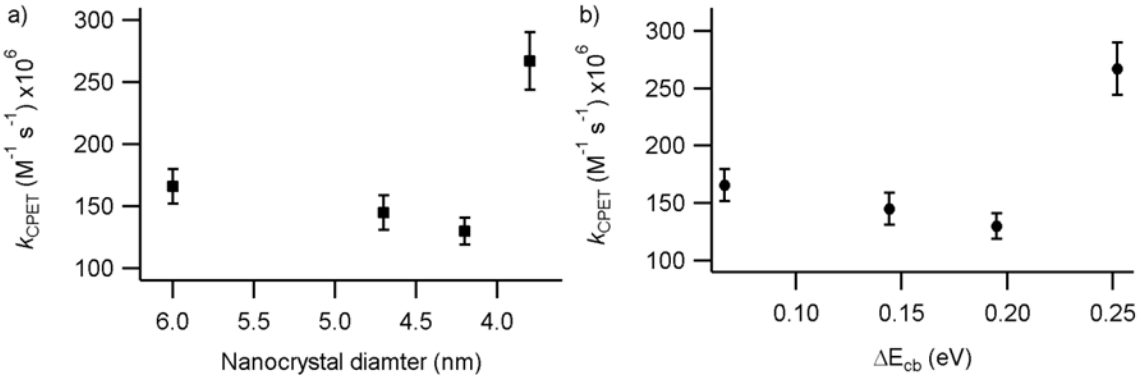

Figure 3.6. Comparison of measured k_{PCET} with the average NC size (a) and the difference in conduction band energy (b).

3.3 Discussion and Conclusions

Several observations can be made from looking at the collection of TA data compiled from several batches of ZnO NCs. As previously reported, the PCET from photoreduced ZnO to $^{t}Bu_3ArO^{\bullet}$ is fast with a bimolecular rate constant of about 1×10^8 $M^{-1}s^{-1}$.[9] The reaction rate is retarded by increasing the concentration of the dodecylamine capping ligand. The decrease in reaction rate is small, about 1.5 times slower with a 10 fold increase in capping ligand, and becomes more pronounced as the concentration of dodecylamine is increased. The NC size, which modulates the NC conduction band energy or reduction potential, has no significant effect on the rate of PCET.

Other researchers have made similar observations about capping ligand concentrations playing a role in the rate of charge transfer between semiconductor nanocrystals and small molecules. Grauer and Alivisatos demonstrated that spiking excess octadecylamine capping ligand into solutions of tungsten oxide (WO_x) nanorods decreased the rate of ET from the nanorods to iron based molecular oxidant.[10] The authors also noted that changing the chain length of the capping ligand had no measureable effect on the rate of ET. They attributed the decrease in observed reaction rate to a mechanism in which CT proceeds through uncoordinated surface sites on the nanorod, so additional ligand would block access to these sites. Malicki, Knowles, and Weiss showed that exchanging oleate capping ligands for decanethiolate ligands can essential stop charge transfer between photo-excited lead sulfide (PbS) nanocrystals and

aminoferrocene.[11] The decanethiolate ligands keep the aminoferrocene from accessing the surface of the NC until the photo-excited state has decayed. In these two cases the ligands are modulating charge transfer between NC and small molecules in a steric sense, where they are physically blocking the small molecule from easily accessing the surface of the NC.

This mechanism of retarding the rate of CT, surface site access gated by ligand dissociation, would appear to be at play in the reaction of photoreduced ZnO with $^{t}Bu_3ArO^{\bullet}$, but other observations from our lab bring into question the ligand dissociation mechanism for the reaction discussed in this chapter. NMR studies of these dodecylamine capped ZnO NCs, at 0.1 mM concentrations, reveal that the NCs have a dynamic ligand shell with strongly bound, weakly bound, and free capping ligand.[12] Only about 15% of the surface zinc atoms, or 25% of a monolayer, have strongly bound dodecylamine. The ZnO NC concentrations used in the TA experiments described above are hundreds to thousands of times lower than those in the NMR studies, so the surface of the ZnO NCs should have even less strongly bound DDA. It should be quite easy for the $^{t}Bu_3ArO^{\bullet}$ to access the surface of the ZnO NC.

The charge carries in the CT reactions described above are all distinct so direct analogy with the ZnO NCs does not hold. In the case of the WOx nanorods, there are between 75 and 100 electrons in the "conduction band" of each nanorod, so the electrons may be quite localized on certain tungsten atoms.[10] In the reactions of photoreduced ZnO NCs with $^{t}Bu_3ArO^{\bullet}$, the NCs are in the limit of less than one electron per NC and the electron is delocalized over the entire volume of the NC.[13] The studies with the PbS nanocrystals observed hole transfer to aminoferrocene from an excited state,[11] the charge carrier is not stable over a period of days, as in the case of the ZnO NCs.[14] While the examples discussed above are simple CT, moving a single electron, the reaction studied in this chapter is PCET where a proton is also moved. The NMR studies of dodecylamine capped ZnO NCs showed evidence that the weakly bound ligands were hydrogen bonding with surface hydroxide groups. Since the ZnO NCs already have less than a monolayer of ligand coverage and should not sterically block $^{t}Bu_3ArO^{\bullet}$ from accessing the NC surface, the amine capping ligands may slow the reaction by hydrogen bonding with the surface protons required for PCET. The dodecylamine is acting like a base, modulating the concentration of protons, more than it is gating CT from NC surface access.

Given previous examples NC size influencing the rate of CT with small molecules; it was a surprise that a rather flat trend was observed when comparing the rate of PCET with ZnO

NC size. The work by Haase, Weller, and Henglein demonstrated that the rate constant for the reaction of photoreduced 1.7 nm diameter ZnO NCs with O_2 was 3.2×10^6 $M^{-1}s^{-1}$ while the rate constant for the reaction O_2 and 4.0 nm diameter NCs was 50 times slower.[6] In the case of PCET from photoreduced ZnO NCs to $^tBu_3ArO^{\bullet}$, the rate constant measured for 3.7 nm diameter NCs was $2.67 \pm 0.23 \times 10^6$ $M^{-1}s^{-1}$ and the rate constant measure with 6.0 nm diameter NCs was only 1.5 times slower. If the rate determining step of the reaction was ET or CPET, from the Marcus cross relation one would expect a 30 fold difference in rate constant from the 0.180 eV difference in E_{CB} for 3.8 and 6.0 nm diameter ZnO NCs.[15] As the observed rate constants only differ by a factor of 1.5, the data suggest that the rate determining step of the reaction is insensitive to the NC reduction potential, and therefore unlikely to be ET. It could be the case that tBu3ArO• binds to the surface of the photoreduced ZnO NC and ET does not occur until a reactive surface proton is encountered.

The results outlined in this chapter provide an interesting comparison to those in the next chapter, from the reaction of photoreduced ZnO NCs with 2,2,6,6-tetramethyl-piperidin-1-yl-oxyl (TEMPO). The experimental conditions were quite different for the two studies of PCET from photoreduced NCs to hydrogen atom acceptors. In this chapter the ZnO NCs were at a considerably lower concentration (0.1 to 1 μM) than in next (~100 mM), so the capping density of the NCs in this chapter would be lower as well. In all of the experiments with $^tBu_3ArO^{\bullet}$, the NC photoreduction was achieved with a laser flash at 355 nm, kinetic data was obtained from monitoring the band edge bleach over hundreds of microseconds, and the rate constants could be obtained with simple second-order kinetics. In the next chapter where reactions with TEMPO are described, the ZnO NCs were photoreduced with a Hg/Xe arc lamp and reactions performed at least a half hour after photoreduction. The kinetic data was obtained by monitoring the loss of the visible absorption in the millisecond to second range, and the kinetics were multi-exponential in nature, only allowing for the rough estimation of reaction lifetimes. The difference in the thermodynamics of $^tBu_3ArO^{\bullet}$ and TEMPO does explain the difference in the overall reaction rates, as the O–H bond in the $^tBu_3ArOH$ product is about 11 kcal/mol stronger than that of TEMPOH.[16] Given all the differences between the two studies, they both point to the protons playing a critical role in the rate of PCET; the experiments in the next chapter provide stronger evidence.

3.4 EXPERIMENTAL

3.4.1 *General Considerations*

The synthesis and characterization of ZnO NCs is described in Chapter 1. Solutions of ZnO NCs were stored in a freezer at -35 °C in a N_2 filled glovebox. Unless otherwise noted, all reagents were purchased from Aldrich and all solvents were purchased from Fisher Scientific. Ethanol was purchased from Decon. All samples for kinetic analysis were prepared in an N_2 filled glovebox and sealed in gas-tight Kontes quartz, fluorescence cuvettes to obtain measurements. Electronic absorption spectra were collected with a Hewlett-Packard 8453 diode-array UV-visible spectrophotometer.

3.4.2 *Synthesis of 2,4,6-tri-tert-butylphenoxyl radical*

2,4,6-tri-*tert*-butylphenol (^{t}Bu$_3$ArOH) was recrystallized from hot ethanol and the crystals were washed with ethanol cooled in dry ice to remove yellow colored impurities. ^{t}Bu$_3$ArO$^\bullet$ was prepared from the recrystallized ^{t}Bu$_3$ArOH with potassium ferricyanide in a biphasic anaerobic mixture of benzene and aqueous 1 M sodium hydroxide. In a slight modification to procedure,[17] the aqueous layer and a small portion of organic layer were removed with a cannula and the remaining benzene was removed under reduced pressure. The dry powder was transferred to an N_2 filled glovebox, dissolved in acetonitrile, and placed in a dark freezer at -35 °C where crystals were grown.

3.4.3 *Transient Absorption Experiments*

Transient Absorption experiments were performed on a commercially available Luzchem LFP-211 nanosecond laser flash photolysis apparatus. Solutions of reagents were photolyzed with the third harmonic (355 nm) of a Continuum Minilite I Nd:YAG laser. Shots were acquired with a 1 Hz repetition rate at about 7 mJ per pulse with a 5 ns pulse duration. Kinetic traces were obtained at 350 nm by probing with a Xenon light source perpendicular to the laser excitation. The probe beam was passed through a monochromator and collected on a PMT with the voltage controlled by software. Control experiments using only ZnO show bleaching of the band edge

faster than the resolution of the experiment followed by a persistent baseline offset, indicative of particle reduction. In a series of control experiments $^{t}Bu_3ArO^{\bullet}$ was shown to be stable at the 355 nm excitation wavelength and energy.

Experiments were performed on several batches of ZnO NCs with different average particle diameters and with varying concentrations of the dodecylamine capping ligand. To estimate the error in observed rate constant samples were prepared for Transient Absorption studies as follows. A dilute stock of ZnO NCs was prepared by diluting 270 µL of as synthesized ZnO to 8 mL with toluene using a 1000 µL pipettor. A solution of $^{t}Bu_3ArO^{\bullet}$ (19 mg, 72 µmol) was prepared with toluene in a 10 mL volumetric flask. Reaction mixtures were prepared from 200 µL of the dilute ZnO stock, 150 µL, 200 µL, 325 µL, and 400 µL of the $^{t}Bu_3ArO^{\bullet}$ stock and were all brought to a final volume of 4 mL with toluene. UV-Visible spectra of each sample was obtained before and after TA data was collected to measure the concentration range of $^{t}Bu_3ArO^{\bullet}$. TA data for each sample was obtained by averaging 50 measurements collected for a total of 400 or 800 µs with 2500 point resolution. This process was repeated three times for each of the four $^{t}Bu_3ArO^{\bullet}$ concentrations in order to obtain an experimental error for the observed rates.

Experiments exploring the effect of the dodecylamine capping ligands were performed by preparing reaction mixtures of dilute ZnO stocks and $^{t}Bu_3ArO^{\bullet}$, splitting them into equal portions and adding spikes of a dodecylamine solution and bringing the total volume of the reaction mixture to 4 mL with toluene in fluorescence cuvettes. An experiment looking at the effect of four different concentrations of the capping ligand was set up as follows. A dilute stock of ZnO NCs was prepared by diluting 200 µL of as synthesized ZnO to 8 mL with toluene. A solution of $^{t}Bu_3ArO^{\bullet}$ (19.5 mg, 74 µmol) was prepared with toluene in a 10 mL volumetric flask. A dodecyl amine (150 mg, 806 µmol) stock solution was prepared with toluene in a 5 mL volumetric flask. Reaction solutions with four different concentrations of $^{t}Bu_3ArO^{\bullet}$ were prepared with toluene in 10 mL volumetric flasks, using 870 µL of the dilute ZnO NC stock and 436 µL, 717 µL, 1000 µL, and 1,310 µL of the $^{t}Bu_3ArO^{\bullet}$ stock respectively. From these reaction solutions, 2.3 mL were transferred to fluorescence cuvettes and 0 µL, 100 µL, 200 µL, or 400 µL of the DDA stock were added to them before being brought to 4 mL with toluene. Details from other experiments are compiled in Table 3.2. The dodecylamine capping ligand concentration of the as synthesized ZnO NCs was calculated by estimating their surface area as a sphere and multiplying it by the experimentally determined capping density, 6.7 molecules per nm^2.[7]

The transient absorption traces had the first 252 to 256 data points removed to eliminate the time points before the laser flash and those that would include laser scatter. The data was then imported into SpecFit software and observed rate constants were obtained by fitting the data to a single exponential function. These observed rates were plotted against the concentration of $^{t}Bu_3ArO^{\bullet}$ with the slope of the fit being the second order rate constant for the reaction.

Table 3.5. Reaction Solution Details

NC Batch	ZnO NC Diameter (nm)	[ZnO] Stock (μM)	[ZnO] Reaction (μM)	[$^{t}Bu_3ArO^{\bullet}$] Stock (mM)	[$^{t}Bu_3ArO^{\bullet}$] Reaction (μM)	[DDA] Stock (mM)	[DDA] Added (mM)
MB2164	4.7	8.20	0.41	7.24	272, 362, 588, 724	N/A	N/A
MB2164	4.7	6.10	0.30	6.63	166, 290, 414, 540	161	7.3
MB2164	4.7	6.10	0.30	7.4	186, 306, 427, 555	161	4.0, 8.1, 16.1
MB3003	6.1	3.60	0.18	8.0	200, 330, 460, 600	N/A	N/A
MB3005	4.2	15.5	0.43	7.85	200, 326, 462, 598	165	4.1
MB3005	4.2	15.5	0.43	7.85	200, 326, 462, 598	165	4.1
MB3026	3.7	15.6	1.56	7.62	257, 327, 465, 526	162	4.0

3.5 NOTES

(1) Hagfeldt, A.; Graetzel, M. *Chem. Rev.* **1995**, *95* (1), 49–68.

(2) Anderson, N. A.; Lian, T. *Annu. Rev. Phys. Chem.* **2005**, *56* (1), 491–519.

(3) Stockwell, D.; Yang, Y.; Huang, J.; Anfuso, C.; Huang, Z.; Lian, T. *J. Phys. Chem. C* **2010**, *114* (14), 6560–6566.

(4) Ardo, S.; Meyer, G. J. *Chem. Soc. Rev.* **2008**, *38* (1), 115–164.

(5) Huss, A. S.; Bierbaum, A.; Chitta, R.; Ceckanowicz, D. J.; Mann, K. R.; Gladfelter, W. L.; Blank, D. A. *J. Am. Chem. Soc.* **2010**, *132* (40), 13963–13965.

(6) Haase, M.; Weller, H.; Henglein, A. *J. Phys. Chem.* **1988**, *92* (2), 482–487.

(7) Norberg, N. S.; Gamelin, D. R. *J. Phys. Chem. B* **2005**, *109* (44), 20810–20816.

(8) Meulenkamp, E. A. *J. Phys. Chem. B* **1998**, *102* (29), 5566–5572.

(9) Schrauben, J. N.; Hayoun, R.; Valdez, C. N.; Braten, M.; Fridley, L.; Mayer, J. M. *Science* **2012**, *336* (6086), 1298–1301.

(10) Grauer, D. C.; Alivisatos, A. P. *Langmuir* **2014**, *30* (9), 2325–2328.

(11) Malicki, M.; E. Knowles, K.; A. Weiss, E. *Chem. Commun.* **2013**, *49* (39), 4400–4402.

(12) Valdez, C. N.; Schimpf, A. M.; Gamelin, D. R.; Mayer, J. M. *ACS Nano* **2014**, *8* (9), 9463–9470.

(13) Whitaker, K. M.; Ochsenbein, S. T.; Polinger, V. Z.; Gamelin, D. R. *J. Phys. Chem. C* **2008**, *112* (37), 14331–14335.

(14) Liu, W. K.; Whitaker, K. M.; Kittilstved, K. R.; Gamelin, D. R. *J. Am. Chem. Soc.* **2006**, *128* (12), 3910–3911.

(15) Mayer, J. M. *J. Phys. Chem. Lett.* **2011**, *2* (12), 1481–1489.

(16) Warren, J. J.; Tronic, T. A.; Mayer, J. M. *Chem. Rev.* **2010**, *110* (12), 6961–7001.

(17) Manner, V. W.; Markle, T. F.; Freudenthal, J. H.; Roth, J. P.; Mayer, J. M. *Chem Commun* **2008**, No. 2, 256–258.

Chapter 4. REACTION DYNAMICS OF PROTON COUPLED ELECTRON TRANSFER FROM REDUCED ZNO NANOCRYSTALS[1]

4.1 INTRODUCTION

Many of the critical energy conversion reactions being studied at semiconductor interfaces, such as the oxidations of water and H_2, and the reductions of protons and CO_2, are inherently proton-coupled electron transfer (PCET) processes. These reactions are typically described as charge transfer (CT) processes, and their dynamics and mechanisms are usually discussed primarily in terms of the electronic energies of the charge carriers.[2–6] Other factors have been identified, including the nature and density of the surface ligands[7,8] and the crystal plane exposed to the solution.[9] However, there has been little study of the role of the protons in the kinetics of these reactions, outside of the typical Nernstian dependence of the band energies on proton activity (pH).[10,11]

Previous work from our laboratory has demonstrated that photo-reduced colloidal zinc oxide (ZnO) and titanium dioxide (TiO_2) nanocrystals (NCs) can react by proton-coupled electron transfer (PCET) with organic hydrogen atom acceptors.[12] The presence of chemically active protons is indicated by a number of observations, including the formation of protonated reaction products in aprotic media. Thermodynamic coupling of the protons and electrons in ZnO NCs was observed through electron transfer from one-electron reductants to the NCs upon addition of protons to suspensions of ZnO nanocrystals in aprotic solvents.[13]

This report is focused on the kinetics of the PCET reaction of photoreduced ZnO NCs with the nitroxyl radical TEMPO, which forms the hydroxylamine TEMPOH (2,2,6,6-tetramethyl-piperidin-1-yl-oxyl to N-hydroxy-2,2,6,6-tetramethylpiperidine), Equation 1. To write a balanced chemical equation, we write the photoreduced ZnO NCs as $ZnO{:}e^-_{CB}/H^+$. The subscript CB indicates that the electrons in these ZnO NCs occupy conduction band (CB)-like orbitals that are delocalized over the entire NC.[14] The presence of CB electrons is indicated by the blue color of the NC suspension, so in Equation 1 the circle representing the reduced NCs is colored blue.

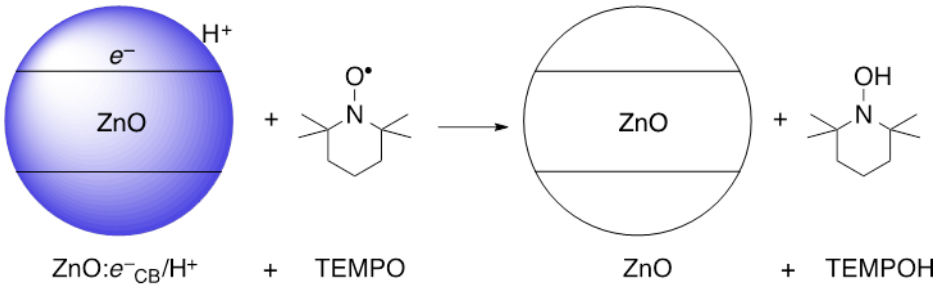

(1)

Most CT studies of NCs have examined photochemical or photo-initiated processes limited to short-lived photoexcited states; for some exceptions, see the following references.[10,11,15–17] This work uses stopped-flow spectroscopy to study the PCET reactivity of stable reduced NC suspensions. These reactions are slow, occurring on a milliseconds-to-seconds timescale, and are relevant to PCET catalysis at oxide interfaces. These TEMPO reactions are slower than the more typically studied photo-induced ET processes in part because of their lower driving force. PCET reactions that are more exoergic can proceed much more quickly, such as the reaction of photogenerated ZnO:e^-_{CB}/H^+ with the 2,4,6-tri-*tert*-butylphenoxyl radical (^{t}Bu$_3$ArO$^\bullet$), which has a 0.5 eV larger driving force and occurs with k ~ 10^7 M^{-1} s^{-1}.[11] This example suggests that the involvement of proton transfer does not necessarily make the reactions slow. The slow-timescale and proton-coupled nature of these reactions make them interesting models for steps occurring in fuel cell or solar fuel production, as these processes also occur on relatively slow timescales.[18]

Reproducible kinetic data for e^-/H^+ transfer from reduced ZnO to TEMPO have been obtained, by comparing aliquots from the same suspension of NCs. The disappearance of the CB electrons is multi-exponential but the kinetics are simple first-order in [TEMPO]. Using aliquots from a single batch of NCs, we have prepared sets of reduced ZnO suspensions that are compositionally essentially identical via slightly different chemical routes. Despite having essentially the same average numbers of electrons, protons and capping ligands, and the same electronic spectra, these samples show different kinetic behavior with TEMPO. We tentatively suggest that the history of the NC solution may yield different populations of protons that play a role beyond modulating the energetics, and we suggest that the protons need to be explicitly considered when X–H bonds are being formed or cleaved.

4.2 RESULTS

4.2.1 *Description of Kinetic Behavior.*

Mixing reduced ZnO NC colloids with anaerobic solutions of TEMPO causes rapid loss of the broad low-energy absorbance of the ZnO:e^-CB/H^+ (Figure 4.1a). Since TEMPOH is the product, this reaction involves the transfer of one e^-_{CB} and one H^+ to the substrate.[12] Reactions were typically carried out under conditions of excess TEMPO, with the e^-_{CB} as the limiting reagent, and were monitored via the absorbance at 700 nm, which scales linearly with the concentration of e^-_{CB}.[12,13] The decay in the TEMPO absorbance (λ_{max} 460 nm) is consistent with the changes at 700 nm. Control experiments reacting uncharged ZnO NCs with TEMPO did not show any reaction, as would have been evident from a decrease in the TEMPO optical absorbance. The colloidal ZnO:e^-_{CB}/H^+ are similarly stable for extended periods.

In the first set of experiments, reactions were monitored for one sample of reduced ZnO NCs with three different concentrations of TEMPO (Figure 4.1b). As described in the Experimental Section, all of the experiments reported here used this kind of comparison, starting from a single batch of NCs, to ensure that their properties were identical for all of the kinetic runs within a comparative set. In all of the kinetic runs, the absorbance at 700 nm at the first time point (1 ms) was significantly below the true initial value, calculated by halving the averaged absorbance of the reduced NC solution alone in the observation cell (without TEMPO). The absorbance values were obtained before and after reactions with TEMPO had been monitored by flushing through 0.5 to 1.0 mL of the reduced NC solution. In Figure 4.1b and some of the other Figures below, this initial absorbance is shown as a horizontal dashed line.

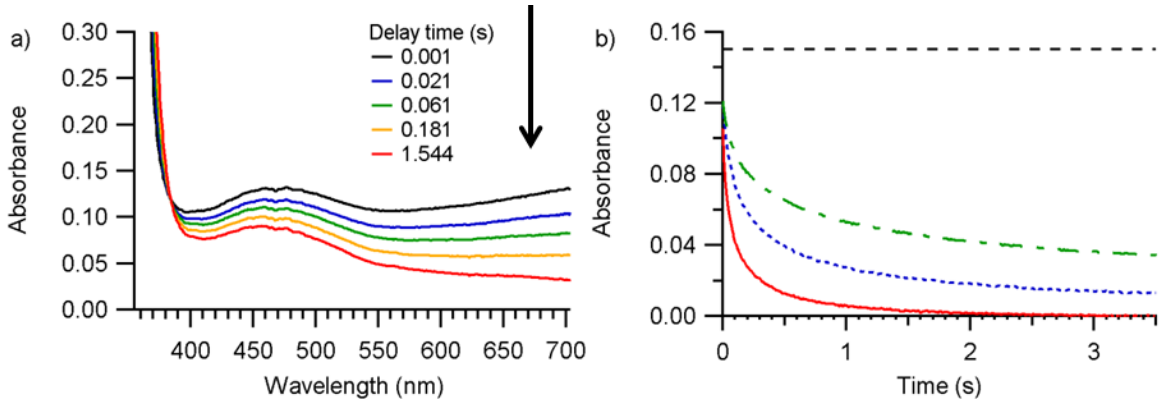

Figure 4.1. Absorption spectra and extracted single wavelength data showing the reaction of reduced ZnO NCs (0.17 mM, [e^-] = 0.24 mM) with TEMPO. (a) Stacked spectra from 1 ms to 1.54 s from reaction of reduced NCs with 4.8 mM TEMPO, black arrow indicating direction of absorbance change with time. The broad peak at 460 nm is due to TEMPO. (b) Absorbance at 700 nm plotted over 3.5 s for [TEMPO] = 0.24 mM (green, dot-dashed), 1.2 mM (blue, dotted), and 4.8 mM (red, solid). The black dashed line represents the initial absorbance if no reaction had occurred, determined from half of the absorbance of a spectrum of reduced, unreacted NCs pushed into the mixing chamber of the stopped-flow.

With each concentration of TEMPO, the decay in absorbance at 700 nm [A(700)] was multi-exponential. For instance, in a reaction with [e^-] = 0.24 mM and [TEMPO] = 1.2 mM (blue [middle] trace in Figure 1b), 20% of the reaction is complete within the 1 ms mixing time of the instrument. It took 100 ms for the reaction to reach 50% completion, and required 2 seconds to reach 75% completion. The decays can be fit to a stretched exponential function or (poorly) to a sum of two exponential functions, as described in the Appendix. In the bi-exponential fits, the time constants differ by roughly an order of magnitude.

4.2.2 *First-order Dependence on TEMPO Concentration.*

Higher concentrations of TEMPO increase the reaction velocity, as is qualitatively evident from the time traces in Figures 1b and 2a. In Figure 2, TEMPO is in 10 and 20 fold excess relative to electrons. The dependence of these reactions on the TEMPO concentration is indicated by plotting A(700) versus the product of time and [TEMPO], Figure 2b. This scaling of the time axis causes the two traces to overlay very closely over the entire reaction. This close overlay has

been observed in repeated experiments of this kind. The overlay of the kinetic traces vs. {time × [TEMPO]} shows that the reaction is first order in [TEMPO].[19] This scaling can be viewed as a graphical definition of first-order behavior.[20]

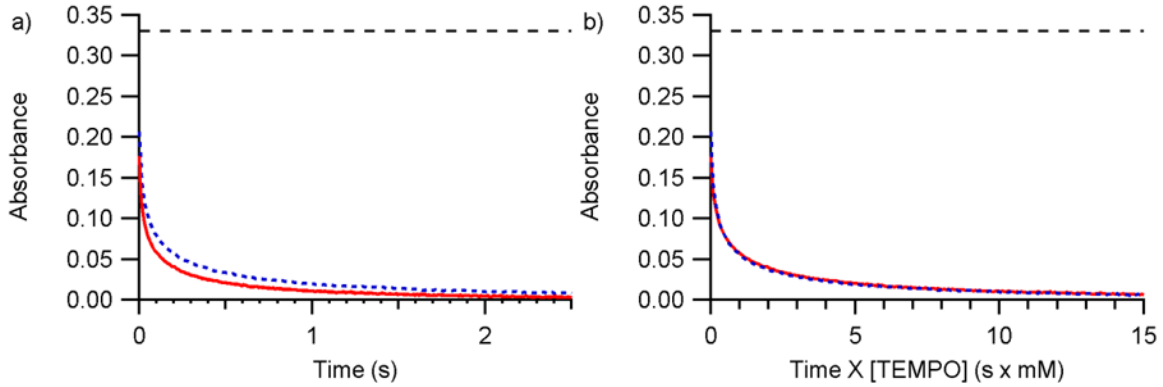

Figure 4.2. Reaction of reduced ZnO ([NC] = 0.17 mM; [e^-] = 0.47 mM) and TEMPO (blue line = 4.8 mM; red line = 9.6 mM). (a) Absorbance at 700 nm plotted for reactions with two concentrations of TEMPO; the red trace with the higher concentration of substrate decays faster. (b) The data on the left plotted with the time axis multiplied by the [TEMPO]; the traces overlay indicating a first order dependence on [TEMPO]. Dashed lines indicate the expected initial absorbance if no reaction occurred, obtained from half of the absorbance of a spectrum of reduced, unreacted NCs in the stopped-flow.

4.2.3 *Dependence on the Number of Electrons per NC.*

The effect of the extent of NC reduction on PCET reaction dynamics was studied by changing the electron content of different aliquots of a NC suspension. This was first done by diluting photolyzed aliquots with unphotolyzed aliquots of NCs in the glove box, Scheme 1a (see Experimental Section). Since charge transfer between NCs is very fast,[21] these samples rapidly equilibrated to different electron concentrations. There was minor air oxidation during sample loading onto the stopped-flow instrument, so the absorbance at 700 nm was used to measure the e^- concentration for each sample. Dividing the e^- concentration by the NC concentration gives the average e^-_{CB}/NC for each solution, being 2.7, 0.9, and 0.4 in this experiment. For each sample, the reaction with 4.8 mM TEMPO displayed multi-exponential A(700) vs. time traces, qualitatively similar to those as described above (Figure 4.3a).

The traces can be directly compared by normalizing the data, $(A_t-A_{final})/(A_{initial}-A_{final})$ (Figure 4.3b; semi-log plots are given in the SI), where $A_{initial}$ is the independently measured expected absorbance at t = 0 (see above). A_{final} is obtained from averaging the final 25 time points in reactions monitored to 15 seconds. It is qualitatively clear that the more highly reduced NCs react more quickly. For instance, the times for 50 percent of the electrons to react are 15, 75, and 160 ms for the 2.7, 0.9, and 0.4 e^-_{CB}/NC samples, respectively. Determining a quantitative relationship between the e^-_{CB}/NC and the kinetics has not been possible, due to the complexity of the multi-exponential kinetics. The origin of the multi-exponential behavior is discussed below.

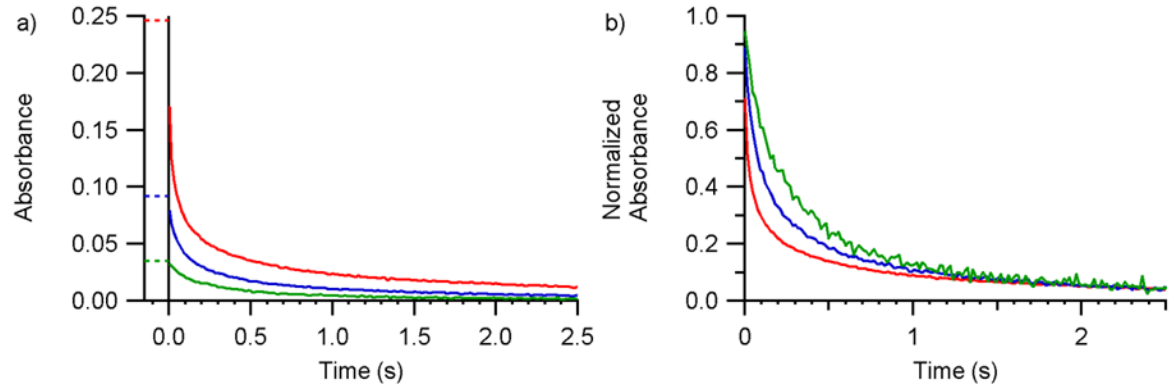

Figure 4.3. Plots for reaction of reduced ZnO NC solutions with TEMPO. [NC] = 0.13 mM; [e^-] = 0.35 (red, top); 0.13 (blue, middle); 0.049 mM (green, bottom); [TEMPO] = 4.8 mM. (a) Absorbance at 700 nm over the first 2.5 s of the reaction. (b) Normalized absorbance, $(A_t-A_{final})/(A_{initial}-A_{final})$ vs. time. The dashed lines before zero indicate the expected initial absorbance for each NC aliquot if no reaction occurred, obtained from half of the absorbance of a spectrum of reduced, unreacted NCs in the stopped-flow.

4.2.4 *Dependence on Pathway to NC Electron Content.*

In the experiment described in Scheme 1b, a NC suspension was split into aliquots and reduced by three different methods. The first sample was photolyzed for 80 minutes, yielding NCs reduced on average by 2.6 e^-_{CB}/NC once loaded into the stopped flow. The second sample, photolyzed for 20 minutes, provided a solution with 1.1 e^-_{CB}/NC. The third sample was prepared by mixing equal volumes of 80-minute photolyzed aliquot and unphotolyzed aliquots, produced NCs containing 1.0 e^-_{CB}/NC. Thus samples 2 and 3 had close to the same number of e^-_{CB}/NC but were prepared by different paths. The three samples were each reacted with the same 4.8 mM

TEMPO solution. Plots of absorbance and normalized absorbance $(A_t-A_{final})/(A_{initial}-A_{final})$ vs. time are shown in Figure 4.4. The normalized absorbance plot shows that the more reduced NCs react faster than the less reduced NCs, as observed previously. For the NCs prepared by short photolysis and by dilution, both the absorbance and normalized absorbance traces nearly overlay. Thus the two samples of NCs with similar ~1 e^-_{CB}/NC, formed by different procedures, have similar reaction dynamics with TEMPO.

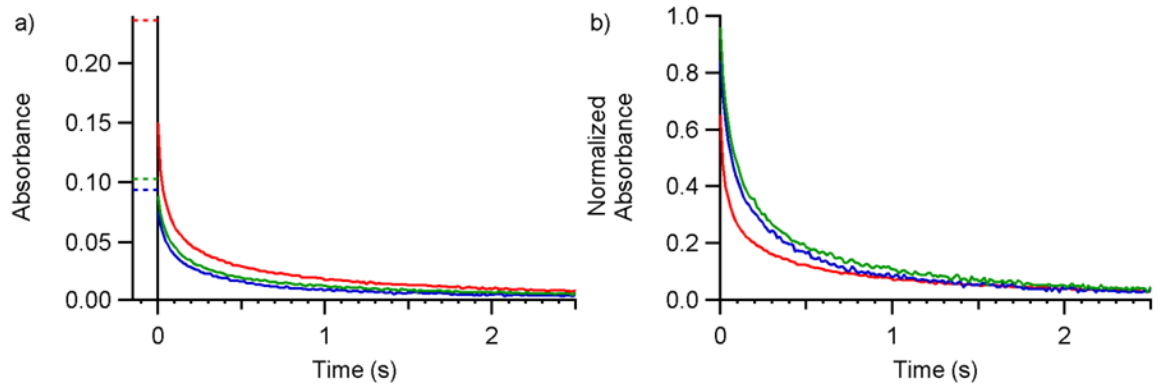

Figure 4.4. Kinetic plots for reactions of TEMPO with ZnO NCs ([NC] = 0.13 mM) reduced through different methods: 80 minute photolysis (red), [e^-] = 0.34 mM; 80 minute photolysis diluted with uncharged NCs (blue), [e^-] = 0.13; 20 minute photolysis (green) [e^-] = 0.15 mM with TEMPO (4.8 mM). (a) Absorbance at 700 nm vs. time. (b) Normalized absorbance, $(A_t-A_{final})/(A_{initial}-A_{final})$, vs. t. The dashed lines before zero indicate the expected initial absorbance for each NC aliquot if no reaction occurred, obtained from half of the absorbance of a spectrum of reduced, unreacted NCs in the stopped-flow.

To extend the previous analysis of NC reactivity dependence on the path to reduction, the experiments described in Scheme 1c were performed. An 80-minute photolyzed sample had 2.3 e^-_{CB}/NC once loaded onto the stopped-flow instrument. An aliquot of this sample diluted with the unphotolyzed solution yielded NCs with 0.8 e^-_{CB}/NC. The last portion was titrated in the glovebox with a sub-stoichiometric amount of TEMPO to produce a solution with 1.0 e^-_{CB}/NC on average. All of the solutions were reacted with the same concentration of TEMPO in greater than 10 fold excess. The resulting plot of absorbance at 700 nm vs. time appears similar to those shown above (Figure 4.5a). The normalized and semi-log kinetic traces (Figures 4.5b and 4.5c) show that the most reduced aliquot reacts fastest, as expected. For the two less reduced samples,

the TEMPO-quenched sample initially reacts slightly faster, as expected because it has a slightly higher [e^-]. In the second half of the reaction, however, the traces for these two samples diverge. The reaction velocity of the sample pre-reacted with TEMPO is lower than the diluted sample, even though it had a slightly higher initial electron concentration. These two samples have different reactivity, even though they have essentially the same concentration of electrons. They have just had a different path to get to that [e^-].

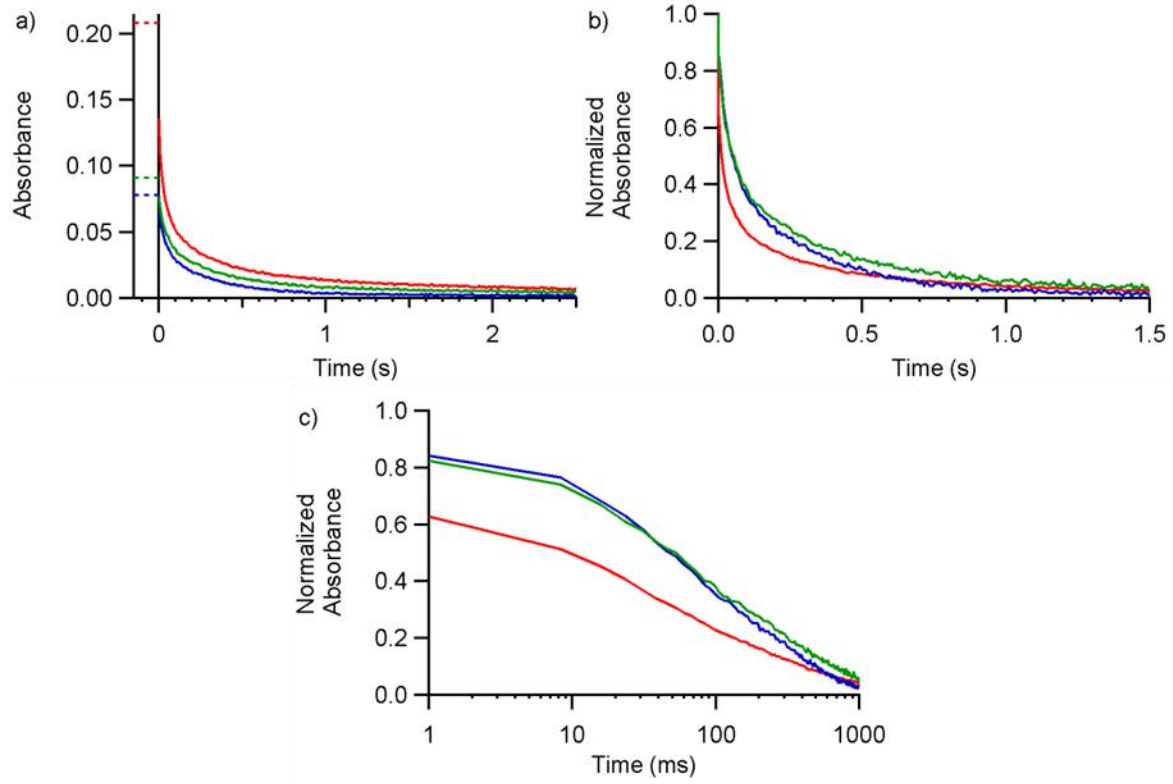

Figure 4.5. Kinetic plots for reactions of TEMPO (4.8 mM) with ZnO NCs ([NC] = 0.13 mM) reduced through different methods: 80 min photolysis (red), [e^-] = 0.30 mM; 80 min photolysis then diluted with unphotolyzed NCs (blue), [e^-] = 0.11 mM; 80 min photolysis then pre-reaction in the glove box with a small amount of TEMPO (green), [e^-] = 0.13 mM). (a)A(700) vs. t. (b) Normalized absorbance, $(A_t-A_{final})/(A_{initial}-A_{final})$, vs. t. The dashed lines before zero indicate the expected initial absorbance for each NC aliquot if no reaction occurred, obtained from half of the absorbance of a spectrum of reduced, unreacted NCs in the stopped flow. (c) Normalized absorbance data plotted on a semi-log scale.

There is another way to look at these data to further probe whether the pathway to a certain concentration of electrons is important. Consider the reactions of the most highly charged NCs, those that had been irradiated for 80 minutes and have ca. 2.5 e^-_{CB}/NC. When these react with TEMPO in the stopped flow instrument, after about 30 to 52 ms they reach ~1 e^-_{CB}/NC. This is the same concentration as the less photolyzed, diluted or pre-oxidized samples. However, this ~1 e^-_{CB}/NC sample has a quite different kinetic behavior with the same amount of TEMPO. The best way to illustrate this is to adjust the time axis of the A(700) vs. time trace of the more highly reduced sample, so that it has the same absorbance as the less-reduced sample at "t = 0". Conceptually, this is like treating the first 30 to 52 ms of reaction as a "pre-reaction" to prepare a sample with ~1 e^-_{CB}/NC. Figure 4.6a shows this 'time axis-shifted' plot for the data in Figure 4.4 above. Upon shifting the time axis of the 80 minute photolysis NC sample to the initial absorbance of the 20 minute photolysis NCs, it is observed that the absorption for the 20-minute photolyzed NCs decays more quickly than NCs that initially were more reduced. The 20-minute photolyzed sample is significantly more reactive than the 80-minute sample that has reached ~1 e^-_{CB}/NC in the stopped-flow. The same behavior is seen when the data from Figure 4.5 are time shifted (Figure 4.6b and 4.6c): the initially more reduced sample is less reactive once it reaches the lower charging level inside the stopped-flow.

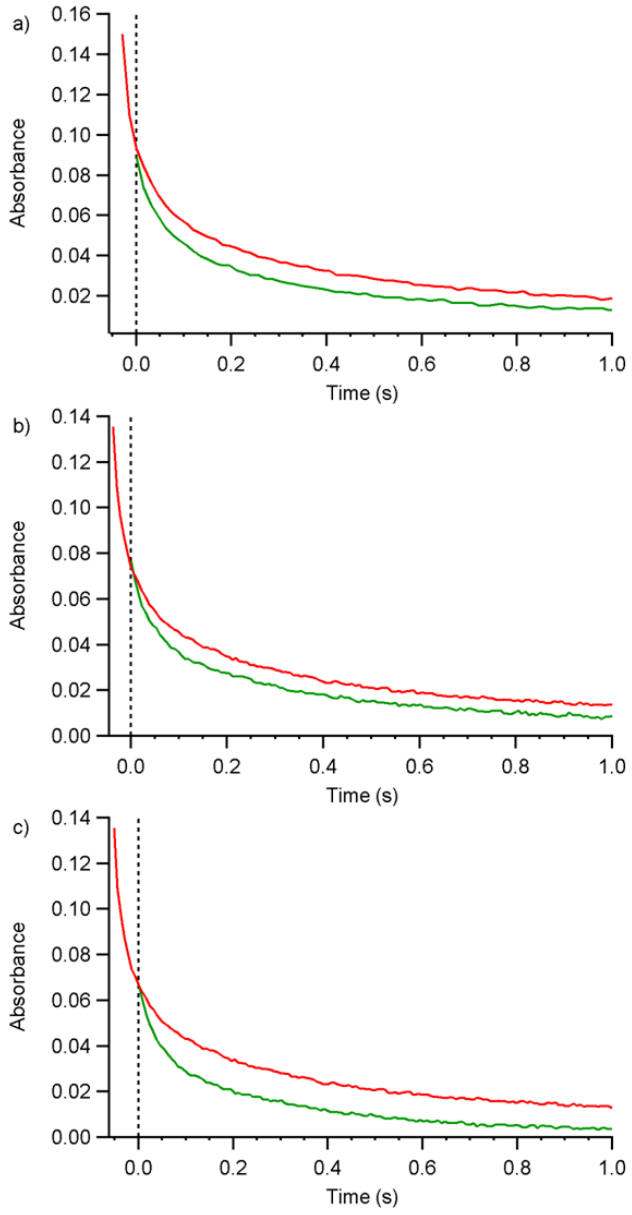

Figure 4.6. Kinetic plots for reactions of TEMPO with ZnO NCs in which the time axis for the red data has been shifted to the left so that at it has the same absorbance as the other sample at t = "0" (indicated by the vertical dotted line). (a) Data from Figure 4, with the 80 minute-photolyzed sample (initially 2.6 e^-_{CB}/NC, red) shifted 30 ms to the left to overlap with the 20 minute-photolyzed data (initially 1.1 e^-_{CB}/NC, green). (b) Data from Figure 5, with the 80 minute-photolyzed sample (initially 2.3 e^-_{CB}/NC, red) shifted 45 ms to the left to overlap with the TEMPO-pre-reacted sample (initially e^-_{CB}/NC, green).). (c) Data from Figure 5, with the 80 minute-photolyzed sample (initially 2.3 e^-_{CB}/NC, red) shifted 52 ms to the left to overlap with the diluted sample (initially 0.8 e^-_{CB}/NC, green).

These various examples show that NC aliquots with the same concentration of electrons can have different reactivity if they are prepared by different paths. These comparisons are made on the same batch of photoreduced NCs, so the compared suspensions have the same concentration and the same distribution of sizes, shapes, capping groups, and protons. This is one of the most important conclusions of this study; the reactivity of otherwise identical NCs does not simply scale with the concentration of electrons. This conclusion contrasts with the implicit assumptions in Gerischer-type models typically used for semiconductor-solution charge transfer reactions.[22,23] These models emphasize the energy of the electrons or holes (typically the Fermi energy).

4.3 DISCUSSION

4.3.1 *Mechanistic Overview of Proton-Coupled Electron Transfer at Colloidal ZnO Nanocrystals*

The reaction of photoreduced ZnO (ZnO:e^-_{CB}/H^+) with the nitroxyl radical TEMPO (Equation 1) is a proton-coupled electron transfer process because both e^- and H^+ are transferred to form TEMPO-H. Reaction 1 has been studied by traditional stopped-flow mixing kinetics, appropriate for its timescale of milliseconds to seconds. The two reagents start in different solutions and undergo many collisions prior to reaction. (The collision frequency under these conditions is $>10^8$ s^{-1}, see Appendix) These reactions are therefore somewhat different than the more traditional studies of photoinitiated processes, which occur on much shorter timescale and often involve pre-coordinated substrates (*cf.*[24]).

The kinetics of reaction 1 being first order in [TEMPO] is similar to the first-order dependence of the reaction of ZnO:e^-_{CB}/H^+ with the phenoxyl radical $^tBu_3ArO^\bullet$ observed in our previous laser-flash photolysis studies (see Chapter 3 and reference 11). The precise details of how TEMPO approaches the surface and acquires the e^- and H^+ are not known. The density of DDA capping ligands on these NCs is relatively low (~25-50%)[25] so the surface is accessible to the TEMPO. To avoid the effects of changes in capping ligand density (as discussed in Chapter 3), all of the comparative experiments described here involved solutions with the same DDA/NC ratio. The reaction must occur at a particular site on the surface because a proton is a quite localized particle, able to tunnel only a few tenths of an Ångström.[26] Reaction 1 is very unlikely to occur by initial outer-sphere electron transfer because TEMPO has a very negative redox

potential even in polar media, and formation of the $TEMPO^-$ anion in the non-polar toluene is very unfavorable.[27] Similarly, TEMPO is not a strong base and the NC acidity is buffered by the excess DDA present, so initial proton transfer to form $TEMPOH^{+\bullet}$ is also very unfavorable. It could be that TEMPO abstracts e^- and H^+ from a NC in one kinetic step, which would resemble a hydrogen atom transfer process (also termed concerted proton-electron transfer, CPET).[28] Alternatively, TEMPO could potentially bind to the surface, concomitant with transfer of an electron to form a $TEMPO^-$ ligand to a Lewis-acidic zinc site, followed by protonation to form TEMPO-H. In either case, the proton must be at or very near the surface, likely present as a surface hydroxide or a surface-bound dodecylammonium ion ($C_{12}H_{25}NH_3^+$). Preliminary experiments with added strong base suggest the presence of at least dozens of surface protons in the non-reduced NC.[25] This is not surprising since the NCs are prepared hydrolytically and are not calcined. Photochemical charging adds a stoichiometric proton for each added electron.[12] The reduced NCs may have some protons intercalated into the ZnO, as there is strong evidence for intercalated e^- and H^+ in bulk ZnO.[29–32] Protons below the surface of a NC would have to diffuse to the surface to be reactive.

4.3.2 *Multi-Exponential Kinetics.*

The reaction of $ZnO{:}e^-_{CB}/H^+$ + TEMPO (eq 4.1) is not first order in the concentration of electrons. Reactions were monitored by the change in absorbance at 700 nm, which measures the decrease in the concentration of electrons, the limiting reagent in the experiments. The multi-exponential behavior is illustrated by the contrast between the substantial amount of reaction within the 1 ms mixing time of the stopped-flow instrument vs. the ca. 1 s needed for completion. In reactions of NC suspensions with $>2e^-$/NC on average, ~30% of the reaction is complete in the 1 ms mixing time while ca. 500 ms are needed to reach ~90% of reaction.

Some of the multi-exponential behavior could be due to the distribution of electrons within the ensembles of NCs, some having $1e^-$, some $2e^-$ *etc*. However, similar kinetics are observed even for samples with an average of 0.4 e^-/NC, in which the distribution is likely much narrower than in the $>2e^-$/NC samples. The added electrons have been shown to occupy conduction band states rather than trap states, even at 4K.[14] The reduced NCs are stable for extended periods and do not form H_2. Control experiments mixing TEMPO with non-reduced ZnO NCs, and mixing TEMPOH with reduced NCs, showed no reaction. Thus there are no

indications of side reactions, for instance with the DDA capping ligands. Addition of TEMPOH did not inhibit a reaction of ZnO:e^-_{CB}/H^+ + TEMPO, so there is no evidence for TEMPOH blocking reactive sites. Such blocking seems quite unlikely as the reactions only involve 0.4-3 TEMPO molecules per NC and there are hundreds of surface zinc ions and likely many dozens of surface protons.

Multi-exponential or "distributed" kinetic behavior is often observed for CT reactions between molecules and nanomaterials. The most studied class are charge injection and back electron transfer between semiconductors and surface-attached dyes. These are typically thought to be multi-exponential because of a variety of dye/semiconductor structures and interactions.[33,34] The behavior of the injected electrons in nanoscale TiO_2 electrodes has also been interpreted with continuous-time random walk models of electron hopping and trapping events.[35] The complex kinetics of ET from WO_x nanorods to a soluble Fe(III) oxidant was ascribed to the varying energetics of the multiple electrons being transferred.[8]

It is not evident why the ZnO:e^-_{CB}/H^+ + TEMPO reaction has multi-exponential kinetic behavior. However, there are a number of features of this reaction that constrain the possible explanations, starting with the slow rate of reaction and the simple first order dependence on [TEMPO]. Consider first a hypothetical ensemble of *identical* ZnO:e^-_{CB}/H^+ particles with multiple reactive sites on the surface, perhaps multiple proton sites. This would not give multi-exponential kinetic behavior. The reactions studied here are in the limit of many collisions per reactive event so that all surface sites will be explored. Identical ZnO:e^-_{CB}/H^+ particles with multiple reactive hydrogens on the surface would behave just like molecules in a solution, which might have, for instance, multiple reactive hydrogens. In propane ($CH_3CH_2CH_3$), for example, the primary and secondary hydrogen sites have different reactivities but that does not lead to multi-exponential kinetics.[36]

The multi-exponential kinetics therefore must result from some sort of heterogeneity of the NCs, a difference among the particles that is not rapidly equilibrating on the ms timescale. This heterogeneity could be in the sizes of the NCs, the energetics of the CB electrons, the faceting of the NCs, the number or position of the capping ligands, and the number and nature of the proton sites. We note that spectroscopic studies have shown that the added electrons in such ZnO NCs occupy orbitals that are delocalized over the entire NC.[14] So there is not the broad distribution of mid-gap electron trap states that are common in TiO_2 and other materials.

The uncharged ZnO NCs have a size distribution of about ±17% about the mean, estimated from the shape of the band edge absorption.[37] This distribution of sizes leads to a distribution of electron energies in the NCs. It is important to note that electron transfer between NCs is rapid under these conditions. ET from smaller NCs to larger ones occurs within 2 ms even at 50 μM NCs.[21] So as the reaction proceeds, the highest energy more reactive electrons should be depleted and this could be the cause of the multi-exponential kinetics. The results in Figure 3b support the qualitative prediction of this 'electron energy' model, as the decay of e^-_{CB} signal at 700 nm upon reaction with TEMPO is progressively slower in NCs with decreasing electron content. However, this model is not consistent with the conclusions of the previous section that the kinetic behavior is not just due to the number of electrons. The failure of this model can also been seen from the data in Figure 3, comparing the reactions of 2.7, 0.9, and 0.4 e^-_{CB}/NC samples. The last 15% of the reaction of the 2.7 e^-_{CB}/NC sample is dramatically slower than the initial reaction of the 0.4 e^-_{CB}/NC sample, even though they have the same electron concentration. Furthermore, electron transfer between PbS NCs and quinones with similar size distributions display single exponential kinetic behavior in the μs, collisional time-frame.[24]

So we conclude both that the NCs in the suspension must be inhomogeneous, to account for the multi-exponential kinetics, and that the electron concentration alone does not account for this heterogeneity. This is not a small effect, as rough fitting of the data to a bi-exponential model gives time constants for the fast and slow components that differ by an order of magnitude. It seems unlikely that this is due to variations in the size and shape of the NCs, given the fairly narrow size distribution (±17%).[37] Similarly, heterogeneity in the capping group number and density seem unlikely to cause this large a variation given the low number of strongly bound groups.[25]

One possible explanation is that the effects observed here are related to the protons transferred in this PCET process. Perhaps there are different populations of protons compensating the charge of the CB electrons and these have varying facility to transfer to TEMPO. The changes in the particles with time or different treatments could then relate to these proton populations. These NCs undoubtedly have surface protons in the form of surface hydroxyl groups, from their hydrolytic synthesis and from the photoreduction process.[12,25] There is also a body of experimental[38,39] and computational[40] evidence for protons intercalating into bulk ZnO. The diffusivity of deuterium in bulk ZnO and ZnO films is likely $\geq$10 nm^2s^{-1} [as extrapolated

from higher temperature measurements[41,42]] so movement of protons in these NCs on this timescale is reasonable. The experiments reported here may perhaps be plausibly interpreted as more reactive surface protons being removed from the NC first and other protons having to migrate to those more reactive sites. The differences in reactivity observed between the samples partially oxidized with TEMPO versus partially oxidized with uncharged NCs, could be due to these reagents removing protons from ZnO:e^-_{CB}/H^+ NCs in different ways.

The ZnO:e^-_{CB}/H^+ + TEMPO PCET reaction seems slow compared to related studies of electron transfer (ET) reactions of nanocrystals.[21] Bimolecular ET from photoreduced PbS NCs to benzoquinone, for instance, occurs on the microsecond timescale, $k_q = 4.7 \times 10^8$ $M^{-1}s^{-1}$.[24,43] Quantitative comparisons are difficult due to reaction 1 being multi-exponential and showing substantial reactivity within the ca. 1 ms mixing time of the stopped-flow instrument, but the timescales of the reactions indicate bimolecular rate constants from 10 - 10^4 M^{-1} s^{-1} (see Appendix). These are not atypical of molecular PCET reactions of TEMPO, which is fairly sterically crowded. More detailed interpretations of the reaction timescales will require as yet unavailable information about the free energies of the reactions. The slowness of the reactions described here do not appear to be simply due to their being PCET processes, as flash-kinetics experiments indicated rate constants of ca. 10^7 M^{-1} s^{-1} for the PCET reaction between the photoinduced reactions of ZnO NCs and $^tBu_3ArO^{\bullet}$.[12] $^tBu_3ArO^{\bullet}$ reactions are 0.46 eV more exoergic than analogous TEMPO reactions, based on their O–H bond dissociation free energies.[27]

4.4 CONCLUSIONS

Proton-coupled electron transfer (PCET) from photoreduced colloidal ZnO nanocrystals (ZnO:e^-_{CB}/H^+ NCs) to the nitroxyl radical TEMPO proceeds over the ms to s timescale. The kinetics are first order in TEMPO. More highly reduced NCs react faster. The rate of decay of the electron concentration is multi-exponential for all NCs, even those with less than $1e^-$/NC on average. The multi-exponential kinetic behavior is indicated to be due to the heterogeneity of the nanocrystals. We tentatively suggest that this heterogeneity is at least in part due to a distribution of the nature of the reactive protons. Reduced NCs from the same batch with the same average number of electrons per NC can have different kinetic behavior, depending on the different chemical routes to that electron concentration. For instance, two samples with the same average

number of electrons per NC can be prepared from aliquots of a highly reduced ZnO:e^-_{CB}/H^+ NC suspension by partial oxidation with TEMPO or with uncharged ZnO NCs. Thus the electronic composition and electron energy are not the sole determinant of reactivity. These results indicate limitations of the simple energy level diagrams which are commonly used to interpret interfacial redox reactivity. Future studies will probe whether these conclusions are general to PCET reactions of other oxides, to catalytic processes that involve PCET, and to reactions that involve just the transfer of an electron or hole.

4.5 EXPERIMENTAL

4.5.1 *General Considerations*

ZnO NCs were prepared as previously described,[44] from the addition of ethanolic tetramethylammonium hydroxide to zinc acetate in dimethyl sulfoxide/ethanol at 0 °C. The NCs were washed with ethanol twice and capped with dodecylamine before being suspended in toluene. These stock solutions of NCs were bubble degassed under reduced pressure and stored at -35 °C in an N_2-filled glovebox. The ZnO NC concentrations were calculated from the average NC size (4 to 4.2 nm in diameter), determined from optical spectra of dilute solutions,[45] together with the zinc concentration of those solutions, measured by ICP-AES. TEMPO (Sigma-Aldrich) was sublimed before use. Dodecylamine, 98% from Sigma-Aldrich, was used without further purification. Toluene was obtained from a Seca Solvent System installed by GlassContour.

Manipulations of solutions were completed in an air-free glove box, unless otherwise noted. In a typical experiment, a ZnO NC stock solution was removed from cold storage and allowed to reach room temperature, 24±1 °C. An experimental solution of 0.26-0.34 mM ZnO NC was prepared by dilution with toluene. Photoreduction of the experimental solutions was achieved by removing a portion of this solution from the glovebox in a quartz reaction vessel outfitted with a Kontes valve and a Teflon coated stir-bar, followed by photolysis for 20 to 80 minutes with stirring using an Oriel 200 W Hg/Xe arc lamp (Model 66056) and power supply (Model 68742, operating at 6 amps). After the desired photolysis time, the reduced NC solution was returned to the glovebox and split into aliquots which were further manipulated, *vide infra*. These aliquots were loaded into 5 or 10 mL gas-tight syringes with valves. Gas-tight syringes of degassed toluene and solutions of TEMPO were also prepared in the glovebox.

The NC aliquots, solvent and reagent-filled syringes were removed from the glovebox and attached to the sample handling unit of a TgK Double-Mixing Cryo Stopped-Flow Instrument. Hamilton "T" valves were attached between the sample and reservoir syringes to aid in removing air bubbles. The reservoir syringes and reagent lines were rinsed with 3 to 4 mL of degassed solvent before being replaced with syringes of reduced NC or TEMPO solutions. Spectra to determine the [e^-] were obtained by pushing 0.5 to 1.5 mL of the NC solution through the observation cell prior to and after reactions. The actual initial reaction concentrations were half of this measured value (to account for mixing with the TEMPO solution), and are indicated by dashed lines in many of the Figures below. Reactions were performed at 0 °C and monitored between 340 and 705 nm with the diode array detector. Data were collected from the mixing time of the instrument, *ca*. 1 ms, over time courses of 1.5 to 35 s depending on the conditions, using integration times of 1.5 to 2 ms.

PCET from reduced ZnO NCs to TEMPO was monitored through the loss of a broad absorbance in the visible spectrum of the reaction solution. This visible absorbance is the high energy tail of a very broad band peaking in the IR, and has been described as an intra-band absorption of the CB electrons.[46] While the shape and intensity of this overall resonance is a complex function of the concentration of electrons, we have shown by titration that for these sizes of NC_S, the absorbance at 700 nm is a linear function of the number of electrons, with an extinction coefficient $\varepsilon = 700 \pm 100\ M^{-1}\ cm^{-1}$.[13] This ε and the spectra mentioned above determined the electron concentration of the NC suspension. While there is some small variation in the ε from one experiment to another, in every case the absorbance at 700 nm depends linearly on the [e^-] based on titration experiments. Therefore the kinetics of the reactions were analyzed using the absorbance at 700 nm.

4.5.2 *Manipulation of Experimental NC Samples*

The electron content of the NC samples was modulated in three different ways; changing photolysis time, dilution with unreduced NCs, and oxidation with TEMPO (Scheme 1). This allowed us to observe how the path to a particular electron concentration effected the reaction of the NCs with TEMPO.

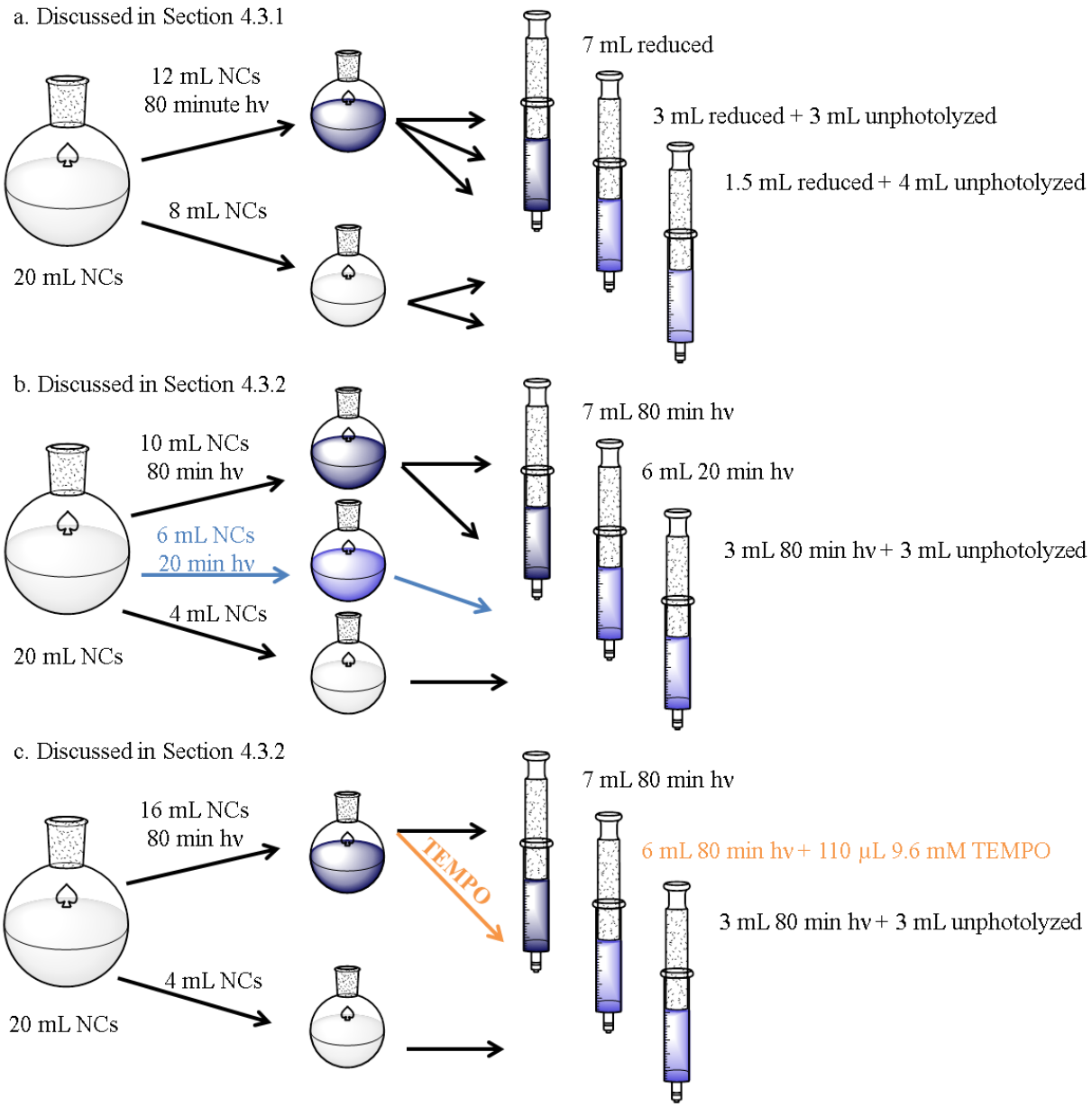

Scheme 4. Manipulation of NCs solutions to observe effects on reaction dynamics of photoreduced ZnO NCs and TEMPO. a) Dilution of photoreduced NCs with unphotolyzed NCs, Section 4.3.1. b) NCs with same electron content reached through short photolysis time or long photolysis time and dilution with unreduced NCs, Section 4.3.2. c) NCs with same electron content reached though oxidation with TEMPO or dilution with unreduced NCs, Section 4.3.2.

One set of experiments to probe the effect of electron concentration is illustrated in Scheme 4a (results in Figure 4.3 above). An experimental solution was prepared by diluting 15 mL of a stock solution to 20 mL ([NC] = 0.26 mM) with toluene. A 12 mL portion was

transferred to the gas-tight quartz vessel photolyzed for 80 minutes. Three aliquots were prepared for comparison on the stopped-flow spectrometer: 7 mL of the photolyzed experimental solution; 3 mL of the photolyzed solution mixed with an equal volume of the unphotolyzed solution; and 1.5 mL of the photolyzed solution mixed with 4 mL of the unphotolyzed solution. Previous work has shown that inter-NC ET is fast and should rapidly equilibrate the electrons across all the NCs in the colloidal suspension.[19] This kind of procedure was followed in all of the experiments reported here, to ensure that the NC properties were identical for all of the kinetic runs within a comparative set. This avoids the incidental variation in the properties of the NCs between synthetic batches, for instance in the concentration of dodecylamine capping groups. For instance, the dilution experiments mixed reduced NCs with unphotolyzed NCs from the same batch, thus maintaining a constant capping ligand/NC ratio.

In order to probe whether the pathway to NC electron content has an effect on the reaction with TEMPO the experiments in Scheme 4b were undertaken (results in Figure 4.4). An experimental solution was prepared by diluting 15 ml of a stock solution to 20 mL ([NC] = 0.26 mM) with toluene. This solution was separated into three aliquots of 10, 6, and 4 mL. The 10 and 6 mL aliquots were photolyzed for 80 and 20 minutes respectively and the 4 mL aliquot was left unphotolyzed. A 3 mL portion of the 80 minute photolyzed aliquot was mixed an equal volume of the unphotolyzed aliquot.

The experiments illustrated in Scheme 4c (Figure 4.5) used a 20 mL experimental solution, prepared as described above, separated into 16 and 4 mL aliquots. The 16 mL aliquot was photolyzed for 80 minutes. A 6 mL portion of the photolyzed solution was oxidized with a 110 µL volume of TEMPO [19.2 mM], monitoring this reaction with an Ocean Optics UV-Visible spectrometer in the glove box. A 3 mL portion of the photolyzed sample was diluted with an equal volume of the photolyzed aliquot. A 7 mL portion of the photolyzed aliquot was kept for comparison with the other two samples.

4.6 NOTES

(1) This chapter was prepared and accepted as an article in ACS Nano. I gratefully acknowledge Daniel Gamelin for critical intellectual contributions and proofreading and Jim Mayer for helping me shape the entire chapter, especially the introduction and discussion sections. Braten, M.N.; Gamelin, D. R.; Mayer, J. M. *ACSNano.* **2015**, *9* (10), 10258-10267.

(2) Walter, M. G.; Warren, E. L.; McKone, J. R.; Boettcher, S. W.; Mi, Q.; Santori, E. A.; Lewis, N. S. *Chem. Rev.* **2010**, *110* (11), 6446–6473.

(3) Nozik, A. J. *Annu. Rev. Phys. Chem.* **1978**, *29* (1), 189–222.

(4) *Materials and Processes for Solar Fuel Production*; Viswanathan, B., Subramanian, V., Lee, J. S., Eds.; Nanostructure Science and Technology; Springer New York: New York, NY, 2014; Vol. 174.

(5) Berger, T.; Monllor-Satoca, D.; Jankulovska, M.; Lana-Villarreal, T.; Gómez, R. *ChemPhysChem* **2012**, *13* (12), 2824–2875.

(6) Bard, A. J. *J. Am. Chem. Soc.* **2010**, *132* (22), 7559–7567.

(7) Knowles, K. E.; Frederick, M. T.; Tice, D. B.; Morris-Cohen, A. J.; Weiss, E. A. *J. Phys. Chem. Lett.* **2012**, *3* (1), 18–26.

(8) Grauer, D. C.; Alivisatos, A. P. *Langmuir* **2014**, *30* (9), 2325–2328.

(9) Liu, G.; Yu, J. C.; Lu, G. Q. (Max); Cheng, H.-M. *Chem. Commun.* **2011**, *47* (24), 6763–6783.

(10) Hamann, T. W.; Gstrein, F.; Brunschwig, B. S.; Lewis, N. S. *J. Am. Chem. Soc.* **2005**, *127* (21), 7815–7824.

(11) Lyon, L. A.; Hupp, J. T. *J. Phys. Chem. B* **1999**, *103* (22), 4623–4628.

(12) Schrauben, J. N.; Hayoun, R.; Valdez, C. N.; Braten, M.; Fridley, L.; Mayer, J. M. *Science* **2012**, *336* (6086), 1298–1301.

(13) Valdez, C. N.; Braten, M.; Soria, A.; Gamelin, D. R.; Mayer, J. M. *J. Am. Chem. Soc.* **2013**, *135* (23), 8492–8495.

(14) Whitaker, K. M.; Ochsenbein, S. T.; Polinger, V. Z.; Gamelin, D. R. *J. Phys. Chem. C* **2008**, *112* (37), 14331–14335.

(15) Haase, M.; Weller, H.; Henglein, A. *J. Phys. Chem.* **1988**, *92* (2), 482–487.

(16) Shim, M.; Guyot-Sionnest, P. *J. Am. Chem. Soc.* **2001**, *123* (47), 11651–11654.

(17) Mohamed, H. H.; Mendive, C. B.; Dillert, R.; Bahnemann, D. W. *J. Phys. Chem. A* **2011**, *115* (11), 2139–2147.

(18) Jiao, F.; Frei, H. *Energy Environ. Sci.* **2010**, *3* (8), 1018.

(19) Look, J. L.; Wick, D. D.; Mayer, J. M.; Goldberg, K. I. *Inorg. Chem.* **2009**, *48* (4), 1356–1369.

(20) A rate law that is first-order in [TEMPO] can be written as $d[e^-]/dt = f([e^-])[TEMPO]$, where the $f([e^-])$ term describes the non-exponential form of the kinetics and is independent of [TEMPO]. Rearranging to $d[e^-] = f([e^-])\{[TEMPO]dt\}$ shows that the reaction course should be invariant to the product of [TEMPO] times time under conditions of excess (constant) [TEMPO].

(21) Hayoun, R.; Whitaker, K. M.; Gamelin, D. R.; Mayer, J. M. *J. Am. Chem. Soc.* **2011**, *133* (12), 4228–4231.

(22) Koval, C. A.; Howard, J. N. *Chem. Rev.* **1992**, *92* (3), 411–433.

(23) *Electrochemistry at Semiconductor and Oxidized Metal Electrodes | S.R. Morrison | Springer*.

(24) Knowles, K. E.; Tagliazucchi, M.; Malicki, M.; Swenson, N. K.; Weiss, E. A. *J. Phys. Chem. C* **2013**, *117* (30), 15849–15857.

(25) Valdez, C. N.; Schimpf, A. M.; Gamelin, D. R.; Mayer, J. M. *ACS Nano* **2014**, *8* (9), 9463–9470.

(26) Krishtalik, L. I. *Biochim. Biophys. Acta BBA - Bioenerg.* **2000**, *1458* (1), 6–27.

(27) Warren, J. J.; Tronic, T. A.; Mayer, J. M. *Chem. Rev.* **2010**, *110* (12), 6961–7001.

(28) Mayer, J. M. *Acc. Chem. Res.* **2011**, *44* (1), 36–46.

(29) Van de Walle, C. G. *Phys. Rev. Lett.* **2000**, *85* (5), 1012–1015.

(30) Cox, S. F. J.; Davis, E. A.; Cottrell, S. P.; King, P. J. C.; Lord, J. S.; Gil, J. M.; Alberto, H. V.; Vilão, R. C.; Piroto Duarte, J.; Ayres de Campos, N.; Weidinger, A.; Lichti, R. L.; Irvine, S. J. C. *Phys. Rev. Lett.* **2001**, *86* (12), 2601–2604.

(31) Lavrov, E. V.; Herklotz, F.; Weber, J. *Phys. Rev. B* **2009**, *79* (16), 165210.

(32) Shi, G. A.; Stavola, M.; Pearton, S. J.; Thieme, M.; Lavrov, E. V.; Weber, J. *Phys. Rev. B* **2005**, *72* (19), 195211.

(33) Anderson, N. A.; Lian, T. *Annu. Rev. Phys. Chem.* **2005**, *56* (1), 491–519.

(34) Wong, N. Z.; Ogata, A. F.; Wustholz, K. L. *J. Phys. Chem. C* **2013**, *117* (41), 21075–21085.

(35) Ardo, S.; Meyer, G. J. *Chem. Soc. Rev.* **2008**, *38* (1), 115–164.

(36) For hydrogen abstraction (PCET) from propane by a radical $X^{\bullet}$, $d[CH_3CH_2CH_3]/dt = \{2k_{2^\circ}(CH_3CH_2CH_3) + 6k_{1^\circ}(CH_3CH_2CH_3)\}[CH_3CH_2CH_3][X^{\bullet}]$ (the numbers reflecting the statistical weight of the different H's). This is a simple second order rate law that will give exponential decay of propane in the presence of excess $X^{\bullet}$ (the conditions used here for Equation 1).

(37) Pesika, N. S.; Stebe, K. J.; Searson, P. C. *J. Phys. Chem. B* **2003**, *107* (38), 10412–10415.

(38) Kohiki, S.; Nishitani, M.; Wada, T.; Hirao, T. *Appl. Phys. Lett.* **1994**, *64* (21), 2876–2878.

(39) Chianella, C.; Palombari, R.; Petricca, A. *Electrochimica Acta* **2006**, *52* (1), 369–372.

(40) Janotti, A.; Walle, C. G. V. de. *Rep. Prog. Phys.* **2009**, *72* (12), 126501.

(41) Nickel, N. H. *Phys. Rev. B* **2006**, *73* (19), 195204.

(42) Ip, K.; Overberg, M. E.; Heo, Y. W.; Norton, D. P.; Pearton, S. J.; Stutz, C. E.; Luo, B.; Ren, F.; Look, D. C.; Zavada, J. M. *Appl. Phys. Lett.* **2003**, *82* (3), 385–387.

(43) Knowles, K. E.; Malicki, M.; Weiss, E. A. *J. Am. Chem. Soc.* **2012**, *134* (30), 12470–12473.

(44) Norberg, N. S.; Gamelin, D. R. *J. Phys. Chem. B* **2005**, *109* (44), 20810–20816.

(45) Meulenkamp, E. A. *J. Phys. Chem. B* **1998**, *102* (29), 5566–5572.

(46) Schimpf, A. M.; Thakkar, N.; Gunthardt, C. E.; Masiello, D. J.; Gamelin, D. R. *ACS Nano* **2014**, *8* (1), 1065–1072.

Chapter 5. EXPLORING THE ELECTROCHEMICAL REDUCTION OF ZINC OXIDE NANOCRYSTALS USING SELF-ASSEMBELED MONOLAYERS

5.1 INTRODUCTION

The electrochemical and phase behavior of bulk metal-oxide materials under aqueous conditions are well documented in what have become known as Pourbaix diagrams.[1] These maps of chemical equilibria, with pH as the abscissa and electrochemical potential as the ordinate, are heavily used in the fields of corrosion and environmental sciences. Pourbaix diagrams prominently display the Nernstian shift of -59 mV per pH unit for many materials. This Nernstian behavior often tracks with the band edge potentials for semiconductors such as TiO_2 and ZnO. Lewis and coworkers exploited this Nernstian shift of band edge potential to study the driving force dependence on the interfacial electron transfer rate from single crystal ZnO to dissolved electron acceptors.[2] Lyon and Hupp demonstrated that the conduction band energy of nanocrystalline TiO_2 electrodes shift -64 mV per decade for over 30 proton activity units and concluded that at high proton concentrations, intercalation into nanocrystals must occur as the semiconductor-solution interface would be proton saturated.[3] Similar experiments with nanocrystalline ZnO electrodes, although in a narrower proton activity window, reached the same conclusion that electron injection into the conduction band is accompanied with proton interaction to maintain charge balance.[4]

Other studies of nanocrystalline ZnO electrodes have used spectroelectrochemistry to estimate flat band potentials of these films[5] or focused on charge storage and transport.[6] Some researchers have described the electron accumulation occurring in these films with a shell filling model.[7,8] Although some of these studies occurred after Hupp publications on ZnO and TiO_2, protons were not explicitly included in discussions of the results. For some time researchers have worried about the application of Gerischer model for semiconductor electrolyte interfaces being applied to films of nanocrystalline metal-oxides, specifically how charge compensating ions interact with the nanocrystals and what this means for bulk phenomena such as band bending.[9]

There are few studies on the electrochemistry of colloidal nanocrystals[10–13] and attempts in our lab using amine capped ZnO failed due to NC precipitation. While the modulation of the

reduction potential of ZnO NCs with protons was demonstrated in our lab with chemical reductants,[14] the ability to probe the relationship between NC reduction potential and protons with traditional electrochemistry would help us better understand the thermodynamic coupling of protons and electrons in non-aqueous conditions. Hoping to avoid some of the unknowns introduced from electrochemistry with NC films, a new approach of chemically anchoring ZnO NCs to gold electrodes has been explored. This method was inspired by a publication from the Murray group demonstrating reversible electrochemistry with iridium oxide (IrO_x) nanoparticles chemically anchored to gold electrodes.[11]

Self-assembled monolayers (SAMs) are formed by the adsorption of molecules onto substrates from homogenous solutions.[15] One of the most widely studied classes of SAMs is thiols adsorbed onto Au surfaces and the research has ranged from fundamental measurements of alkanethiol packing density on single crystal gold surfaces,[16] to testing the exponential distance dependence of the heterogeneous electron transfer rate from Marcus theory.[17,18] A few reports on CdTe and ZnSe NCs capped with thioglycolic and 3-mercapto-propionic acids demonstrated attaching the NCs to Au electrodes in order to study surface traps and bandgap size dependence electrochemically.[12,13] While these reports initially piqued our interest in exploring the electrochemistry of ZnO with SAMs, Murray's thoughtful analysis of data collected on IrOx NCs with C-8, C-12, and C-16 thiol-carboxylates SAMs steered us to use 12-mercaptododecanoic acid (MDA) to avoid uncompensated solution resistance encountered with thiolcarboxylates of C-8 and lower.

5.2 RESULTS

5.2.1 *Evidence of Formation of SAM and Attachment of ZnO NCs*

Cyclic voltammograms were obtained in 0.1 NaOH at scan rates of 250, 500, and 1000 mV/s with an Au working prior to and after being treated in 10 mM MDA for 24 hours. A decrease in the "charging" current associated with the electrochemical double layer can be observed after the Au electrode has been submerged in the MDA solution, indicating the formation of a SAM on the electrode surface, Figure 5.1a. The CVs obtained between 0.2 and -1.0 V *versus* Ag/AgCl with MDA treated electrode show an increase in current with scan rate and are reversible indicating stability of the SAM in this potential window, Figure 5.1b. Electrodes treated with

MDA followed by submersion in ethanolic solutions of uncapped ZnO NCs yielded CVs with slightly higher currents than electrodes treated only with MDA, Figure 5.1c. From overlaying the 500 mV/s CVs of the MDA and MDA/ZnO treated electrodes the increase in current as well as a cathodic feature near -0.6 V become obvious, Figure 5.1d. No reversible couple for the reduction and oxidation of ZnO NCs was observed. Similar results were obtained for CVs collected in acetonitrile with 0.1 M [TBA][PF_6] supporting electrolyte.

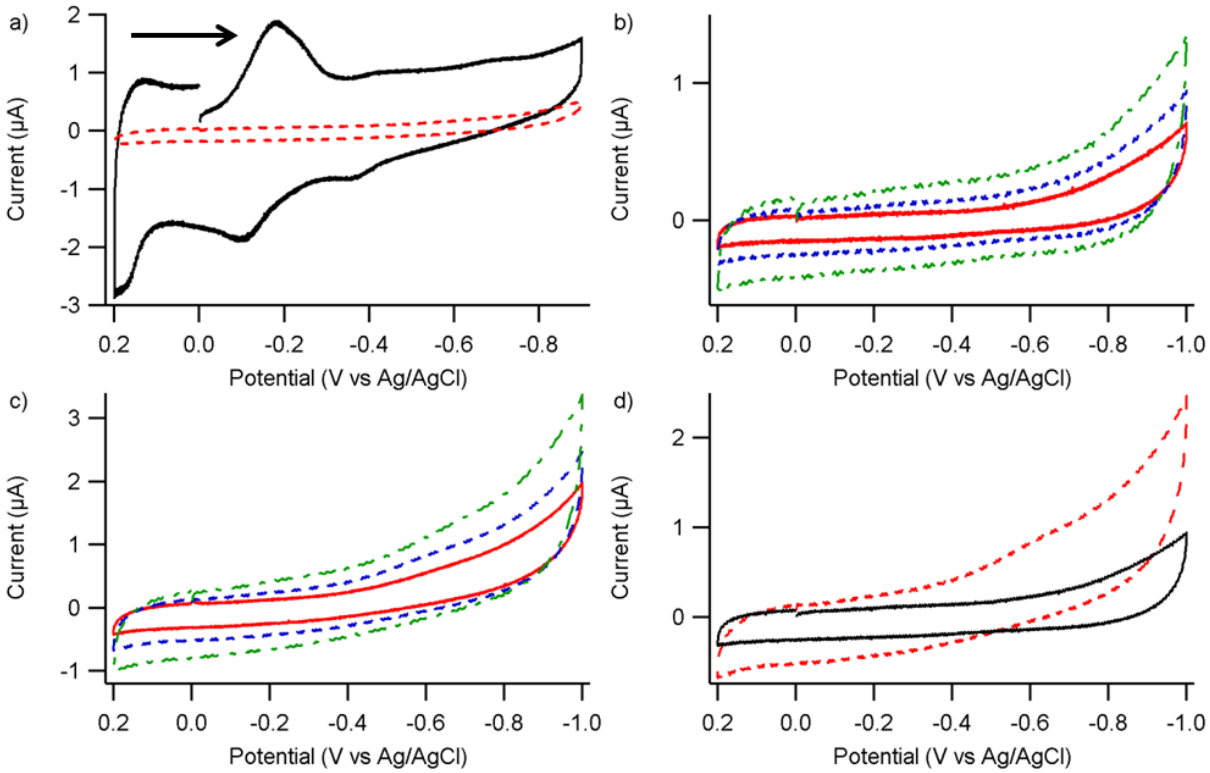

Figure 5.1. Cyclic voltammograms obtained in 0.1 M NaOH. a) Comparison of the signals from 500 mV/s sweep of the bare Au electrode (black, solid) and the MDA treated electrode (red, dashed) between 0.2 and -0.9 V. Black arrow indicates direction of potential sweep. b) Signal from the MDA treated Au electrode at different scan rates: 250 mV/s (red, solid); 500 mV/s (blue, dashed); 1000 mV/s (green, dot-dashed). c) Signal from the MDA/ZnO treated Au electrode at different scan rates: 250 mV/s (red, solid); 500 mV/s (blue, dashed); 1000 mV/s (green, dot-dashed). d) An overlay of the scans for the MDA treated (black, solid) and MDA/ZnO treated (red, dashed) Au electrode at 500 mV/s.

5.2.2 *Exploring SAMs by Chronocoulometry*

Observing no reversible couple from the CVs of the MDA/ZnO treated electrodes, chronocoulometry was performed with MDA and MDA/ZnO electrodes between -0.100 and -0.875 V to search for reductive features, see section 5.5.4. Briefly, treated electrodes were placed in electrolyte, a potential of 0.0 V was applied, the potential was stepped to a more negative potential and held for 250 seconds, then the potential was stepped back to 0.0V and held for 250 ms, Figure 5.2a. The maximum cathodic charge passed at each step potential was measured and plotted against the potential at which it was measured, Figure 5.2b. The maximum charge passed increased with decreasing potential and the total charge passed was greater for the MDA/ZnO treated electrodes than for the MDA treated electrodes. The difference in charge passed between MDA/ZnO and MDA treated electrodes in 0.1 M NaOH showed large increase starting at around -0.450 V, Figure 5.2c. Data collected in acetonitrile with 0.1 M [TBA][PF_6] electrolyte did not display a notable difference in the charge passed until about -0.575 V, Figure 5.2d. While no quantitative conclusions can be drawn for this data, the difference in passed charge for the MDA/ZnO and MDA treated electrodes provide further evidence for the attachment of ZnO NCs to the carboxylate functional groups of the SAMs.

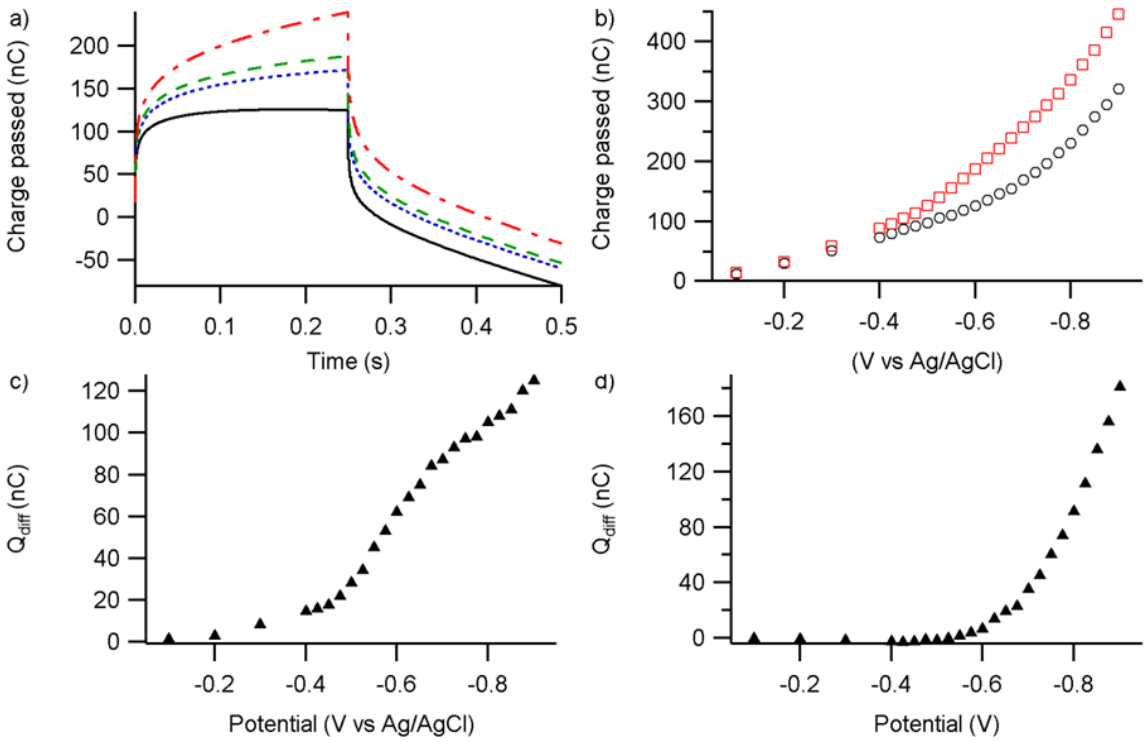

Figure 5.2. a) Chronocoulometric data from an MDA/ZnO treated Au electrode with step potentials of -500 mV (black, solid); -575 mV (blue, dotted); 600 mV (green, dashed); and -675 mV (red, dot-dashed) in 0.1 M NaOH. b) Maximum charged passed versus potential for MDA (black, circles) and MDA/ZnO (red, squares) in 0.1 M NaOH. c) Difference in the maximum passed charge for the MDA/ZnO and MDA treated electrodes from panel (b). d) Difference in the maximum passed charge for the MDA/ZnO and MDA treated electrodes in acetonitrile with 0.1 M [TBA][PF_6].

Questioning the results of the first chronocoulometry experiments, a new method of data collection was devised, stepping to the most negative potentials first and measuring the electrode response for longer periods of time, 5 seconds. CVs of the electrodes were also obtained before and after the chronocoulometry experiments to test the stability of the SAMs. The total difference in maximum charge passed for an MDA/ZnO versus MDA treated electrode in 0.1 M NaOH was much larger than previously observed between -0.200 and -0.775 V, Figure 5.3a. The CVs of the MDA/ZnO treated electrodes obtained before and after chronocoulometry were very similar, but the CVs of the electrode only treated with MDA were quite different suggesting degradation of the SAM during chronocoulometry, Figure 5.3c. The increase in the total

difference in charge passed in Figure 5.3a is probably from the degradation of the SAM. In 0.1 M LiOH, however, the difference in maximum charge data increases linearly until -0.400 V where it plateaus until -0.750 V, Figure 5.3b. The CVs obtained before and after chronocoulometry in 0.1 M LiOH overlay fairly well for both the MDA and MDA/ZnO electrodes suggesting that the SAM is stable with the LiOH electrolyte.

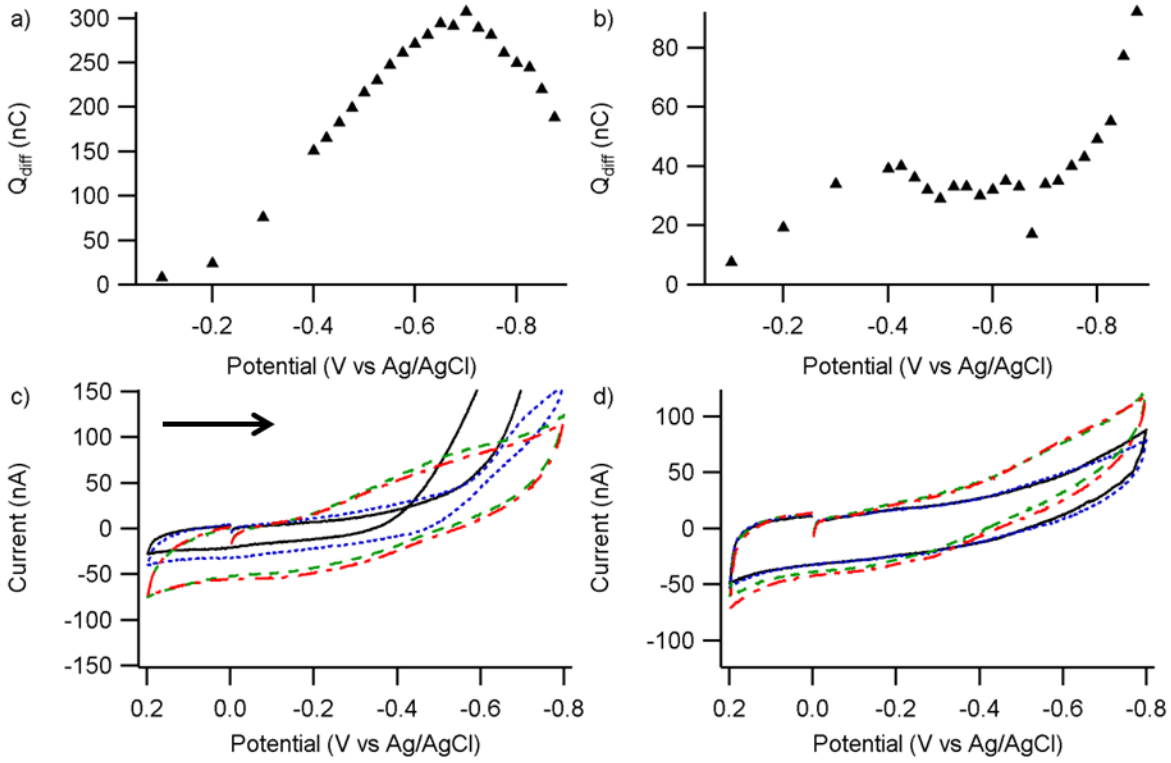

Figure 5.3. Difference in the maximum passed charge for the MDA/ZnO and MDA treated electrodes in 0.1 M NaOH (a) and 0.1 M LiOH (b) measuring the most negative potentials first. Cyclic voltammograms of the MDA treated electrodes before (black, solid) and after (blue, dotted) the chronocoulometry measurements compared with MDA/ZnO treated electrodes before (green, dashed) and after (red, dot-dashed) the chronocoulometry measurements in 0.1 M NaOH (c) and 0.1 M LiOH at 20 mV/s (d). Black arrow in (c) indicates direction of potential sweep.

5.2.3 *Other Solvents and Electrolytes*

Having not observed reversible NC reduction under aqueous conditions, experiments were extended into organic solvents with a few different electrolytes. Cyclic voltammograms collected at a scan rate of 20 mV/s in ethanolic 0.1 M $NaPF_6$, displayed a sharp, irreversible increase in current around -0.600 V for MDA treated electrodes when scanned out to -0.800 V; black, solid and blue, dotted traces, Figure 5.4. Data collected under the same conditions for MDA/ZnO treated electrodes was fairly featureless, showing a slight increase in current before the negative switching potential; green, dashed and red, dot-dashed, Figure 5.4. Comparing the CVs from the MDA and MDA/ZnO treated electrodes implies that the SAM is not stable on its own under the given conditions, and the ZnO treated SAM is stable, but potentials sufficient to reduce the ZnO NCs were not reached.

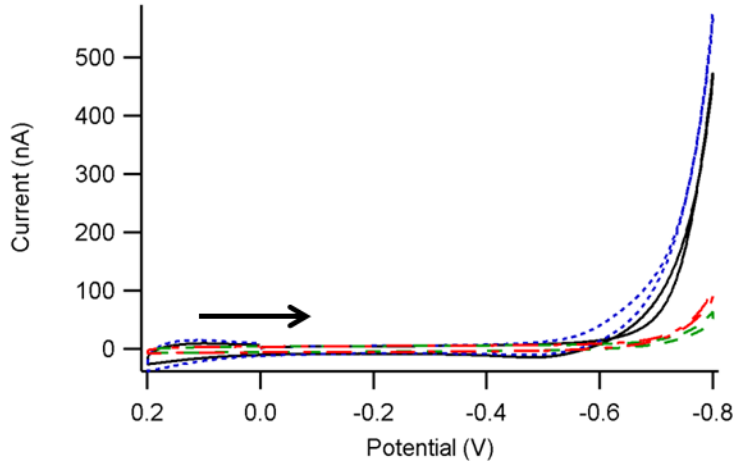

Figure 5.4. Successive cyclic voltammograms of MDA and MDA/ZnO treated electrodes in ethanolic 0.1 M $NaPF_6$ obtained at 20 mV/s: MDA 1st (black, solid) and 2nd (blue, dotted); MDA/ZnO 1st (green, dashed) and 2nd (red, dot-dashed). Black arrow indicates direction of potential sweep.

Data collected in ethanolic $LiPF_6$ at a scan rate of 20 mV/s led to some peculiar observations. Successive cyclic voltammograms collected with an MDA/ZnO treated electrode between 0.200 and -0.600 V overlaid well with each other and had no reductive features; black, solid and blue, dashed Figure 5.5. When the scans were extended to -0.800 V, the current began to increase around -0.625 V, the CV "crossed" over twice on the return, and a anodic peak could

be observed at -0.465 V, Figure 5.5 inset. Cyclic voltammograms obtained in the 0.200 to -0.600 V potential window, after the scan to more negative potentials, displayed an increase in current starting around -0.325 V and an anodic peak at -0.425 V; green, dashed Figure 5.5.

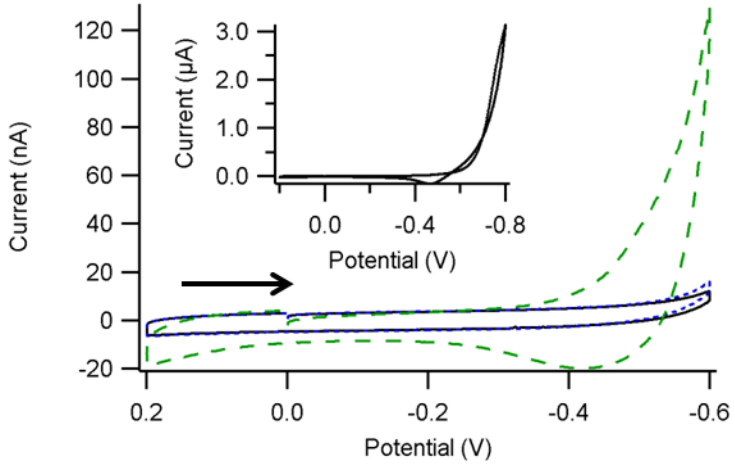

Figure 5.5. Successive cyclic voltammograms MDA/ZnO treated electrodes in ethanolic 0.1 M $LiPF_6$ obtained at 20 mV/s in the potential window between 0.2 and -0.6 V: MDA/ZnO 1st (black, solid) and 2nd (blue, dotted). The black arrow indicates the direction of the potential sweep. The 3rd (green, dashed) CV was obtained after scanning out to -0.8V (inset) and observing nonreversible behavior at such reducing potentials.

Since some of the CVs with $LiPF_6$ as the supporting electrolyte displayed both cathodic and anodic features, experiments were run with LiCl at 0.1 M in ethanol. When data were collected at a scan rate of 20 mV/s, the MDA treated electrodes gave reversible cyclic voltammograms between 0.200 and -1.0 V, although the second CV in a series (blue, dotted) had less current at negative potentials than the first CV (black, solid), Figure 5.6a. The first CV obtained with MDA/ZnO treated electrode (green, dashed) showed a sharp increase in current at about -0.780 V with a peak current at -0.960 V. The reduction was irreversible and had two "crossovers" on the return scan. The second CV obtained with the MDA/ZnO treated electrode (red, dot-dashed) displayed an increase in current at a lower potential, about -0.530 V, with a peak current also lower in potential, -0.860 V, again containing two "crossover" features.

Data collected at a faster scan rate, 100 mV/s, between 0.200 and -0.900 V was cleaner than the data collected at 20 mV/s because no "crossovers" were present. The CVs from MDA/ZnO treated electrodes showed in increase in current at -0.480 V that plateaued

around -0.880 V; blue, dotted and green dashed Figure 5.6b. On the reverse scan, an anodic "shoulder" was present at about -0.590 V. The reductive current for the MDA/ZnO treated electrodes was greater in magnitude than that from the electrodes when treated with only MDA, black, solid Figure 5.6b and may be evidence for nonreversible NC reduction.

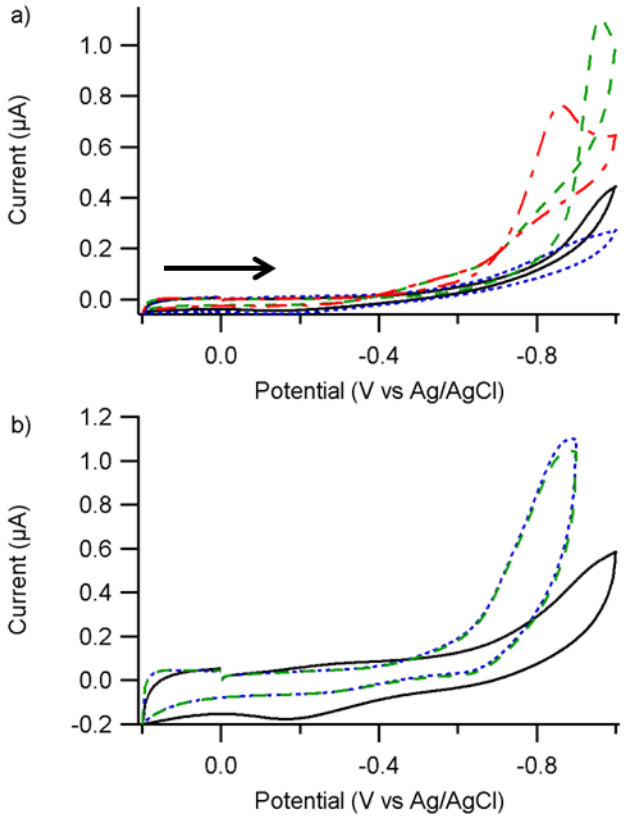

Figure 5.6. a) Successive cyclic voltammograms of MDA and MDA/ZnO treated electrodes in ethanolic 0.1 M LiCl obtained at 20 mV/s: MDA 1st (black, solid) and 2nd (blue, dotted); MDA/ZnO 1st (green, dashed) and 2nd (red, dot-dashed). The black arrow indicates the potential sweep direction. b) Cyclic voltammograms of MDA treated (black, solid) and MDA/ZnO treated electrodes in ethanolic 0.1 M LiCl obtained at 100 mV/s: 1st (blue, dotted) and 2nd (green, dashed).

With moderate success in observing reductive current possible associated with NC reduction using LiCl as the in ethanol, experiments in the aprotic solvent tetrahydrofuran (THF) were planned. Electrolyte was prepared at 0.2 M and CVs obtained with MDA treated electrodes showed reversible charging current between 0.200 and -0.800 V; black, solid and blue, dotted, Figure 5.7. Data collected with the MDA/ZnO treated electrodes had charging currents that were

smaller than the MDA treated electrodes and no reductive features close indicative of NC reduction; green, dashed and red, dot-dashed, Figure 5.7.

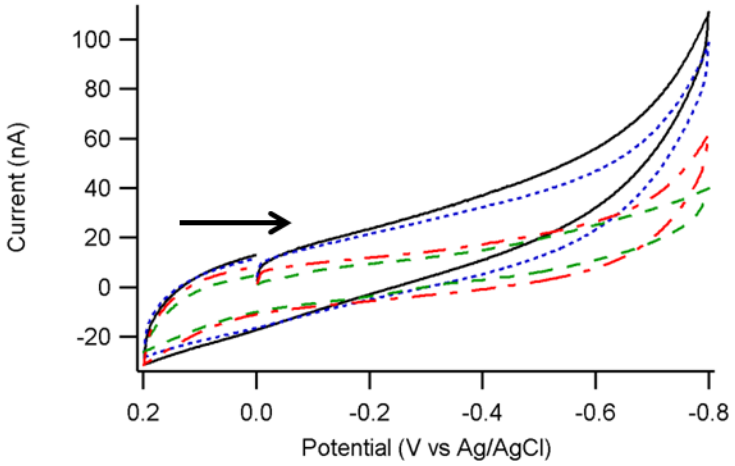

Figure 5.7. Successive cyclic voltammograms of MDA and MDA/ZnO treated electrodes in 0.2 M LiCl obtained at 100 mV/s: MDA 1st (black, solid) and 2nd (blue, dotted); MDA/ZnO 1st (green, dashed) and 2nd (red, dot-dashed). The black arrow indicates the direction of the potential sweep.

5.3 Discussion

The experiments in 0.1 M NaOH did not demonstrate reversible ZnO NC reduction, but they did establish that SAMs of MDA were forming on the gold electrodes and that the SAMs were stable between 0.200 and -1.00 V vs Ag/AgCl in good agreement with literature about SAMS of alkanethiols on gold surfaces.[19] The CVs obtained with the MDA/ZnO treated electrodes did have larger charging currents than the electrodes only treated with MDA and displayed reductive features around -0.600 V, suggesting attachment of ZnO NCs. No reversible NC reduction was observed under these conditions which may be attributed to two factors that were initially overlooked. The first being that in solution with a high pH value the conduction band energy of ZnO would be shifted from -0.4 V vs NHE to higher potentials, somewhere between -1.1 and -1.2 V. At these potentials NC reduction would be in competition with reductive thiol desorption.[20] At high pH ZnO could also begin to dissolve, so the NCs were most likely etched off upon submerging the MDA/ZnO treated electrodes in the 0.1 M NaOH.[21]

The results obtained in ethanol with lithium electrolytes suggest the irreversible reduction of ZnO NCs. The data presented in Figure 5.5 clearly show reductive current occurring during the CV taken out to -0.800 V and in the CV collected afterward but only swept out to -0.600 V. The observed shape of the CVs, sharp reduction peak and small oxidation peak, are very similar to those obtained with ZnO NC films in acetonitrile with 0.1 M lithium perchlorate and 0.1 M tetrabutylammonium perchlorate.[22] The observation that reduction occurs at lower potentials after the scan out to -0.800 V implies some type of electrochemical hysteresis. The authors of a study on how different electrolyte and solvent combinations influence the electrochemical behavior of TiO_2 nanoparticle films, describe running several "conditioning" CVs at 10 mV/s before collecting data noting that these conditioning CVs were required to obtain reproducible data.[23] It could be that with MO_x NC films and MDA/ZnO treated electrodes, there is some electrochemical hysteresis related to intercalation of counter ions occurring during the NC reduction. The small or nonexistent anodic current may be attributed to reduction of advantageous O_2.

The CVs obtained with MDA/ZnO treated electrodes in ethanolic LiCl had similar features to those obtained with $LiPF_6$. At the scan rate of 20 mV/s the CVs were irreversible, but reduction was observed and it occurred at lower potentials on successive scans. Afterwards when data was collected with a scan rate of 100 mV/s, successive voltammograms overlaid and contained an anodic shoulder during the return scan. The data did not contained the well-defined redox couple observed with IrO_x nanoparticles attached to SAMs,[11] but if compared with the CVs obtained with ZnO and TiO_2 films mentioned previously, the data suggests the cathodic current is from the reduction of ZnO NCs. In Boschloo and Fitzmaurice's work with nanocrystalline TiO_2 films, TiO_2 reduction was observed at lower potentials in acidic water than in acetonitrile with the same concentrations of lithium perchlorate electrolyte.[23] The data collected in the aprotic THF solvent did not contain the reductive features observed in ethanol which implies that protons from solvent, not lithium ions, are involved in the cathodic features observed in ethanolic solutions.

5.4 CONCLUSIONS

SAMs of 12-mercaptododecanoic acid were prepared on Au electrodes. These SAMs were submerged in ethanolic solutions of ZnO NCs and electrochemical measurements were obtained

in a variety of solvents and electrolytes. Data obtained in 0.1 M NaOH and LiOH did not contain any evidence of NC reduction, most likely due to dissolution of the ZnO under the conditions. In ethanolic solutions of $LiPF_6$ and LiCl cathodic and anodic features were observed in CVs. Given the similarity of the features observed in the CVs the MDA/ZnO treated electrodes with those observed with nanocrystalline ZnO thin films, I attribute these features ZnO NC reduction and oxidation. This result contrasts with a lack of cathodic features observed with LiCl in THF and implies that protons are involved in the electrochemical reduction of ZnO NCs observed in this chapter.

5.5 EXPERIMENTAL

5.5.1 *General Considerations*

Acetonitrile was obtained from Fisher Scientific and used as received. Absolute ethanol was purchased from Decon and used as received. Ultrapure water, ChromAR, was obtained from Mallinckrodt. Tetrabutylammonium hexafluorophosphate [TBA][PF_6] was obtained from Sigma-Aldrich, recrystallized three times from hot ethanol and dried overnight on a Schlenk line with mild heating (30 °C) before use. All other substrates and metal-oxide precursors were purchased from Sigma-Aldrich and used as received unless otherwise noted. Electrochemical measurements were obtained on either a BASI Epsilon or CHI 650D potentiostat in a three electrode cell arrangement, using a gold (2 mm diameter) working electrode, platinum auxiliary electrode and either Ag/AgCl, Ag/$AgNO_3$ or Ag wire reference depending on the conditions.

5.5.2 *Preparation of SAMs and attachment of ZnO NCs*

Standard, 2mm diameter, Au electrodes were cleaned in piranha solution (sulfuric acid, 3 mL: hydrogen peroxide, 1 mL) for 2 minutes. The electrodes were then rinsed twice with about 4 mL of ultrapure water, followed by about 4 mL of absolute ethanol. The cleaned, rinsed electrodes were then submerged into an ethanolic 1 mM solution of 12-mercaptododecanoic acid (60 mg) previous prepared in a 25 mL volumetric flask. The electrodes were allowed to rest in the thiol-carboxylate solution for 24 hours to allow for Au-thiol SAM formation. Prior to electrochemical measurements, the electrodes were removed and rinsed with the electrolyte being used that day.

When attaching ZnO NCs to the SAMs, the electrodes were rinsed with absolute ethanol and placed in the solution of uncapped ZnO NCs and left in a freezer (-35 °C) for 48 hours.

5.5.3 *Electrochemical Measurements: Cyclic Voltammetry*

Cyclic voltammograms (CVs) were obtained in a variety of solvent and electrolyte combinations at scan rates ranging from 20 to 1000 mV per second. CVs were collected by scanning in the negative direction starting at 0 V, switching direction at the lowest potential, scanning to 200 mV and then returning to 0V. Data collected under aqueous conditions was referenced to the Ag/AgCl couple. Data collected in organic solvents was collected with either an Ag/AgCl electrode or a silver wire. Measurements were made after the electrolytes were purged with N_2 for at least ten minutes, and an N_2 blanket was maintained over the solutions during data collection.

Table 5.6. Electrolyte Preparation

Electrolyte	Solvent	Molarity (mol/L)	Volume (mL)	Mass (g)
NaOH	Water	0.1	50	0.20
NH_4PF_6	Acetonitrile	0.1	100	3.87
$LiOH \bullet H_2O$	Water	0.1	50	0.21
$NaPF_6$	Ethanol	0.1	25	0.42
$LiPF_6$	Ethanol	0.1	25	0.38
LiCl	Ethanol	0.1	50	0.21
LiCl	Tetrahydrofuran	0.2	50	0.42

5.5.4 *Electrochemical Measurements: Chronocoulometry*

Chronocoulometry measurements were obtained by two different methods for both MDA and MDA/ZnO treated electrodes. In the first method, data was collected from the least reducing to the most reducing potentials Briefly, the voltage was held at 0.0 V for three seconds, then the voltage was stepped to a more negative potential which was held for 250 ms, followed by a step back to 0.0 V which was held for 250 ms. This procedure was repeated for each potential stepped to between 0 and -0.875V. Between -0.100 and -0.400 V the step increment was 100 mV. From -0.400 to -0.875 V the step increment was 25 mV. In the second method, data was collected from the most reducing to the least reducing potentials. The same step increments were used, but the initial potential of 0.0 V was held for 2 seconds, followed by a step to a more

reducing potential which was help for 5 seconds, before being step back to 0.0 V and held for 5 seconds. The data was analyzed by plotting the maximum charge passed during the cathodic step against the potential at which it was measured.

5.6 NOTES

(1) Marcel. Pourbaix. *Atlas of electrochemical equilibria in aqueous solutions,* [1st English ed.].; Oxford, New York, Pergamon Press, 1966.

(2) Hamann, T. W.; Gstrein, F.; Brunschwig, B. S.; Lewis, N. S. *Chem. Phys.* **2006**, *326* (1), 15–23.

(3) Lyon, L. A.; Hupp, J. T. *J. Phys. Chem. B* **1999**, *103* (22), 4623–4628.

(4) Lemon, B. I.; Hupp, J. T. *J. Phys. Chem. B* **1997**, *101* (14), 2426–2429.

(5) Redmond, G.; O'Keeffe, A.; Burgess, C.; MacHale, C.; Fitzmaurice, D. *J. Phys. Chem.* **1993**, *97* (42), 11081–11086.

(6) Hoyer, P.; Weller, H. *J. Phys. Chem.* **1995**, *99* (38), 14096–14100.

(7) Roest, A. L.; Kelly, J. J.; Vanmaekelbergh, D.; Meulenkamp, E. A. *Phys. Rev. Lett.* **2002**, *89* (3).

(8) Roest, A. L.; Germeau, A.; Kelly, J. J.; Vanmaekelbergh, D.; Allan, G.; Meulenkamp, E. A. *ChemPhysChem* **2003**, *4* (9), 959–966.

(9) Berger, T.; Monllor-Satoca, D.; Jankulovska, M.; Lana-Villarreal, T.; Gómez, R. *ChemPhysChem* **2012**, *13* (12), 2824–2875.

(10) Bae, Y.; Myung, N.; Bard, A. J. *Nano Lett.* **2004**, *4* (6), 1153–1161.

(11) Gambardella, A. A.; Feldberg, S. W.; Murray, R. W. *J. Am. Chem. Soc.* **2012**, *134* (13), 5774–5777.

(12) Poznyak, S. K.; Osipovich, N. P.; Shavel, A.; Talapin, D. V.; Gao, M.; Eychmüller, A.; Gaponik, N. *J. Phys. Chem. B* **2005**, *109* (3), 1094–1100.

(13) Gaponik, N.; Poznyak, S. K.; Osipovich, N. P.; Shavel, A.; Eychmüller, A. *Microchim. Acta* **2008**, *160* (3), 327–334.

(14) Valdez, C. N.; Braten, M.; Soria, A.; Gamelin, D. R.; Mayer, J. M. *J. Am. Chem. Soc.* **2013**, *135* (23), 8492–8495.

(15) *Electroanalytical chemistry; a series of advances.*; Bard, A. J., Rubinstein, I., Eds.; Boca Raton, FL CRC Press, Taylor & Francis Group, 1996; Vol. 19.

(16) Love, J. C.; Estroff, L. A.; Kriebel, J. K.; Nuzzo, R. G.; Whitesides, G. M. *Chem. Rev.* **2005**, *105* (4), 1103–1170.

(17) Adams, D. M.; Brus, L.; Chidsey, C. E. D.; Creager, S.; Creutz, C.; Kagan, C. R.; Kamat, P. V.; Lieberman, M.; Lindsay, S.; Marcus, R. A.; Metzger, R. M.; Michel-Beyerle, M. E.; Miller, J. R.; Newton, M. D.; Rolison, D. R.; Sankey, O.; Schanze, K. S.; Yardley, J.; Zhu, X. *J. Phys. Chem. B* **2003**, *107* (28), 6668–6697.

(18) Eckermann, A. L.; Feld, D. J.; Shaw, J. A.; Meade, T. J. *Coord. Chem. Rev.* **2010**, *254* (15-16), 1769–1802.

(19) Widrig, C. A.; Chung, C.; Porter, M. D. *J. Electroanal. Chem. Interfacial Electrochem.* **1991**, *310* (1-2), 335–359.

(20) Walczak, M. M.; Popenoe, D. D.; Deinhammer, R. S.; Lamp, B. D.; Chung, C.; Porter, M. D. *Langmuir* **1991**, *7* (11), 2687–2693.

(21) Meulenkamp, E. A. *J. Phys. Chem. B* **1998**, *102* (40), 7764–7769.

(22) Willis, R. L.; Olson, C.; O'Regan, B.; Lutz, T.; Nelson, J.; Durrant, J. R. *J. Phys. Chem. B* **2002**, *106* (31), 7605–7613.

(23) Boschloo, G.; Fitzmaurice, D. *J. Phys. Chem. B* **1999**, *103* (37), 7860–7868.

Chapter 6. SCREENING METAL-OXIDES AS CATALYSTS FOR THE ELECTROOXIDATION OF ALKANES

6.1 INTRODUCTION

6.1.1 *Motivation*

The development of efficient and sustainable ways to convert and store electrical energy has presented an evolving challenge to scientist and engineers for at least a century.[1] Hydrocarbons provide the highest energy density by volume or weight compared to hydrogen or batteries, but little current technology exists to efficiently convert the energy stored in the chemical bonds of hydrocarbons into electricity. Solid oxide fuel cells are used to generate electricity from methane, but these devices are not portable and operate at high temperatures 800-1000 °C.[2] The research described below was inspired by a vision from Defense Advanced Research Projects Agency to develop a low temperature, wearable alkane fuel cell. The creation of such a device hinges on the discovery of cheap and efficient hydrocarbon oxidation catalysts.

6.1.2 *Vision and Method*

Previous work in the Mayer lab with TiO_2 and ZnO nanoparticles (NPs) demonstrated that when reduced, these metal-oxides (MO_x) can transfer electrons (e^-) and protons (H^+) to organic reagents in an effective hydrogen atom transfer reaction.[3] Because these metal oxides (MO_x) are able to transfer e^- and H^+, it was proposed that the reaction may be run backwards using holes generated by an applied bias to oxidize C–H bonds; with surface oxygen atoms acting as a base to accept protons Figure 6.1.

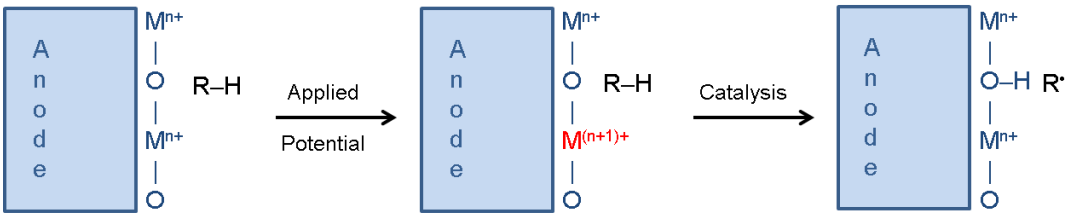

Figure 6.1. Envisioned scheme for C–H oxidation with MO_x electrocatalyst.

The first organic substrate screened, 9,10-dihydroanthracene (DHA), was chosen because its main oxidation product, anthracene, is readily identifiable by UV-Vis spectroscopy[4] and it contains a relatively weak C–H bond Scheme 6.1. The bond dissociation free energy (BDFE), which is the energy required to homolytically cleave an X–H bond, is 76 kcal/mol for DHA. This BDFE is fairly low for a C–H bond, considering that the BDFEs of methane and the methyl C–H of toluene are 102 and 87 kcal/mol respectively.[5] By choosing a substrate with a relatively weak C–H bond, there it was assumed there would be a higher likelihood of observing oxidation through a concerted proton coupled electron transfer (CPET) mechanism. As the project progressed the organic substrate scope was expanded to include alkylated benzenes and phenylated carboxylic acids.

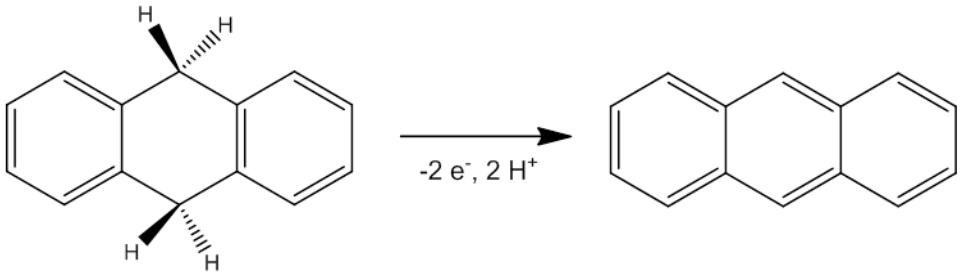

Scheme 6.1. Oxidation of 9,10-dihydroanthracene to anthracene.

6.2 RESULTS

6.2.1 *Overview of MO_x Anodes Screened During Study and Benchmarking*

Over the course of the study 17 different MO_x anodes were screened in acetonitrile (MeCN) with tetrabutylammonium hexafluorophosphate (NBu_4PF_6) electrolyte, aqueous potassium hydroxide solution or both. Background cyclic voltammograms were obtained in just electrolyte, followed by CVs in the same potential window with substrate present. Some of the MO_X electrodes displayed an increased non-reversible oxidation starting at about 1.5 V vs NHE when DHA was present while others showed little or no increase in current. The Fluorine-doped Tin Oxide (FTO) anodes that the MOx were deposited on showed modest oxidation activity (Figure 6.2 a) while α-Fe_2O_3, a known photoelectrochemical water oxidation catalyst,[6] did not show evidence for the oxidation of DHA (Figure 6.2 b). The MO_x that displayed the largest current densities in organic solutions was Nickel Oxide (NiO). It should be noted that anthracene is oxidized at a

lower potential than DHA, about 1.30 V, and that much higher current densities were observed, about 3 orders of magnitude, at substrate concentrations 18 times lower (Figure 6.2 c & 6.3 a).

To demonstrate that the oxidative current observed starting at around 1.5 V was from the oxidation of DHA to the anthracene, Controlled Potential Electrolysis (CPE) was performed. An "H-cell" with 55 mM DHA solution was prepared with an NiO electrode separated from the reference electrode, and CPE was run for 15 minutes at 1.72 V. UV-visible spectra were obtained from the substrate solutions before and after the CPE. The spectrum obtained previous to electrolysis displayed a sharp increase in absorbance starting at 280 nm. The spectrum of the post electrolysis solution contained five peaks in the Near UV at 310, 324, 340, 357, and 376 nm which are from anthracene produced during oxidation of DHA (Figure 6.3 b).[4]

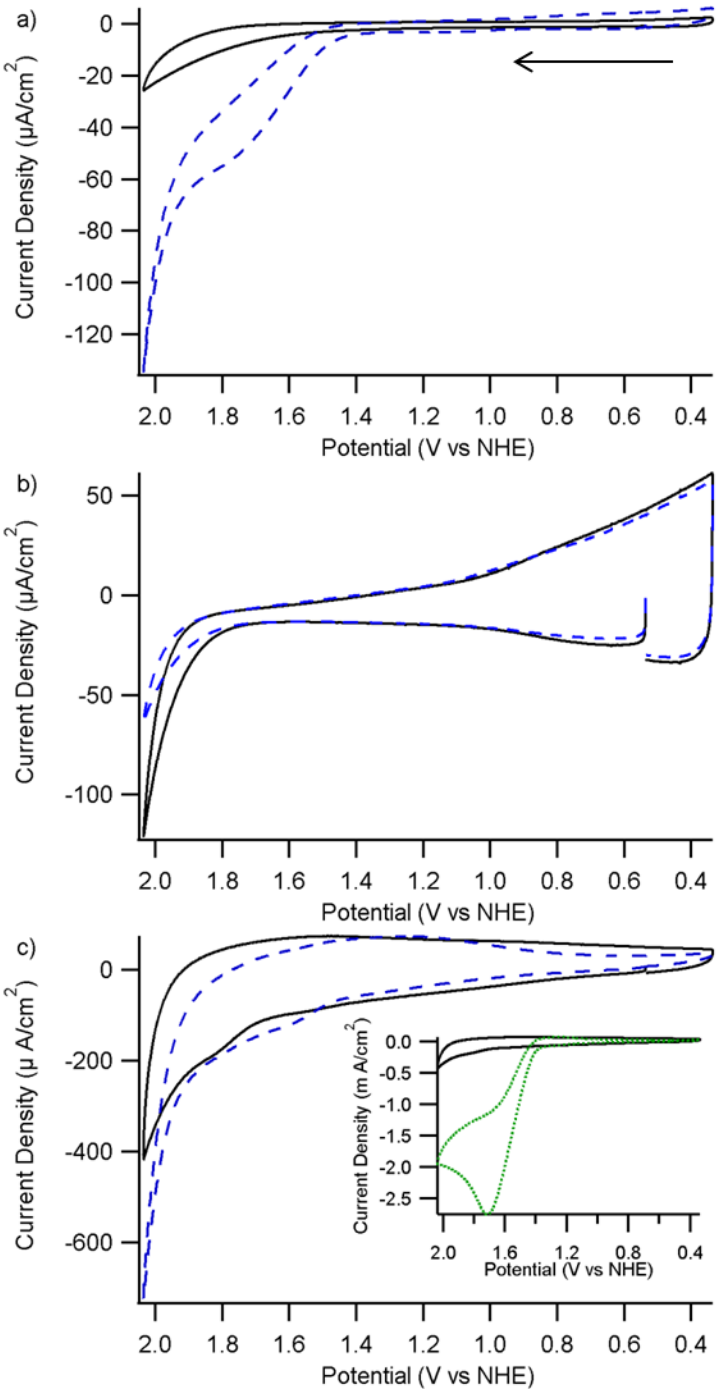

Figure 6.2. Cyclic voltammograms of FTO (a) , α-Fe_2O_3 (b), and NiO (c) in electrolyte (0.1 M NBu_4PF_6, MeCN) solution (black, solid) for a background current and 55 mM DHA solution (blue, dashed). The arrow in (a) indicates the potential sweep direction (50 mV/s). The inset shows the response of the NiO anode in 3mM anthracene (green, dotted).

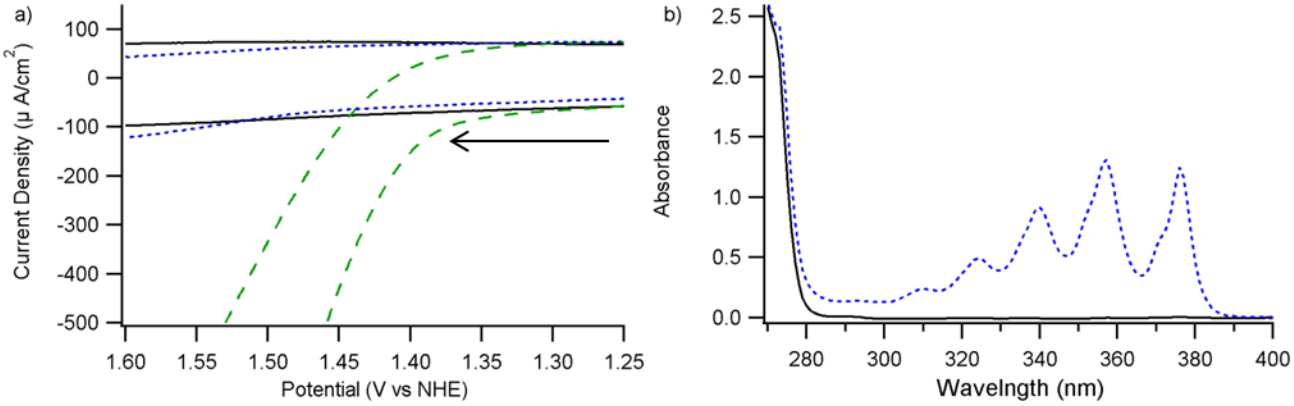

Figure 6.3. a) Overlay of CVs from NiO anode in electrolyte (0.1 M NBu_4PF_6, MeCN) solution (black, solid), 55 mM DHA (blue, dotted) and 3mM anthracene (green, dashed). The arrow in (a) indicates the potential sweep direction (50 mV/s). b) UV-Visible spectra of DHA solution before (black, solid) and after 15 minutes of controlled potential electrolysis at 1.72 V.

Table 6.7. Metal-Oxide Anode Screening Summary

Metal-Oxide	Reason for Screen	Notes
Zinc Oxide (ZnO)^{O}	Observed PCET reactivity[3]	Low current dens
Titanium Dioxide (TiO_2)^{O}	Observed PCET reactivity[3]	No oxidation
Nickel Oxide (NiO)^{B}	Oxidizes alcohol, amines, & water[7,8]	High current dens
Cerium Oxide (CeO_2)^{O}	Catalyst in SOFC[9]	No oxidation
Iron Oxide (α-Fe_2O_3)^{O}	Water Oxidation Catalyst (WOC)[6]	No oxidation
Tungsten Trioxide (WO_3)^{O}	WOC	No oxidation
Bismuth Vanadate ($BiVO_4$)^{O}	WOC	Low current dens
Vanadium Pentoxide (V_2O_5)^{B}	Oxidized methane to methanol[10]	Interesting feature at low potential
Ruthenium Oxide (RuO_2)^{B}	Oxidized ethylene to CO_2[11]	High current dens
Lithium Nickel Cobalt Aluminum Oxide^{O}	Battery Cathode Material[12]	Unstable film
Lithium Manganese Nickel Cobalt Oxide^{O}	Battery Cathode Material	Unstable film
Iridium Oxide (IrO_x)^{B}	WOC[13]	Modest current dens
Cobalt Oxide (CoO_x)^{B}	WOC[14]	Modest current dens
Nickel-Iron Oxide ($Ni_xFe_yO_z$)^{A}	WOC[14,15]	Similar to NiO
Nb doped Nickel Oxide (Nb:NiO)^{B}	Computational Prediction[16]	No oxidation
Niobium Pentoxide (Nb_2O_5)^{B}	Compare activity to Nb:NiO	Low current dens
Nickel Foil ($Ni(OH)_2$)^{A}	Ethanol oxidation catalyst[17]	Low current dens

Solvent System(s) Tested In: ^{A}- aqueous; ^{O}- organic; ^{B}- both.

6.2.2 *Comparison of Top Performing MO_x*

Of the 17 MO_x electrodes screened, NiO and RuO_2 displayed the highest current densities for the oxidation of DHA, Figure 6.4 a and b respectively. At 1.45 and 1.55 V NiO and RuO_2 displayed current densities of 97 and 132 and 33 and 83 $\mu A/cm^2$ respectively. To account for the difference in surface roughness the double-layer capacitance (C_{DL}), which is an estimate of the area of the solid-liquid interface,[18] was determined for an FTO and top the performing NiO and RuO_2 electrodes. These C_{DL} values were obtained by calculating the difference in cathodic and anodic current (ΔJ) for electrodes at different scan rates, Figure 6.4c. The C_{DL} is then obtained from one-half of the slope of ΔJ versus scan rate, Figure 6.4d. The FTO electrode had a C_{DL} of 0.35 $\mu F/cm^2$. The RuO_2 and NiO electrodes had greater C_{DL}s of 4.35 and 14.75 $\mu F/cm^2$ respectively.

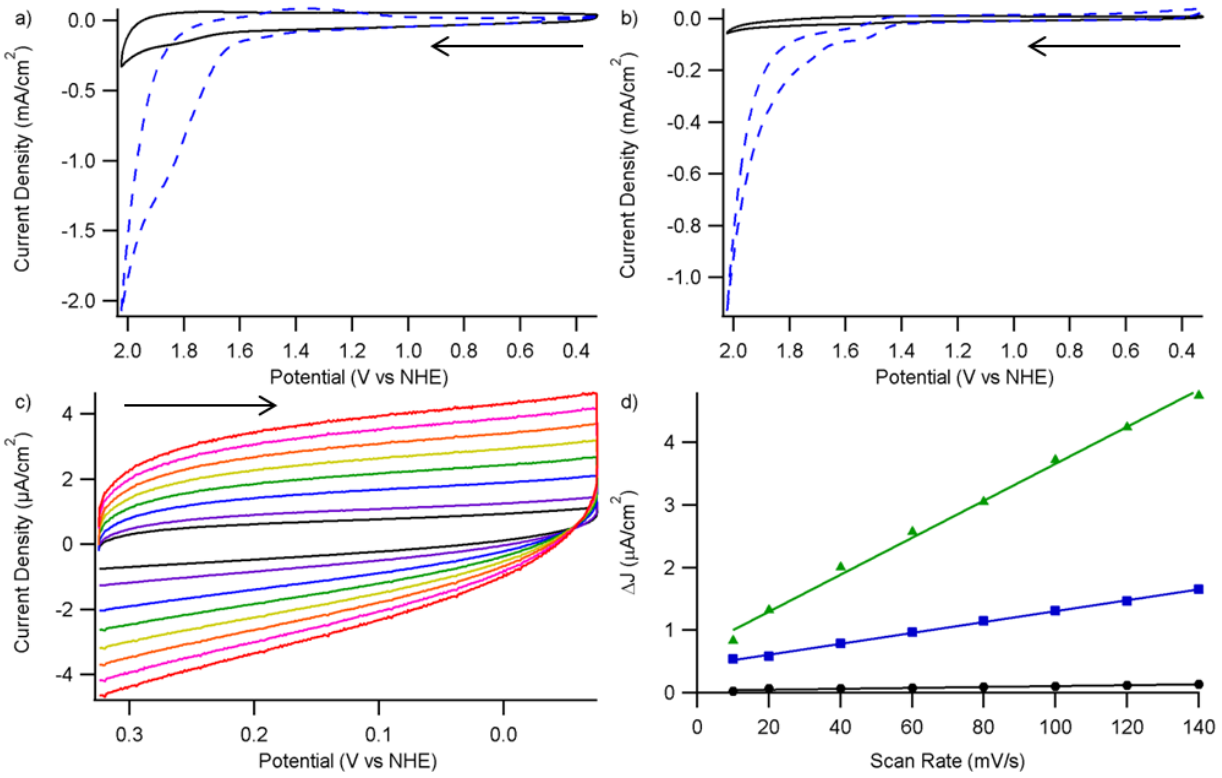

Figure 6.4 Response of NiO electrode (a) and RuO_2 electrode (b) in electrolyte (0.1 M NBu_4PF_6, MeCN) solution (black, solid) and 55 mM DHA (blue, dashed) obtained at 50 mV/s. c) CVs of RuO_2 electrode in electrolyte solution and scan rates of: 10 (black), 20 (purple), 40 (blue), 60 (green), 80 (yellow), 100 (orange), 120 (pink), and 140 (red) mV/s . d) ΔJ at 0.1 V *vs.* Scan Rate for FTO (black, circles), RuO_2 (blue, squares) and NiO (green, triangles) electrodes. The arrows indicate the potential sweep direction.

6.2.3 *Scrutinizing Response of V_2O_5 Electrodes*

Initial screening of V_2O_5 anodes revealed an interesting oxidative feature between 1.1 and 1.2 V in solutions of DHA, Figure 6.5 a. Several experiments were carried out to tell whether or not the oxidative current around 1.2 V was associated with catalytic oxidation of DHA. A series of CVs were obtained with a lower switching potential of 1.385 V. An oxidative peak initially observed at around 1.25 volts shifted to lower potentials and decreased in intensity with increasing scans. Furthermore, CPE was run in solutions of DHA at 1.225 and 1.395 V for ten minutes employing UV-visible spectroscopy to check for the presence of anthracene, of which, none was observed.

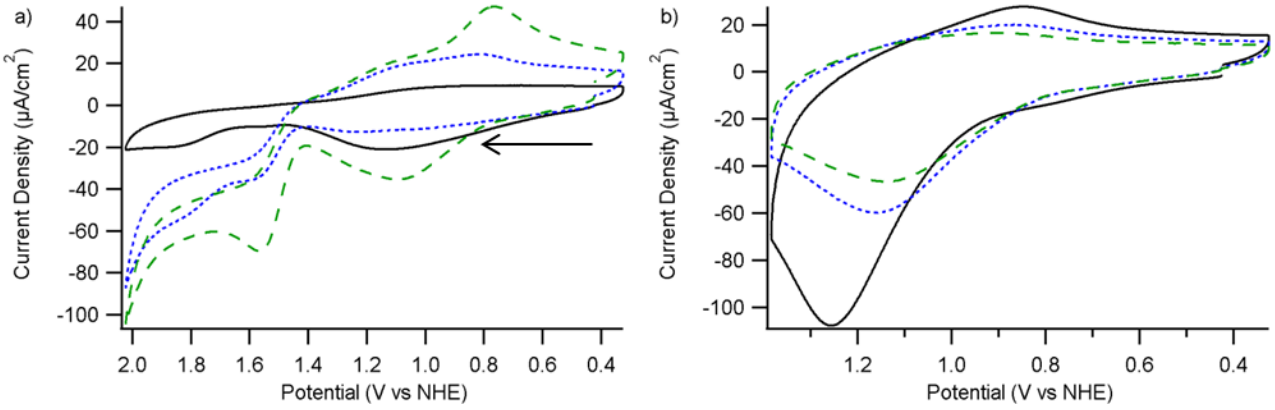

Figure 6.5 a) CVs of a V_2O_5 anode in electrolyte (0.1 M NBu_4PF_6, MeCN) solution (black, solid). The first (blue, dotted) and second (green, dashed) scans in a DHA solution. The arrow indicates the potential sweep direction (50 mV/s). b) Successive CVs obtained in DHA solution with a lower switching potential to investigate feature at 1.2 V; first (black, solid), second (blue, dotted), third (green, dashed). Note the reduction in current around 1.2 V with the second and third scans.

6.2.4 *Increasing Substrate Scope*

The alkyl substituted benzene molecules toluene, ethylbenzene, and cumene were screened for oxidation with NiO and RuO_2 anodes. CVs were collected in 55 mM solutions of each substrate by scanning out to 2.425 V. A CV obtained in a solution of ethylbenzene with an RuO_2 anode, Figure 6.6, displays a dramatic increase in oxidative current starting at about 2.1 V. All of the alkylated benzene substrates had similar behavior on both the NiO and RuO_2 anodes; oxidative current was never observed prior 2.1 V.

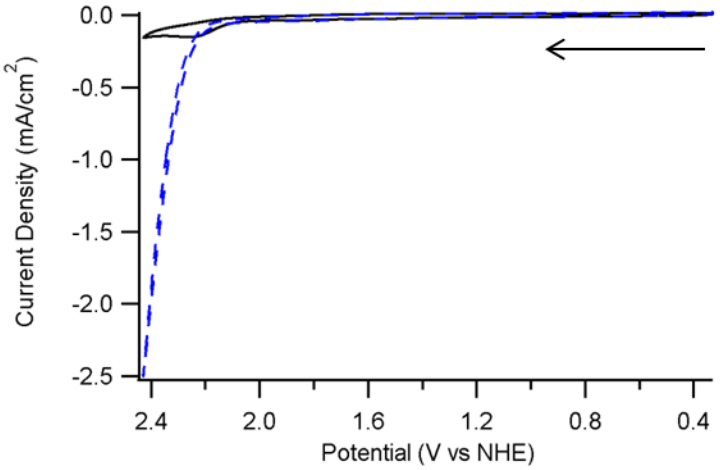

Figure 6.6. CVs showing the response of an RuO2 anode in electrolyte (0.1 M NBu_4PF_6, MeCN) solution (black, solid) and in a solution of ethylbenzene (blue, dashed). The arrow indicates the potential sweep direction (50 mV/s).

6.2.5 *Introducing External Bases*

Organic and inorganic bases were introduced to the catalyst system in an effort to achieve C–H oxidation at lower potentials. The organic base pyridine was tested first as it was soluble in the electrolyte solutions. CVs were obtained with the NiO anode in four different solutions: electrolyte, the standard DHA solution, pyridine (2.5 mM) in electrolyte, and both the DHA and the base. The CVs in the electrolyte and DHA solutions were typical of what had been previously observed, Figure 6.7a) black, solid and blue, dotted traces respectively. The pyridine solution displayed a large irreversible oxidation beginning around 1.4 V, reaching a maximum at about 1.8V, Figure 6.7a) green, dashed trace. The solution containing the combination of DHA and pyridine yielded a CV that appeared to be a superposition of the two separate components of

the mixture, Figure 6.7a) red, dot-dashed. No decrease in the oxidation onset of DHA was observed.

To test inorganic bases NiO electrodes were dipped in 0.1 M solutions of sodium carbonate, monosodium phosphate hydrate, and disodium phosphate. The electrodes were then allowed to dry for about 1 minute before CVs were obtained. The CVs from electrolyte and DHA solutions prior to base solution treatment were similar to those previously described, Figure 6.7b) black, solid and blue, dotted respectively. After treatment in the sodium carbonate solution, the CV collected in electrolyte displayed a slight increase in current over the whole scan starting from about 0.9 V, Figure 6.7b) green, dashed. The CV collected in DHA with the base treated anode had an overall decrease in current density and significant oxidation was not observed until after 1.8 V, Figure 6.7b) red, dot-dashed. Similar behavior, hindering the oxidation of DHA, was observed for the other inorganic bases screened.

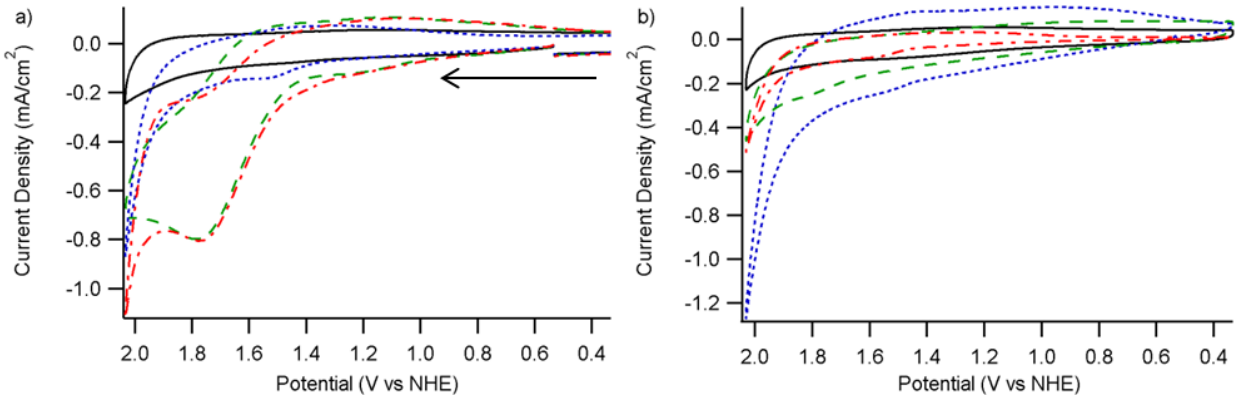

Figure 6.7 a) CVs obtained with an NiO anode in electrolyte (black, solid); DHA solution (blue, dotted); electrolyte with 2.5 mM pyridine (green, dashed); and DHA solution with 2.5 mM pyridine (red, dot-dashed). (b) CVs obtained with an untreated NiO anode in electrolyte (black, solid) and DHA solution (blue, dotted); and CVs obtained with same anode treated with sodium carbonate in electrolyte (green, dashed) and DHA solution (red, dot-dashed). The arrow in (a) indicates the potential sweep direction (50 mV/s) and the electrolyte solutions was 0.1 M NBu_4PF_6 in MeCN.

6.2.6 *Moving To Aqueous Basic Solutions*

Nickel metal and NiO anodes are known to form a $Ni(OH)_2$ phase in basic, aqueous solutions.[19] Studies by Pletcher and coworkers demonstrated that "oxide coated" nickel electrodes oxidize various simple alcohols and amines to carboxylic acids, nitrile, aldehydes and ketones under basic conditions.[7,20] The oxidation of these small molecules is attributed to the a NiO(OH) phase formed from the loss of one electron and one proton.

The coupling of proton activity to this oxidizing phase change was investigated on the NiO anodes and Nickel foil in solutions of KOH/KNO_3 ranging between pH 12 and 14. In aqueous 1.0 M KOH, at pH 14, the Ni^{2+}/Ni^{3+} couple associated with the change from $Ni(OH)_2$ to NiO(OH) was centered at 560 mV for the NiO anode, Figure 6.8a red, dot-dot-dashed. The NiO anodes consistently displayed higher current densities than the Nickel foil. The sharp increase in oxidative current starting after 0.8 V is from the oxidation of water. The Ni^{2+}/Ni^{3+} couple shifts to more positive values as the pH decreases meaning that Ni^{2+} is harder to oxidize, Figure 6.8b. The $E_{1/2}$ for the Ni^{2+}/Ni^{3+} couple shifts by -84 and -77 mV per decade for the NiO and Ni foil (not displayed) respectively.

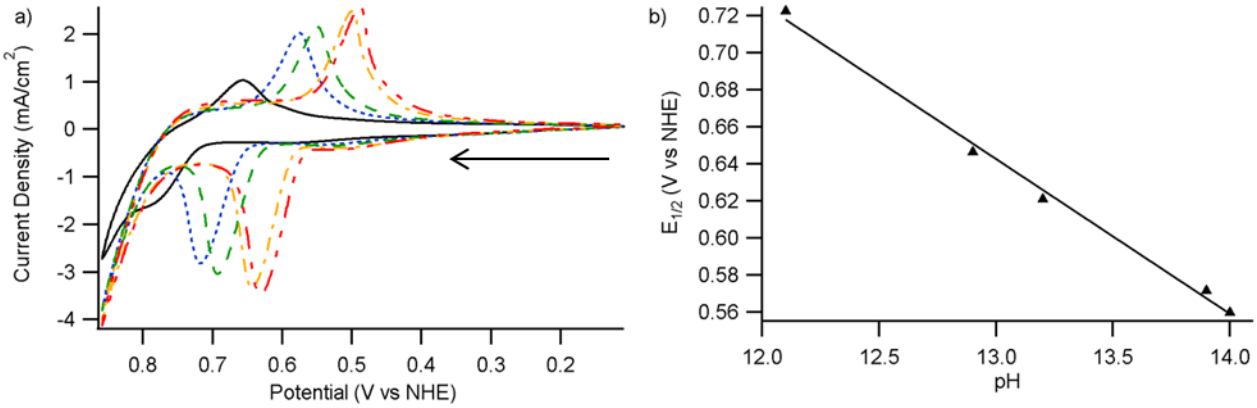

Figure 6.8. a) CVs collected with an NiO anode in basic aqueous electrolyte to track the change of the Ni^{2+}/Ni^{3+} couple with pH; 12.05 (black, solid); 12.85 (blue, dotted); 13.19 (green, dashed); 13.86 (yellow, dot-dashed); 14.00 (red; dot-dot-dashed). The arrow in (a) indicates the potential sweep direction and the scan rate was 50 mV/s. Electrolyte was kept at an ionic strength of 0.1 M with KOH and KNO_3, see section 6.4.8. b) The $E_{1/2}$ value of the Ni^{2+}/Ni^{3+} couple plotted against the pH of the solution is which it was measured.

Having demonstrated the NiO(OH) phase can be accessed with the NiO anodes, many organic substrates were screened for oxidation. As the oxidation of alcohols is well documented, CVs in 0.4 M solutions of KOH with various concentrations of ethanol were obtained, Figure 6.9a. At a concentration of 10 mM the oxidation of ethanol is observed starting around 0.7 V, after the Ni^{2+} oxidation peak. When the concentration of ethanol is 50 mM or higher the catalytic oxidation of this alcohol is observed occurring closer to the apex of the Ni^{2+} oxidation peak.

The oxidations of toluene, ethylbenzene, and cumene were attempted under the aqueous conditions. The substrates were not soluble under the conditions and the CVs obtained from 50 mM solutions nearly overlaid those obtained in electrolyte (not pictured). More soluble derivatives, *p*-toluenesulfonic acid (not pictured) and 4-isopropylbenzoic acid (Figure 6.9b) were screened for oxidation under the aqueous conditions. No oxidation of the substrates was observed, only slight shifts in the Ni^{2+}/Ni^{3+} couple. A total of seven phenylated carboxylic acids were screened for catalytic C–H oxidation. The CVs from these solutions showed slight shifts in the Ni^{2+}/Ni^{3+} couple as was observed with the previously described substrates, Figure 6.9c

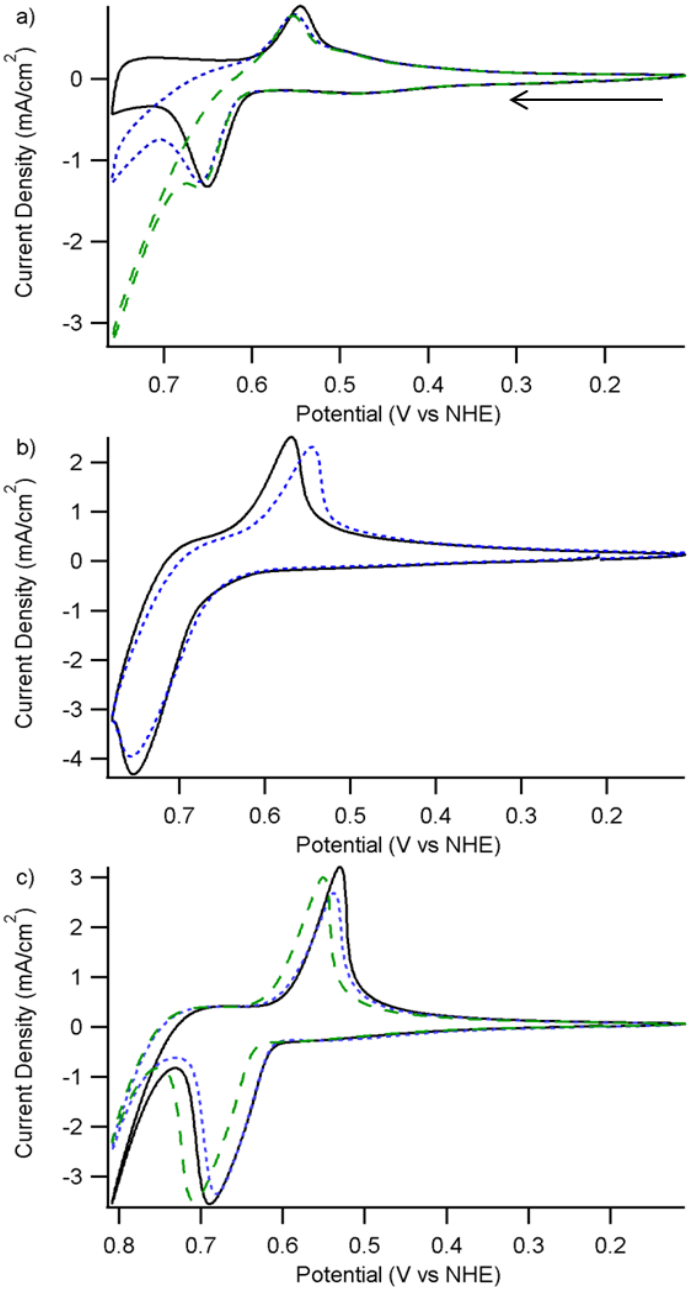

Figure 6.9 a) CVs obtained with a NiO anode in 0.4 M KOH electrolyte (black, solid), and the same electrolyte with 10 (blue, dotted) and 50(green, dashed) mM ethanol respectively. The arrow in (a) indicates the potential sweep direction (50 mV/s). b) CVs obtained with a NiO anode in 0.4 M KOH electrolyte (black, solid) and electrolyte with 50 mM 4-isopropylbenzoic acid (blue, dotted). c) CVs obtained with NiO anode in 0.4 M KOH electrolyte (black, solid) and electrolyte with 50 mM 3-phenylbutyric acid (blue, dotted) and 3-phenylglutaric acid (green, dashed) respectively.

6.3 Discussion and Conclusions

Sadly, no catalytic oxidation of saturated C–H bonds at potentials below anthracene oxidation was observed during the course of the study. A handful of the MO_x screened displayed oxidation of DHA around 1.4 V, and the CPE experiment with NiO electrodes demonstrated that the oxidation of DHA lead to the anthracene product. It is interesting to note that the FTO electrodes oxidized DHA around 1.4 V, which suggests that none of the active MOx provided a thermodynamic advantage. The oxidation of toluene, ethylbenzene, and cumene occurred around 2.2 V Literature on the electrochemistry of these molecules reports the anodic peak potentials for this series to range from 2.49 to 2.56 V, suggesting that ET from the π-system of the organic substrates is being observed, not C–H oxidation.[21]

While displaying modest current densities (100s of $\mu A/cm^2$) the only MO_x to have oxidative behavior below 1.4 V in the organic solutions was V_2O_5. As was described CV and CPE experiments confirmed that the anodic feature centered around 1.2 V was not from DHA oxidation. Close examination of the CVs in Figure 6.5b reveals a reductive feature around 0.8V. The initial feature at 1.2 V may be attributed to oxidation of V^{4+} species in the surface of the film created by oxygen non-stoichiometry; the reductive feature on the return sweep would then be associated with reducing V^{5+} states back to V^{4+}.[10]

The NiO and RuO_2 anodes had consistently higher current densities (~1 to 2.5 mA/cm^2) than the other oxidatively active materials; IrO_x, CoO_x, and $Ni_xFe_yO_z$. The experiments to probe film double layer capacitance (C_{DL}) suggest that the high current densities of the NiO anodes are due to having greater effective surface areas than the other materials. The current densities at 1.55 V from CVs of the NiO and RuO_2 anodes in DHA solutions are 132 and 83 $\mu A/cm^2$, but the NiO has an affective surface area that 3.4 times great than the RuO_2. This implies that the RuO_2 films are intrinsically more active than the NiO. It would have been interesting to measure the C_{DL} of the amorphous oxides, because they are known to form extremely thin films which may account for the low current densities observed in their CVs.

Having not observed catalytic oxidation of the DHA from the MO_x films alone, the idea that the anodes were acting as the oxidant and *the base* came into question. Previous research in our group had examined use of oxidant and bases to act as net PCET reagents,[22] and other researchers showed that this approach could be used to develop catalytic PCET systems.[23] CVs

of pyridine obtained in the absence of DHA, displayed irreversible, oxidative current starting at about 1.0 V. When the soluble organic base pyridine was introduced into an electrolyte solution containing DHA, the CV obtained was nearly a superposition of the base and the substrate. This oxidation of pyridine is not surprising as bases can be thought of as electron rich molecules.[5] In the other approach used to "add a base" to the catalytic system, NiO anodes were dipped in aqueous base solution and allowed to drip dry before CVs were obtained. The thought was that protons on the surface of the MOx would be removed, making the film more basic. The CVs obtained in DHA solution after this procedure actually had lower current densities than CVs obtained from the untreated anodes. The decrease in current is probably caused by the inorganic bases creating a blocking layer on the surface of the electrode.

In reading on oxidations with MO_x electrodes reports on the oxidation of alcohols, amines, and other small molecules with NiO under basic conditions caught our attention.[7,20] This activity was attributed to a $Ni(OH)_2$ species at the solid liquid interface going through an oxidative phase change to an NiO(OH) species. This oxidation is coupled with the loss on a proton hinting that this NiOOH phase may act an oxidant and base at the same time. Mechanistic work by Chen and Chou on the oxidation of *n*-butanol with $Ni(OH)_2$ suggested the first step in oxidation was hydrogen atom abstraction by an NiOOH species.[24]

To better understand the coupling of protons to the oxidation of $Ni(OH)_2$, CVs were obtained in basic solutions having different pH with NiO and Ni foil electrodes. Upon graphing the change in the Ni^{2+}/Ni^{3+} with pH it was determined that the NiO and Ni foil electrodes showed shifts of -84 and -77 mV per decade, Figure 6.8. These values are well above the Nernstian -59 mV/pH unit shift expected from a one electron, one proton process, but they are close to the -96 mV/pH unit slope report by Nocera for his Nickel-borate WOC.[25] A slope of -90 mv/pH unit would describe a two electron, three proton process. While this slope was unexpected, $Ni(OH)_2$ to NiO(OH) is a one electron one proton process, the shift in oxidation potential with pH demonstrated that PCET is operative in this system.

The catalytic oxidation of ethanol in 0.4 M KOH was readily observed with the NiO electrodes, Figure 6.9a. This was not too surprising as the reaction has been studied for decades,[7] particularly with the hopes of developing a direct ethanol fuel cell.[26] At 50 mM concentrations, similar to where catalytic ethanol oxidation is observed, oxidation of *p*-isopropylbenzoic acid (Scheme 6.2, left) was not observed. If one considers that in strongly basic media the benzoic

acid would be deprotonated and may bind to the NiO surface with the tertiary C–H bond facing away from the metal-oxide surface, this may explain the absence of catalytic oxidation. Using the substrate 3-phenylbutyric acid (Scheme 6.2, right) would solve the orientation issue with the tertiary C–H bond encountered with *p*-isopropylbenzoic acid, but oxidation was not observed for this substrate or others with similar structures. From a thermodynamic perspective this is somewhat surprising as the C–H bond disassociation energies (BDE) for the benzylic C–H of toluene and ethylbenzene are 90 and and 85 kcal/mol, while the BDE for α C–H of ethanol is much stronger at 96 kcal/mol.[27] As $Ni(OH)_2$ has also been known to oxidize amines, ketones, and aldehydes, the presence of non-carbon functional group may be required to "activate" the C–H bonds to observe oxidation under the given conditions.

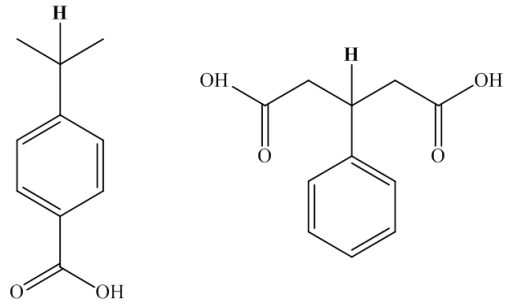

Scheme 6.2. *p*-Isopropylbenzoic acid (left) and 3-phenylbutyric acid (right). The C–H bonds to be oxidized have "H" emboldened.

6.4 EXPERIMENTAL

6.4.1 *General Considerations*

Acetonitrile (HPLC grade) was obtained from Fisher Scientific and used as received. Tetrabutylammonium hexafluorophosphate [TBA][PF_6] was obtained from Sigma-Aldrich, recrystallized three times from hot ethanol and dried overnight on a Schlenk line with mild heating (30 °C) before use. All other substrates and metal-oxide precursors were purchased from Sigma-Aldrich and used as received unless otherwise noted. Fluorine doped tin oxide coated glass slides (FTO), TEC 15 grade supplied from Sigma Aldrich, were rinsed with hexanes followed by ethanol (two times), and then sonicated in ethanol for 30 seconds before a final rinse with ethanol. All thin film electrodes were masked with epoxy so a geometric area could be determined. The geometric area was measured gravimetrically by copying the electrodes onto paper, cutting out the unmasked area and comparing the weight to a full sheet of paper.

Electronic absorption spectra were obtained using a Hewlett-Packard 8453 diode-array UV-visible spectrophotometer. Electrochemical measurements with made with a CH Instruments 650D potentiostat.

6.4.2 *Preparation of MOx Screened*

The following MO_X films were prepared with three coats of precursor, via spin-coating at 1500 rpm for 30 seconds. The precursor films were heated at 400 °C for 10 minutes and the final coat was annealed for 5 hours.

NiO– $NiCl_2$ and the F88 pluronic tri block copolymer (1g, each) were dissolved in a solution of DI water (3g) and ethanol (6g) and allowed to stir overnight. The solution was centrifuged and the supernatant was used as the solution for spin coating.

Nb_2O_5– Nb(V) ethoxide (500 mL) was dissolved in ethanol (7mL) and used for spin-coating.

Nb:NiO– $NiCl_2$, the F88 pluronic tri block copolymer (1g, each) and Nb(V)ethoxide (4.5 µL, 5% molar) were dissolved in a solution of DI water (3g) and ethanol (6g) and allowed to stir overnight. The solution was centrifuged and the supernatant was used for spin coating.

The following MO_X films were prepared with three coats of precursor, via spin coating at 2000 rpm for 30 seconds. The precursor films were heated at 400 °C for 10 minutes and the final coat was annealed for 5 hours.

CeO_2– The precursor was prepared at 0.1 M concentration by dissolving ceric ammonium nitrate (0.546 g) in ethanol (10 mL).

TiO_2– Titanium isopropoxide (400 µL) and ethanolamine (800 µL) were brought up to volume with 2-methoxyethanol in a 10 mL volumetric flask.

RuO_2– $Ru(NO)(NO_3)_3$ (0.1g) was dissolved in DI water (10 mL) to which 1 mL of an aqueous tetramethylammonium hydroxide solution (25% w/w) was added. A precipitate formed that was dissolved by vigorous shaking before spin-coating.[28]

The following MO_X films were prepared with three coats of precursor, via spin coating at 1000 rpm for 30 seconds. The precursor films were heated at 500 °C for 10 minutes and the final coat was annealed for 5 hours.

V_2O_5– Vanadyl acetylacetonate (0.95 g) was dissolved in acetylacetone (4.5 mL) and sonicated for 15 minutes before spin-coating.

$BiVO_4$– Bismuth (II) nitrate pentahydrate (0.173 G), vanadyl acetylacetonate (87 mg), tungsten trioxide monohydrate (5 mg), bis-acetylacetonato,dioxomolybdenum (VI) (7 mg), and acetic acid (0.54 mL) were dissolved in acetylacetone (4.46 mL) and sonicated before spin-coating.

The following MO_X films were prepared with three coats of precursor, via spin coating at 1500 rpm for 30 seconds. The precursor films were heated at 500 °C for 15 minutes and the final coat was annealed for 5 hours.

Lithium Nickel Cobalt Aluminum Oxide– was prepared by creating a slurry of the received material (0.5 g) in ethanol (15 mL) before spin-coating.

Lithium Manganese Nickel Cobalt Oxide– was prepared by creating a slurry of the received material (0.5 g) in ethanol (15 mL) before spin-coating.

The following MO_X films were prepared by spin-coating with the precursors followed by 3 to 5 days of illumination with near UV or 256 nm lamps.

CoO_X– Co(II)ethylhexanoate 60% m/m in mineral oil (12 mg) was diluted in hexanes (15 g).

IrO_X– Ir(III) acetylacetonate (16 mg) was dissolved in chloroform (31 g).

6.4.3 *Electrochemical Measurements in Organic Solvent*

Electrochemical measurements were obtained in acetonitrile (MeCN) solutions containing 0.1M tetrabutylammonium hexafluorophosphate (NBu_4PF_6) as the supporting electrolyte with a MO_x working electrode, a Pt auxiliary electrode, and a $Ag/AgNO_3$ reference electrode. Potentials were referenced to the Normal Hydrogen Electrode (NHE) by measuring the ferrocene/ferrocenium redox couple in solution 5 mM solution and adjusting the potentials offsets by +0.536 V as described by a literature method.[29] The MO_x anodes were screened by obtaining cyclic voltammograms (CV) at 50 mV/s in a potential window between 0.325 and 2.025 V. A 55 M substrate concentration was used unless otherwise noted. The alkyl benzene substrates were screened in a wider potential window, from 0.325V to 2.43 V. The substrate solutions were prepared from stocks of the [TBA][PF_6] (3.87g, 100 mL, 0.1 M) acetonitrile solutions in 10 mL volumetric flasks.

Table 6.8. Organic Substrate Solutions

Substrate	Mass (mg)	Volume (µL)
9,10-dihydroanthraecene	100	N/A
Anthracene (3 mM)	7	N/A
Toluene	0.050	58.2
Ethylbenzene	0.058	67.4
Cumene	0.066	76.7

CVs of the epoxy masked MO_x samples were obtained in electrolyte for a reference or background current before measurements were obtained in the substrate solutions.

6.4.4 *Controlled Potential Electrolysis of DHA with NiO electrode*

A 0.11 M solution of DHA (500 mg) was prepared in a 25 mL volumetric flask. A UV-visible spectrum was obtained by diluting 200 µL of this solution to 2.6 mL with acetonitrile in a quartz cuvette. An "H-Cell" was prepared by adding 10 mL of the solution on each side placing the NiO working electrode Ag/Ag^+ reference electrode and in one compartment and isolating the Pt counter electrode on the other. Cyclic voltammograms were obtained before and after electrolysis by sweeping in the anodic direction between 2.025 V and 0.225 V starting and ending at 0.0 V at a scan rate of 50 mV/s. CPE was run for 15 minutes at a potential of 1.72 V. Another UV-visible spectrum was obtained as described before by diluting the electrolytic solution subjected to CPE.

6.4.5 *Comparing Top Performing MOx in Organic Solutions*

CVs of various FTO, RuO_x, and NiO anodes were obtained in electrolytic solutions of DHA. The anodes of each MOx displaying the highest current density at 1.8 V were subjected to series of electrochemical measurements to determine the double-layer capacitance (C_{DL}) of the films, which provides an estimate of the solid electrolyte interface area.[18,30] CVs were obtained by sweeping the potential in the negative direction from 0.325 to -0.075 V and then to the initial potential. This was performed at 10, 20, 40, 60, 80, 100, 120, and 140 mV/s for each of the chosen anodes. The difference in current (ΔJ) was obtained by subtracting the anodic current density from the cathodic current density at 0.1 V and plotted against the scan rate for each of the chosen anodes. Half of the slope of the line obtained from the aforementioned plots gave the C_{DL}

of the anodes, which were 0.35, 4.35, and 14.75 μF/cm^2 for the FTO, RuO_x, and NiO films respectively.

6.4.6 *Exploring Behavior of V_2O_5 Films*

Two V_2O_5 anodes were screened in the normal CV range and the one displaying higher current densities at ~1.25V was chosen for further tests. Four consecutive CVs were obtained between 0.325 and 1.3825 volts at a scan rate of 50 mV/s. CPE was run for 10 minutes at a potential of 1.225 V and UV-visible spectra were obtained as described in section 1.5.4.

6.4.7 *Introducing External Bases*

Three solutions were prepared in 10 mL volumetric flasks from 0.1 M electrolyte to test how the introduction of an external base would influence the oxidation of DHA over NiO an electrode. The first solution was 55 mM DHA, the second contained pyridine (2 μL, 2.5 mM) and the third contained DHA and pyridine at the 55 and 2.5 mM concentrations respectively. CVs were obtained by sweeping in the oxidative direction from 0.535 to 2.035 V, sweeping in the reductive direction to -1.065 V, and returning to 0.535 V at 50 mV/s. CVs were obtained in the electrolyte followed by the DHA, pyridine, and substrate/base combination solutions.

Basic buffer solutions (0.1 M) of sodium carbonate (106 mg), monosodium phosphate hydrate (138 mg), and disodium phosphate (142 mg) were prepared in 10 mL volumetric flasks with deionized water. With an NiO electrode, three CVs were obtained in solutions of electrolyte and 55 mM DHA. The electrode was then submerged into one of the aqueous buffer solutions, drip-dried for no more than one minute and three CVs were obtained in the electrolyte. The submersion, drip-dry, and CV obtaining process was repeated for the DHA solution with all of the buffers.

6.4.8 *NiO Under Basic Aqueous Conditions*

Electrochemical measurements were obtained in aqueous solutions of 0.4 M potassium hydroxide (KOH) prepared in 50 mL volumetric flasks from 1.12g KOH and 18MΩ water. Measurements were made in a three electrode cell with an MO_x working electrode, a platinum counter electrode and a Ag/AgCl reference electrode. All measurements were referenced to NHE by adding 209 mV to the measured potential. CVs were obtained between 0.209 and 0.759 or 0.8

V vs NHE at 50 mV/s. Several organic substrates were screened under these conditions and were prepared in 10 mL volumetric flasks with the 0.4 M aqueous KOH electrolyte as outlined in the table below.

Table 6.9. Aqueous Substrate Solutions

Substrate	Mass (mg)	Volume (μL)	Concentration (M)
Ethanol	0.005	5.8	0.01
Ethanol	0.023	29	0.05
Toluene	0.046	53	0.05
Ethylbenzene	0.053	61	0.05
Cumene	0.060	70	0.05
p-Toluenesulfonic acid	190	N/A	0.10
4-Isopropylbenzoic acid	84	N/A	0.05
Diphenylacetic acid	318	N/A	0.15
2-Phenylpropionic acid	225	205	0.15
2,2-Diphenylpropionic acid	339	N/A	0.15
3,3-Diphenylpropionic acid	339	N/A	0.15
3-Phenylbutryic acid	246	N/A	0.15
α-Phenyl-*o*-toluic acid	318	N/A	0.15
3-Phenylglutaric acid	312	N/A	0.15

The pH dependence of the Ni^{2+}/Ni^{3+} couple was explored with NiO and Ni foil electrodes. Stock solutions (1.0 M) of KOH and potassium nitrate (KNO_3) were prepared in 50 mL volumetric flasks using 2.76 and 5.05 g of the respective salts with 18 MΩ water. In order to maintain the ionic strength of 1.0 M while varying the pH, five solutions were prepared from the stocks in 10 mL volumetric flasks as outlined in the table below Electrochemical data was collected after running a 30 second pre-electrolysis at 0.729 V after which CVs were taken by sweeping from 0.209 to 0.859 V reversing to 0.109 V and returning to 0.209 V. The pH of each solution was measured before and after the CVs were obtained.

Table 6.10. Solutions to track $\Delta Ni^{2+}/Ni^{3+}$ with pH

Solution	KOH Sol. (mL)	KNO_3 Sol (mL)	pH
1	10	0	14.00
2	6.25	3.75	13.88
3	1.25	8.75	13.19
4	0.625	9.375	12.85
4	0.125	9.875	12.05

6.5 NOTES

(1) Burrows, B. *J. Chem. Educ.* **1971**, *48* (11), 732.

(2) Winter, M.; Brodd, R. J. *Chem. Rev.* **2004**, *104* (10), 4245–4270.

(3) Schrauben, J. N.; Hayoun, R.; Valdez, C. N.; Braten, M.; Fridley, L.; Mayer, J. M. *Science* **2012**, *336* (6086), 1298–1301.

(4) Silverstein, R. M. *Spectrometric Identification of Organic Compounds*; Wiley, 1991.

(5) Warren, J. J.; Tronic, T. A.; Mayer, J. M. *Chem. Rev.* **2010**, *110* (12), 6961–7001.

(6) Khan, S. U. M.; Akikusa, J. *J. Phys. Chem. B* **1999**, *103* (34), 7184–7189.

(7) Fleischmann, M.; Korinek, K.; Pletcher, D. *J. Electroanal. Chem. Interfacial Electrochem.* **1971**, *31* (1), 39–49.

(8) Bediako, D. K.; Surendranath, Y.; Nocera, D. G. *J. Am. Chem. Soc.* **2013**, *135* (9), 3662–3674.

(9) Murray, E. P.; Tsai, T.; Barnett, S. A. *Nature* **1999**, *400* (6745), 649–651.

(10) Lee, B.; Hibino, T. *J. Catal.* **2011**, *279* (2), 233–240.

(11) Jirkovský, J. S.; Busch, M.; Ahlberg, E.; Panas, I.; Krtil, P. *J. Am. Chem. Soc.* **2011**, *133* (15), 5882–5892.

(12) Croy, J. R.; Gallagher, K. G.; Balasubramanian, M.; Chen, Z.; Ren, Y.; Kim, D.; Kang, S.-H.; Dees, D. W.; Thackeray, M. M. *J. Phys. Chem. C* **2013**, *117* (13), 6525–6536.

(13) Smith, R. D. L.; Sporinova, B.; Fagan, R. D.; Trudel, S.; Berlinguette, C. P. *Chem. Mater.* **2014**, *26* (4), 1654–1659.

(14) Smith, R. D. L.; Prévot, M. S.; Fagan, R. D.; Zhang, Z.; Sedach, P. A.; Siu, M. K. J.; Trudel, S.; Berlinguette, C. P. *Science* **2013**, *340* (6128), 60–63.

(15) Trotochaud, L.; Ranney, J. K.; Williams, K. N.; Boettcher, S. W. *J. Am. Chem. Soc.* **2012**, *134* (41), 17253–17261.

(16) McFarland, E. W.; Metiu, H. *Chem. Rev.* **2013**, *113* (6), 4391–4427.

(17) Visscher, W.; Barendrecht, E. *Electrochimica Acta* **1980**, *25* (5), 651–655.

(18) Merki, D.; Vrubel, H.; Rovelli, L.; Fierro, S.; Hu, X. *Chem. Sci.* **2012**, *3* (8), 2515–2525.

(19) Beverskog, B.; Puigdomenech, I. *Corros. Sci.* **1997**, *39* (5), 969–980.

(20) Fleischmann, M.; Korinek, K.; Pletcher, D. *J. Chem. Soc. Perkin Trans. 2* **1972**, No. 10, 1396–1403.

(21) Howell, J. O.; Goncalves, J. M.; Amatore, C.; Klasinc, L.; Wightman, R. M.; Kochi, J. K. *J. Am. Chem. Soc.* **1984**, *106* (14), 3968–3976.

(22) Waidmann, C. R.; Miller, A. J. M.; Ng, C.-W. A.; Scheuermann, M. L.; Porter, T. R.; Tronic, T. A.; Mayer, J. M. *Energy Environ. Sci.* **2012**, *5* (7), 7771–7780.

(23) Tarantino, K. T.; Liu, P.; Knowles, R. R. *J. Am. Chem. Soc.* **2013**, *135* (27), 10022–10025.

(24) Chen, Y.-L.; Chou, T.-C. *Ind. Eng. Chem. Res.* **1996**, *35* (7), 2172–2176.

(25) Dincă, M.; Surendranath, Y.; Nocera, D. G. *Proc. Natl. Acad. Sci.* **2010**, *107* (23), 10337–10341.

(26) Kim, J.-W.; Park, S.-M. *J. Korean Electrochem. Soc.* **2005**, *8* (3), 117–124.

(27) Luo, Y.-R. *Comprehensive handbook of chemical bond energies*; CRC press, 2007.

(28) Musić, S.; Popović, S.; Maljković, M.; Furić, K.; Gajović, A. *Mater. Lett.* **2002**, *56* (5), 806–811.

(29) Pavlishchuk, V. V.; Addison, A. W. *Inorganica Chim. Acta* **2000**, *298* (1), 97–102.

(30) Gileadi, E. *Physical Electrochemistry*; Wiley-VCH: Weinheim, 2011.

BIBLIOGRAPHY

Acharya, K. P.; Khnayzer, R. S.; O'Connor, T.; Diederich, G.; Kirsanova, M.; Klinkova, A.; Roth, D.; Kinder, E.; Imboden, M.; Zamkov, M. *Nano Lett.* **2011**, *11* (7), 2919–2926.

Adams, D. M.; Brus, L.; Chidsey, C. E. D.; Creager, S.; Creutz, C.; Kagan, C. R.; Kamat, P. V.; Lieberman, M.; Lindsay, S.; Marcus, R. A.; Metzger, R. M.; Michel-Beyerle, M. E.; Miller, J. R.; Newton, M. D.; Rolison, D. R.; Sankey, O.; Schanze, K. S.; Yardley, J.; Zhu, X. *J. Phys. Chem. B* **2003**, *107* (28), 6668–6697.

Anderson, N. A.; Lian, T. *Annu. Rev. Phys. Chem.* **2005**, *56* (1), 491–519.

Ardo, S.; Meyer, G. J. *Chem. Soc. Rev.* **2008**, *38* (1), 115–164.

Bae, Y.; Myung, N.; Bard, A. J. *Nano Lett.* **2004**, *4* (6), 1153–1161.

Bahnemann, D. W.; Kormann, C.; Hoffmann, M. R. *J. Phys. Chem.* **1987**, *91* (14), 3789–3798.

Bard, A. J. *J. Am. Chem. Soc.* **2010**, *132* (22), 7559–7567.

Bediako, D. K.; Surendranath, Y.; Nocera, D. G. *J. Am. Chem. Soc.* **2013**, *135* (9), 3662–3674.

Berger, T.; Monllor-Satoca, D.; Jankulovska, M.; Lana-Villarreal, T.; Gómez, R. *ChemPhysChem* **2012**, *13* (12), 2824–2875.

Beverskog, B.; Puigdomenech, I. *Corros. Sci.* **1997**, *39* (5), 969–980.

Boschloo, G.; Fitzmaurice, D. *J. Phys. Chem. B* **1999**, *103* (37), 7860–7868.

Braten, M.N.; Gamelin, D. R.; Mayer, J. M. *ACSNano.* **2015**, *9* (10), 10258-10267.

Brus, L. E. *J. Chem. Phys.* **1983**, *79* (11), 5566–5571.

Brus, L. E. *J. Chem. Phys.* **1984**, *80* (9), 4403–4409.

Brus, L. *J. Phys. Chem.* **1986**, *90* (12), 2555–2560.

Burrows, B. *J. Chem. Educ.* **1971**, *48* (11), 732.

Chen, Y.-L.; Chou, T.-C. *Ind. Eng. Chem. Res.* **1996**, *35* (7), 2172–2176.

Chianella, C.; Palombari, R.; Petricca, A. *Electrochimica Acta* **2006**, *52* (1), 369–372.

Cohn, A. W.; Janßen, N.; Mayer, J. M.; Gamelin, D. R. *J. Phys. Chem. C* **2012**, *116* (38), 20633–20642.

Costentin, C.; Evans, D. H.; Robert, M.; Savéant, J.-M.; Singh, P. S. *J. Am. Chem. Soc.* **2005**, *127* (36), 12490–12491.

Cox, S. F. J.; Davis, E. A.; Cottrell, S. P.; King, P. J. C.; Lord, J. S.; Gil, J. M.; Alberto, H. V.;

Vilão, R. C.; Piroto Duarte, J.; Ayres de Campos, N.; Weidinger, A.; Lichti, R. L.; Irvine, S. J. C. *Phys. Rev. Lett.* **2001**, *86* (12), 2601–2604.

Croy, J. R.; Gallagher, K. G.; Balasubramanian, M.; Chen, Z.; Ren, Y.; Kim, D.; Kang, S.-H.; Dees, D. W.; Thackeray, M. M. *J. Phys. Chem. C* **2013**, *117* (13), 6525–6536.

Dincă, M.; Surendranath, Y.; Nocera, D. G. *Proc. Natl. Acad. Sci.* **2010**, *107* (23), 10337–10341.

Eckermann, A. L.; Feld, D. J.; Shaw, J. A.; Meade, T. J. *Coord. Chem. Rev*. **2010**, *254* (15-16), 1769–1802.

Electroanalytical chemistry; a series of advances.; Bard, A. J., Rubinstein, I., Eds.; Boca Raton, FL CRC Press, Taylor & Francis Group, 1996; Vol. 19.

Electrochemistry at Semiconductor and Oxidized Metal Electrodes | S.R. Morrison | Springer.

Fleischmann, M.; Korinek, K.; Pletcher, D. *J. Chem. Soc. Perkin Trans. 2* **1972**, No. 10, 1396–1403.

Fleischmann, M.; Korinek, K.; Pletcher, D. *J. Electroanal. Chem. Interfacial Electrochem.* **1971**, *31* (1), 39–49.

Gambardella, A. A.; Feldberg, S. W.; Murray, R. W. *J. Am. Chem. Soc.* **2012**, *134* (13), 5774–5777.

Gaponik, N.; Poznyak, S. K.; Osipovich, N. P.; Shavel, A.; Eychmüller, A. *Microchim. Acta* **2008**, *160* (3), 327–334.

Gileadi, E. *Physical Electrochemistry*; Wiley-VCH: Weinheim, 2011.

Grauer, D. C.; Alivisatos, A. P. *Langmuir* **2014**, *30* (9), 2325–2328.

Guillemin, J.-C.; Denis, J.-M. *Tetrahedron* **1988**, *44* (14), 4431–4446.

Haase, M.; Weller, H.; Henglein, A. *J. Phys. Chem.* **1988**, *92* (2), 482–487.

Hagfeldt, A.; Boschloo, G.; Sun, L.; Kloo, L.; Pettersson, H. *Chem. Rev.* **2010**, *110* (11), 6595–6663.

Hagfeldt, A.; Graetzel, M. *Chem. Rev.* **1995**, *95* (1), 49–68.

Hamann, T. W.; Gstrein, F.; Brunschwig, B. S.; Lewis, N. S. *Chem. Phys.* **2006**, *326* (1), 15–23.

Hamann, T. W.; Gstrein, F.; Brunschwig, B. S.; Lewis, N. S. *J. Am. Chem. Soc.* **2005**, *127* (21), 7815–7824.

Hassan, J. J.; Mahdi, M. A.; Yusof, Y.; Abu-Hassan, H.; Hassan, Z.; Al-Attar, H. A.;

Monkman, A. P. *Opt. Mater.* **2013**, *35* (5), 1035–1041.

Hayoun, R. Studies of Metal Oxides in Organic Redox Reactions: Zinc Oxide Nanoparticles as Chemical Reductants In Electron Transfer and Hydrogen Atom Transfer Reactions and the Use of Osmium Tetroxide to Oxidize Higher Alkanes. Dissertation, University of Washington: Seattle Washington, 2011.

Hayoun, R.; Whitaker, K. M.; Gamelin, D. R.; Mayer, J. M. *J. Am. Chem. Soc.* **2011**, *133* (12), 4228–4231.

Howell, J. O.; Goncalves, J. M.; Amatore, C.; Klasinc, L.; Wightman, R. M.; Kochi, J. K. *J. Am. Chem. Soc.* **1984**, *106* (14), 3968–3976.

Hoyer, P.; Weller, H. *Chem. Phys. Lett.* **1994**, *221* (5–6), 379–384.

Hoyer, P.; Weller, H. *J. Phys. Chem.* **1995**, *99* (38), 14096–14100.

Huss, A. S.; Bierbaum, A.; Chitta, R.; Ceckanowicz, D. J.; Mann, K. R.; Gladfelter, W. L.; Blank, D. A. *J. Am. Chem. Soc.* **2010**, *132* (40), 13963–13965.

Ip, K.; Overberg, M. E.; Heo, Y. W.; Norton, D. P.; Pearton, S. J.; Stutz, C. E.; Luo, B.; Ren, F.; Look, D. C.; Zavada, J. M. *Appl. Phys. Lett.* **2003**, *82* (3), 385–387.

Janotti, A.; Walle, C. G. V. de. *Rep. Prog. Phys.* **2009**, *72* (12), 126501.

Jiao, F.; Frei, H. *Energy Environ. Sci.* **2010**, *3* (8), 1018.

Jirkovský, J. S.; Busch, M.; Ahlberg, E.; Panas, I.; Krtil, P. *J. Am. Chem. Soc.* **2011**, *133* (15), 5882–5892.

Kamat, P. V.; Patrick, B. *J. Phys. Chem.* **1992**, *96* (16), 6829–6834.

Khan, S. U. M.; Akikusa, J. *J. Phys. Chem. B* **1999**, *103* (34), 7184–7189.

Kim, J.-W.; Park, S.-M. *J. Korean Electrochem. Soc.* **2005**, *8* (3), 117–124.

Knowles, K. E.; Frederick, M. T.; Tice, D. B.; Morris-Cohen, A. J.; Weiss, E. A. *J. Phys. Chem. Lett.* **2012**, *3* (1), 18–26.

Knowles, K. E.; Malicki, M.; Weiss, E. A. *J. Am. Chem. Soc.* **2012**, *134* (30), 12470–12473.

Knowles, K. E.; Tagliazucchi, M.; Malicki, M.; Swenson, N. K.; Weiss, E. A. *J. Phys. Chem. C* **2013**, *117* (30), 15849–15857.

Koch, U.; Fojtik, A.; Weller, H.; Henglein, A. *Chem. Phys. Lett.* **1985**, *122* (5), 507–510.

Kohiki, S.; Nishitani, M.; Wada, T.; Hirao, T. *Appl. Phys. Lett.* **1994**, *64* (21), 2876–2878.

Koval, C. A.; Howard, J. N. *Chem. Rev.* **1992**, *92* (3), 411–433.

Krishtalik, L. I. *Biochim. Biophys. Acta BBA - Bioenerg.* **2000**, *1458* (1), 6–27.

Kumar, B.; Llorente, M.; Froehlich, J.; Dang, T.; Sathrum, A.; Kubiak, C. P. *Annu. Rev. Phys. Chem.* **2012**, *63* (1), 541–569.

Lavrov, E. V.; Herklotz, F.; Weber, J. *Phys. Rev. B* **2009**, *79* (16), 165210.

Lee, B.; Hibino, T. *J. Catal.* **2011**, *279* (2), 233–240.

Lemon, B. I.; Hupp, J. T. *J. Phys. Chem. B* **1997**, *101* (14), 2426–2429.

Liu, G.; Yu, J. C.; Lu, G. Q. (Max); Cheng, H.-M. *Chem. Commun.* **2011**, *47* (24), 6763–6783.

Liu, W. K.; Whitaker, K. M.; Kittilstved, K. R.; Gamelin, D. R. *J. Am. Chem. Soc.* **2006**, *128* (12), 3910–3911.

Liu, W. K.; Whitaker, K. M.; Smith, A. L.; Kittilstved, K. R.; Robinson, B. H.; Gamelin, D. R. *Phys. Rev. Lett.* **2007**, *98* (18).

Look, J. L.; Wick, D. D.; Mayer, J. M.; Goldberg, K. I. *Inorg. Chem.* **2009**, *48* (4), 1356–1369.

Love, J. C.; Estroff, L. A.; Kriebel, J. K.; Nuzzo, R. G.; Whitesides, G. M. *Chem. Rev.* **2005**, *105* (4), 1103–1170.

Luo, Y.-R. *Comprehensive handbook of chemical bond energies*; CRC press, 2007.

Lyon, L. A.; Hupp, J. T. *J. Phys. Chem. B* **1999**, *103* (22), 4623–4628.

Malicki, M.; E. Knowles, K.; A. Weiss, E. *Chem. Commun.* **2013**, *49* (39), 4400–4402.

Manner, V. W.; Markle, T. F.; Freudenthal, J. H.; Roth, J. P.; Mayer, J. M. *Chem Commun* **2008**, No. 2, 256–258.

Marcel. Pourbaix. *Atlas of electrochemical equilibria in aqueous solutions*, [1st English ed.].; Oxford, New York, Pergamon Press, 1966.

Materials and Processes for Solar Fuel Production; Viswanathan, B., Subramanian, V., Lee, J. S., Eds.; Nanostructure Science and Technology; Springer New York: New York, NY, 2014; Vol. 174.

Mayer, J. M. *Acc. Chem. Res.* **2011**, *44* (1), 36–46.

Mayer, J. M. *J. Phys. Chem. Lett.* **2011**, *2* (12), 1481–1489.

McFarland, E. W.; Metiu, H. *Chem. Rev.* **2013**, *113* (6), 4391–4427.

Merki, D.; Vrubel, H.; Rovelli, L.; Fierro, S.; Hu, X. *Chem. Sci.* **2012**, *3* (8), 2515–2525.

Meulenkamp, E. A. *J. Phys. Chem. B* **1998**, *102* (29), 5566–5572.

Mohamed, H. H.; Mendive, C. B.; Dillert, R.; Bahnemann, D. W. *J. Phys. Chem. A* **2011**, *115* (11), 2139–2147.

Morris-Cohen, A. J.; Donakowski, M. D.; Knowles, K. E.; Weiss, E. A. *J. Phys. Chem. C*

2010, *114* (2), 897–906.

Murray, E. P.; Tsai, T.; Barnett, S. A. *Nature* **1999**, *400* (6745), 649–651.

Musić, S.; Popović, S.; Maljković, M.; Furić, K.; Gajović, A. *Mater. Lett.* **2002**, *56* (5), 806–811.

Nickel, N. H. *Phys. Rev. B* **2006**, *73* (19), 195204.

Norberg, N. S.; Gamelin, D. R. *J. Phys. Chem. B* **2005**, *109* (44), 20810–20816.

Nozik, A. J. *Annu. Rev. Phys. Chem.* **1978**, *29* (1), 189–222.

Pavlishchuk, V. V.; Addison, A. W. *Inorganica Chim. Acta* **2000**, *298* (1), 97–102.

Pesika, N. S.; Stebe, K. J.; Searson, P. C. *J. Phys. Chem. B* **2003**, *107* (38), 10412–10415.

Poznyak, S. K.; Osipovich, N. P.; Shavel, A.; Talapin, D. V.; Gao, M.; Eychmüller, A.; Gaponik, N. *J. Phys. Chem. B* **2005**, *109* (3), 1094–1100.

Redmond, G.; O'Keeffe, A.; Burgess, C.; MacHale, C.; Fitzmaurice, D. *J. Phys. Chem.* **1993**, *97* (42), 11081–11086.

Roest, A. L.; Germeau, A.; Kelly, J. J.; Vanmaekelbergh, D.; Allan, G.; Meulenkamp, E. A. *ChemPhysChem* **2003**, *4* (9), 959–966.

Roest, A. L.; Kelly, J. J.; Vanmaekelbergh, D.; Meulenkamp, E. A. *Phys. Rev. Lett.* **2002**, *89* (3).

Schimpf, A. M.; Thakkar, N.; Gunthardt, C. E.; Masiello, D. J.; Gamelin, D. R. *ACS Nano* **2014**, *8* (1), 1065–1072.

Schrauben, J. N.; Hayoun, R.; Valdez, C. N.; Braten, M.; Fridley, L.; Mayer, J. M. *Science* **2012**, *336* (6086), 1298–1301.

Shi, G. A.; Stavola, M.; Pearton, S. J.; Thieme, M.; Lavrov, E. V.; Weber, J. *Phys. Rev. B* **2005**, *72* (19), 195211.

Shim, M.; Guyot-Sionnest, P. *J. Am. Chem. Soc.* **2001**, *123* (47), 11651–11654.

Schwartz, D. A.; Norberg, N. S.; Nguyen, Q. P.; Parker, J. M.; Gamelin, D. R. *J. Am. Chem. Soc.* **2003**, *125* (43), 13205–13218

Silverstein, R. M. *Spectrometric Identification of Organic Compounds*; Wiley, 1991.

Smith, R. D. L.; Prévot, M. S.; Fagan, R. D.; Zhang, Z.; Sedach, P. A.; Siu, M. K. J.; Trudel, S.; Berlinguette, C. P. *Science* **2013**, *340* (6128), 60–63.

Smith, R. D. L.; Sporinova, B.; Fagan, R. D.; Trudel, S.; Berlinguette, C. P. *Chem. Mater.* **2014**, *26* (4), 1654–1659.

Steele, B. C. H.; Middleton, P. H.; Rudkin, R. A. *Solid State Ion.* **1990**, *40–41, Part 1*, 388–393.

Steigerwald, M. L.; Goddard, W. A.; Evans, D. A. *J. Am. Chem. Soc.* **1979**, *101* (8), 1994–1997.

Stockwell, D.; Yang, Y.; Huang, J.; Anfuso, C.; Huang, Z.; Lian, T. *J. Phys. Chem. C* **2010**, *114* (14), 6560–6566.

Tarantino, K. T.; Liu, P.; Knowles, R. R. *J. Am. Chem. Soc.* **2013**, *135* (27), 10022–10025.

Trotochaud, L.; Ranney, J. K.; Williams, K. N.; Boettcher, S. W. *J. Am. Chem. Soc.* **2012**, *134* (41), 17253–17261.

Valdez, C. N.; Braten, M.; Soria, A.; Gamelin, D. R.; Mayer, J. M. *J. Am. Chem. Soc.* **2013**, *135* (23), 8492–8495.

Valdez, C. N.; Schimpf, A. M.; Gamelin, D. R.; Mayer, J. M. *ACS Nano* **2014**, *8* (9), 9463–9470.

van de Krol, R.; Liang, Y.; Schoonman, J. *J. Mater. Chem.* **2008**, *18* (20), 2311.

Van de Walle, C. G. *Phys. Rev. Lett.* **2000**, *85* (5), 1012–1015.

Visscher, W.; Barendrecht, E. *Electrochimica Acta* **1980**, *25* (5), 651–655.

Vohs, J. M.; Barteau, M. A. *Surf. Sci.* **1989**, *221* (3), 590–608.

Waidmann, C. R.; Miller, A. J. M.; Ng, C.-W. A.; Scheuermann, M. L.; Porter, T. R.; Tronic, T. A.; Mayer, J. M. *Energy Environ. Sci.* **2012**, *5* (7), 7771–7780.

Walczak, M. M.; Popenoe, D. D.; Deinhammer, R. S.; Lamp, B. D.; Chung, C.; Porter, M. D. *Langmuir* **1991**, *7* (11), 2687–2693.

Walter, M. G.; Warren, E. L.; McKone, J. R.; Boettcher, S. W.; Mi, Q.; Santori, E. A.; Lewis, N. S. *Chem. Rev.* **2010**, *110* (11), 6446–6473.

Wang, F.; Tang, R.; Kao, J. L.-F.; Dingman, S. D.; Buhro, W. E. *J. Am. Chem. Soc.* **2009**, *131* (13), 4983–4994

Warren, J. J.; Tronic, T. A.; Mayer, J. M. *Chem. Rev.* **2010**, *110* (12), 6961–7001.

Whitaker, K. M.; Ochsenbein, S. T.; Polinger, V. Z.; Gamelin, D. R. *J. Phys. Chem. C* **2008**, *112* (37), 14331–14335.

Widrig, C. A.; Chung, C.; Porter, M. D. *J. Electroanal. Chem. Interfacial Electrochem.* **1991**, *310* (1-2), 335–359.

Willis, R. L.; Olson, C.; O'Regan, B.; Lutz, T.; Nelson, J.; Durrant, J. R. *J. Phys. Chem. B*

2002, *106* (31), 7605–7613.

Winter, M.; Brodd, R. J. *Chem. Rev.* **2004**, *104* (10), 4245–4270.

Wong, N. Z.; Ogata, A. F.; Wustholz, K. L. *J. Phys. Chem. C* **2013**, *117* (41), 21075–21085.

APPENDIX A

The kinetic traces were fit with both double exponential (Equation A.1) and stretched exponential (Equation A.2) functions. The fits to the double exponential function were poor, but the lifetimes (or rate constants) were always roughly an order of magnitude apart, see Figure A.1. While the stretched exponential functions fit the data slightly better, interpreting the changes in the lifetimes and beta values into a kinetic model is not trivial.

$$f(x) = y_0 + X_1 e^{\{\frac{-(x - x_0)}{\tau_1}\}} + X_2 e^{\{\frac{-(x - x_0)}{\tau_2}\}} \quad \text{A.1}$$

$$f(x) = X \cdot e^{(\frac{-x}{\tau})^{\beta}} \quad \text{A.2}$$

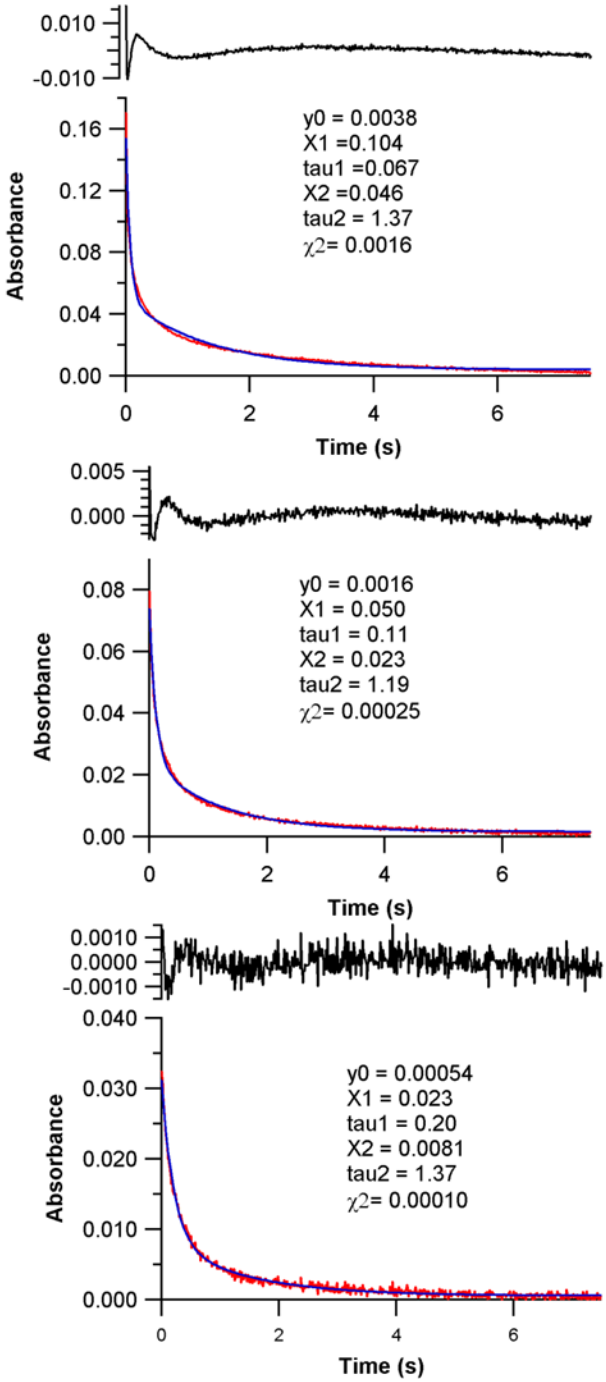

Figure A.10. Kinetic traces at 700 nm (red) for reaction of TEMPO, 4.8 mM with photo reduced ZnO NCs of different electron concentration 0.35 mM (top), 0.13 mM (middle), and 0.049 mM (bottom). The fits of data to a double exponential function (blue), Equation A-1. Associated residuals are displayed as the black graphs above raw data and fits.

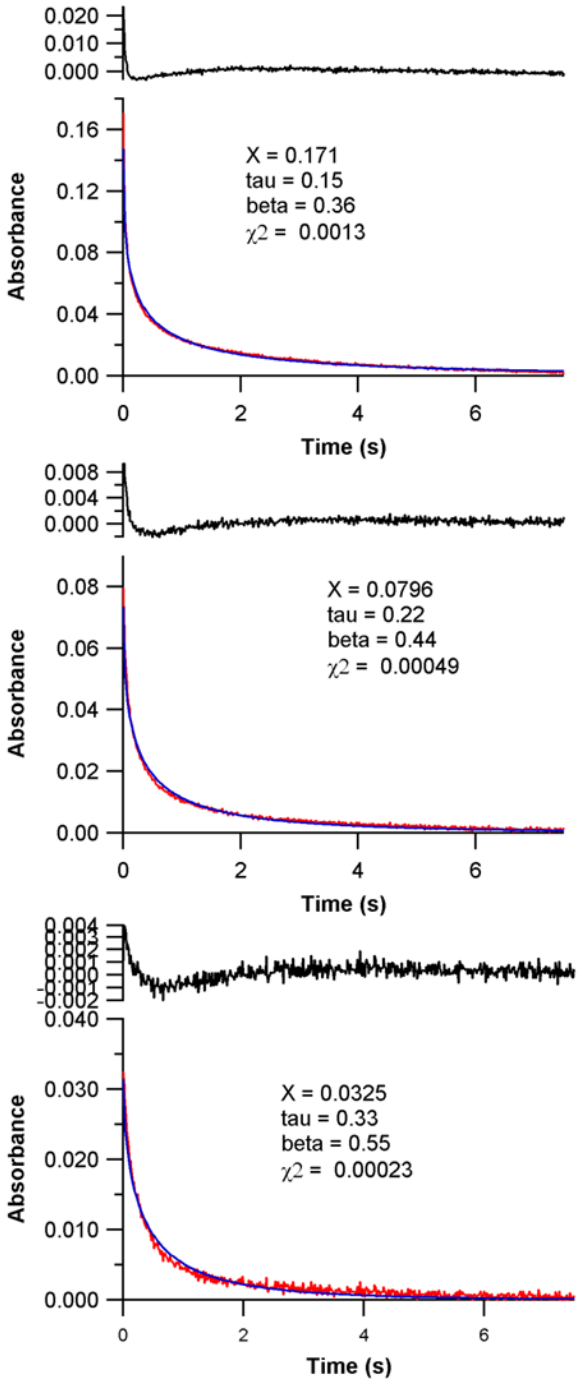

Figure A.11. Kinetic traces at 700 nm (red) for reaction of TEMPO, 4.8 mM with photo reduced ZnO NCs of different electron concentration 0.35 mM (top), 0.13 mM (middle), and 0.049 mM (bottom). The fits of data to a double exponential function (blue), Equation A-2. Associated residuals are displayed as the black graphs above raw data and fits.

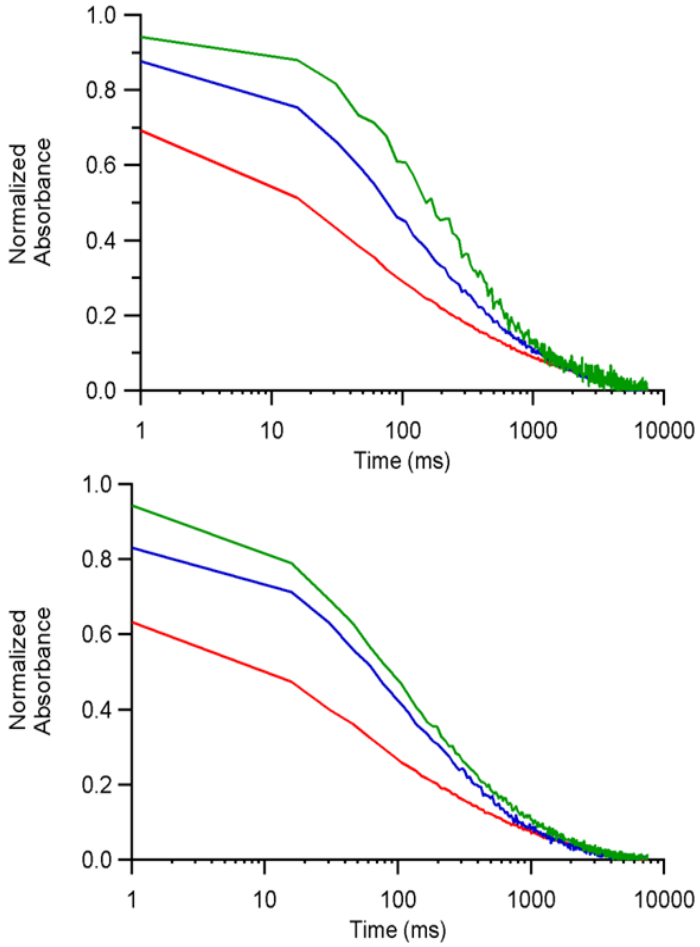

Figure A.12. Normalized kinetic traces from Figure 4.3b (top) and Figure 4.44b (bottom) plotted on a semi log scale to display the multi-exponential character of the data.

Estimation of the diffusion limited rate constants for reactions involving nanoparticles

The following apply the standard approach to estimate the diffusion limited rate constant for small molecules to nanoparticles. This uses the Stokes-Einstein equation and the assumption that a reaction occurs when two reactants are separated by a distance R^* that is the sum of the radii of the reacting materials. It should be emphasized that there are uncertainties in the application of the Stokes-Einstein equation, and that the equation for a diffusion limited rate constant is only approximate. Still, the measurements of diffusion constants by DOSY NMR given at the end of this section give the same result as that predicted from the Stokes-Einstein equation.

Case 1: Reactions of two nanoparticles

The rate constant of a diffusion-controlled reaction, "in which the two reactant molecules react if they come within a distance R* of one another is

$$k_d = 4\pi R^*(\Sigma D)N_A \qquad \text{A.3}$$

where ΣD is the sum of the diffusion coefficients of the two reactant species in solution"

P. Atkins "Physical Chemistry" 6th Ed. 1997, p. 827 ("Σ" added for clarity)

The magnitude of a diffusion constant can be estimated by the Stokes-Einstein equation "for diffusion of spherical [uncharged] particles through liquid with low Reynold's number." (From http://en.wikipedia.org/wiki/Einstein_relation_%28kinetic_theory%29)

$$D = \frac{k_B T}{6\pi \eta r}$$

where: D is the diffusion constant, η is viscosity, r is the radius of the spherical particle. A.4

We assume the validity of Stokes-Einstein and that the reaction radius R^* is roughly twice the particle radius r. Then rate constant for a diffusion controlled reaction of two nanoparticles of radius R that react when they touch at a distance $2r$ is given by:

$$k_d = 4\pi\, 2r\, N_A\, 2(k_B T/6\pi\, \eta\, r) \qquad \text{A.5}$$

$$k_d = (8/3)(N_A k_B T/\eta) \qquad \text{A.6}$$

This predicts that the diffusion-limited rate constant is independent of the radius of the particle. The slower diffusion of the larger nanoparticles is compensated by the fact that they react at a larger separation. This analysis predicts that the diffusion limited rate constant for reaction of two molecular species (*ca.* 10^{10} M^{-1} s^{-1}) will also apply to reactions of two nanoparticles. Based on our measurements of the diffusion constants by DOSY NMR, mentioned below, this may not quite hold, and the nanoparticle-nanoparticle diffusion limit may be a factor of two slower than a ferrocene-ferrocene diffusion limit.

Case 2: Reactions of a nanoparticle with a small molecule.

Consider a nanoparticle with diffusion constant D_P and radius r_P, and a small molecule with diffusion constant D_m and radius r_m. Then the reacting radius R^* is roughly $r_P + r_m$ and equation 3 becomes:

$$k_d = 4\pi(r_P + r_m)(D_P + D_m)N_A \qquad \text{A.7}$$

Using Stokes-Einstein for the diffusion constants gives:

$$k_d = 4\pi N_A(r_P + r_m)(k_BT/6\pi\eta)(1/r_P + 1/r_m) \quad \text{A.8}$$

$$k_d = (2/3)(N_A k_B T/\eta)(r_P/r_P + r_P/r_m + r_m/r_P + r_m/r_m) \quad \text{A.9}$$

$$k_d = (2/3)(N_A k_B T/\eta)(2 + r_P/r_m + r_m/r_P) \quad \text{A.10}$$

When r_P is, for instance, ten times larger r_m,

$$k_d = (2/3)(N_A k_B T/\eta)(2 + 10 + 0.1) = (24.2/3)(N_A k_B T/\eta) \quad \text{A.11}$$

This gives the counterintuitive result that the diffusion limit is *three times faster* for a nanoparticle + molecule reaction with a tenfold difference in size vs. the reaction of two nanoparticles or of two small molecules. This occurs because the diffusion is dominated by the small molecule while the larger nanoparticle radius means that the molecule does not have to diffuse as far.

The collision rate between a small molecule and a NC is estimated to be ~5×10^{10} M^{-1} s^{-1} for these ZnO NCs + TEMPO. For the reactions described here with ~5 mM TEMPO, the collision frequency will be >10^8 s^{-1}.

As noted above, this treatment is approximate so the derived factor of three should be viewed approximate. Still, the diffusion limit for unequal sized particles is thus shown to be larger than that for equal particles. This has been previously discussed in the context of proteins reacting with small molecules on page 135 of O. G. Berg, P. H. von Hippel *Annu. Rev. Biophys. Biophys. Chem.* **1985**, *14*, 131-160, DOI: 10.1146/annurev.bb.14.060185.001023 (and likely has been discussed elsewhere as well).

Preliminary unpublished results from Ms. Carolyn Valdez.
Using 2D ^{1}H diffusion-ordered (DOSY) NMR, the approximate diffusion coefficients of nanoparticles and small molecules (ferrocene) are directly measured, which allows us to make an estimate of the diffusion-limited rates for each reaction in toluene. By this calculation, the diffusion-limited rate constant is not quite independent of size, as the ferrocene-ferrocene k_D is a little more than double that of k_D for two 3 nm diameter nanoparticles.

*	**R* (r_A+r_B) (m)**	**Σ*D* (m^2s^{-1})**	**k_D ($M^{-1}s^{-1}$)**
Nanoparticle+Nanoparticle	6×10^{-9}	1.8×10^{-10}	8.17×10^{9}
Ferrocene+Ferrocene	6×10^{-10}	4×10^{-9}	1.82×10^{10}
Nanoparticle+Ferrocene	3.3×10^{-9}	2.1×10^{-9}	5.24×10^{10}

*The k_D was determined using $k_d = 4\pi R^*(\Sigma D)N_A$, where the estimated radii are based on a 6 nm diameter nanoparticle and the accepted hydrodynamic diameter of 0.6 nm for ferrocene (Canzi, G.; Morse, A. A.; Kubiak, C. P. *J. Phys. Chem. C* **2011**, *115*, 7972−7978). Diffusion coefficients for ferrocene and ZnO nanoparticles capped by dodecylamine were 2×10^{-9} m^2s^{-1} and 9×10^{-11} m^2s^{-1}, respectively, and were an average of three DOSY experiments in toluene-d_8.

VITA

Miles Braten was born in the San Francisco Bay Area and raised in Chico California near the foothills to the Sierra Nevada. He attended the University of San Francisco, blocks away from Golden Gate Park, where he earned a Bachelor of Science in Chemistry. Afterwards he spent a short stint in an analytical laboratory at Chevron's Richmond campus. He then worked in the Sandler-Moore Mass Spectrometry Facility at UCSF during which time he applied to graduate schools and chose to attend the University of Washington. Over the last five years he worked under the guidance of Dr. Jim Mayer on collaborative projects with Dr. Daniel Gamelin, defending his Doctoral Dissertation on October 6th 2015. He is currently looking for employment in the field of portable and stationary energy storage.